

# **Molecular dynamics of nanometric layers of glass formers in interaction with solid substrates**

---

Von der Fakultät für Physik und Geowissenschaften

der Universität Leipzig

genehmigte

DISSERTATION

zur Erlangung des akademischen Grades

DOCTOR RERUM NATURALIUM

(Dr. rer. nat.)

vorgelegt

von **M. Sc. Emmanuel Urandu Mapesa**

geboren am 9. Januar 1976 in Kakamega, Kenia

Gutachter:

Prof. Dr. Friedrich Kremer

Prof. Dr. Juan Colmenero de León

Tag der Verleihung:

17.11.2014

*The secret things belong to the LORD our God, but the things  
revealed belong to us and to our children forever ...*  
**Deuteronomy 29:29a**

## Bibliographische Beschreibung:

Mapesa, Emmanuel Urandu

### **Molecular Dynamics of nanometric layers of glass formers in interaction with solid substrates**

Universität Leipzig, Dissertation

<sup>1</sup>146 S., <sup>2</sup>272 Lit., <sup>3</sup>54 Abb., <sup>4</sup>4 Tab.,

## Referat:

Broadband Dielectric Spectroscopy (BDS) in combination with a nanostructured electrode arrangement – which circumvents the conventional need to evaporate metal electrodes onto soft matter – is used to study the molecular dynamics of several glass forming materials confined in nanometric ( $\geq 5$  nm) layers. Other complementary experimental tools employed in this work include spectroscopic vis-Ellipsometry (SE), AC-chip calorimetry (ACC), X-ray reflectometry (XRR), Differential Scanning Calorimetry (DSC) and Atomic Force Microscopy (AFM). The latter is used to characterize the topography of the samples and to determine their thicknesses. Under the conditions of annealing samples ( $T_g^{bulk} + 50$  K) in high oil-free vacuum ( $10^{-6}$  mbars) for at least 12 h and carrying out measurements in inert (dry nitrogen or argon) atmosphere, it is found for all studied thin layers that the structural relaxation, and hence the dynamic glass transition – in its mean relaxation times – remains within a margin  $\pm 3$  K from the respective bulk behaviour. It is revealed, *inter alia*, that the one-dimensional confinement of thin films introduces restrictions on other (slower) molecular relaxation processes which manifest, depending on the specific system under investigation, as (i) an interruption of the end-to-end (normal mode) fluctuation of the chains, or (ii) a slowing down of the  $\delta$ -relaxation when the system is cooled towards glass-formation. Furthermore, (iii) evidence is provided to show that the dimensionality of confinement plays a significant role in determining the resulting dynamics. A molecular understanding of these findings is given, and the discussion presented with respect to the on-going international debate about dynamics in confinement.

---

<sup>1</sup> ...S. (Seitenzahl insgesamt)

<sup>2</sup> ...Lit. (Anzahl der im Literaturverzeichnis ausgewiesenen Literaturangaben)

<sup>3</sup> ...Abb. (Abbildungen insgesamt)

<sup>4</sup> ...Tab. (Gesamtzahl der Tabellen)

## Abbreviations

AAO	Anodic aluminium oxide
ACC	Alternating current calorimetry
AFM	Atomic force microscopy
API	Active pharmaceutical ingredient
BDS	Broadband dielectric spectroscopy
BLS	Brillouin light scattering
DMA	Dynamic mechanical analysis
DR	Dye-reorientation
DSC	Differential scanning calorimetry
FS	Fluorescence spectroscopy
h	Hour(s)
HN	Havriliak-Negami
Hz	Hertz
LC	Liquid crystal
$M_c$	Critical molecular weight
$M_n$	Number-averaged molecular weight
mol	Mole(s)
$M_w$	Weight-averaged molecular weight
NBI	Nano-bubble inflation
NM	Normal mode
NS	Neutron scattering
PI	Poly(cis-1,4-isoprene)
PID	Polydispersity index
PLS	Positron lifetime spectroscopy
PS	Polystyrene
PTFE	Polytetrafluoroethylene
rms	Root-mean-square
$R_g$	Radius of gyration
s	Second(s)
SE	Spectroscopic vis-ellipsometry
SM	Segmental mode
TES	Thermal expansion spectroscopy
TSC	Terminal subchains
VFT	Vogel-Fulcher-Tammann
WLF	Williams-Landel-Ferry
XRD	X-ray diffraction
XRR	X-ray reflectometry

# Content

---

<b>1. Introduction</b>	<b>1</b>
<b>2. The glass transition and chain dynamics</b>	<b>3</b>
2.1 The phenomenology of the glass transition	3
2.2 Theories of the glass transition	8
2.2.1 Free volume theories	9
2.2.2 Cooperative concepts	10
2.2.3 Mode-coupling theory	12
2.3 Dynamics of polymer chains in melt	13
2.4 The dynamic glass transition in confinement	17
2.4.1 Experiments: state-of-the-art	17
2.4.2 Theoretical attempts at explaining dynamics in confinement	22
<b>3. Sample preparation and experimental techniques</b>	<b>25</b>
3.1 Thin-film preparation by spin-coating	25
3.1.1 Films on glass slides	25
3.1.2 Films on silicon wafers	26
3.1.3 Reproducibility of sample preparation	27
3.1.4 Stability of thin film samples	28
3.1.5 Film thickness determination	29
3.1.6 Sample annealing experiments	33
3.2 Use of nanostructured electrodes – a novel approach	34
3.3 Poly( <i>cis</i> -1,4-isoprene) (PI) in porous media	38
3.4 Experimental techniques	41
3.4.1 Broadband Dielectric Spectroscopy (BDS)	41
3.4.1.1 Polarization	42
3.4.1.2 Dielectric relaxation	47
3.4.1.3 Debye relaxation	49
3.4.1.4 Non-Debye relaxation	51
3.4.1.5 Dielectric data in the time domain	55
3.4.1.6 Conductivity contribution	56
3.4.1.7 The distribution of relaxation times	57
3.4.1.8 BDS – summary	58
3.4.2 Spectroscopic Ellipsometry (SE)	59
3.4.3 AC-chip calorimetry (ACC)	63
<b>4. Results and Discussion</b>	<b>67</b>
4.1 Effect of sample geometry on measured dynamics	67
4.1.1 Introduction	67

4.1.2 Experimental details	68
4.1.3 Results and discussion	69
4.1.4 Summary	74
4.2 Dynamics of polystyrene in a wide range of molecular weights	75
4.2.1 Introduction	75
4.2.2 Experimental details	75
4.2.3 Results and discussion	77
4.2.4 Summary	85
4.3 Molecular dynamics of itraconazole confined in thin supported layers	86
4.3.1 Introduction	86
4.3.2 Experimental details	88
4.3.3 Results and discussion	89
4.3.4 Summary	98
4.4 Segmental and chain dynamics in nanometric layers of poly( <i>cis</i> -1,4-isoprene)	
4.4.1 Introduction	99
4.4.2 Experimental details and data analysis	100
4.4.2.1 Sample preparation	100
4.4.2.2 Data analysis	101
4.4.3 Results and discussion	104
4.4.3.1 1- versus 2-D confinement of poly( <i>cis</i> -1,4-isoprene)	116
4.4.4 Summary	119
<b>5 Conclusions</b>	<b>121</b>
5.1 Dynamics in confinement – a wider perspective	122
<b>References</b>	<b>125</b>
<b>Appendices</b>	<b>142</b>
A1 List of Publications	142
A1.1 Peer-Reviewed Papers	142
A1.2 Book Chapters	143
A1.3 Conference proceedings and others	144
A2 Acknowledgements	145
A3 Selbständigkeitserklärung	146

# 1 Introduction

---

The last two decades have witnessed significant scientific effort towards understanding dynamics and the glass transition in thin films of low-molecular weight and polymeric systems. The first two major driving forces behind the research were: the supposition presented by theory that the glass transition has an inherent length scale, and hence that finite-size effects would arise if this length scale were reached; and, the fast developments in nanotechnology which demand materials in miniaturized sizes. As many research labs began to devote enormous resources in this endeavour, a third force emerged – highly disputable experimental results published in literature, and discussed in international fora. Key among these were reports of  $T_g$  reductions by as big a margin (from the bulk) as 70 K [1,2]– which would imply a decrease in the relaxation times of the segmental dynamics by a factor of about  $10^8$  – for thin polystyrene films. However, continued refining of experimental as well as computational tools now makes it possible to attain a better understanding of dynamics in confinement.

This thesis is designed to make a contribution to this discussion, and is focused on the following issues:

- 1) How does the sample geometry applied in investigating the dynamics in thin films by Broadband Dielectric Spectroscopy (BDS) affect the measured dielectric response?
- 2) Most attention has been paid to the effect of confinement on short time scale motions; how are longer time scale motions, e.g., normal mode relaxations, influenced by confinement?
- 3) If an identical sample preparation procedure were used, would BDS and ellipsometry deliver coinciding results?
- 4) From a molecular point of view, does the dimensionality (1- *vis-à-vis* 2-D) of confinement matter?
- 5) How does the concentration of the mother solution affect the dynamics of the resulting spin-cast films?





# 2 The Glass Transition and Chain Dynamics

---

## 2.1 Phenomenology of the glass transition

The word *glass* has various meanings. In everyday life, this term designates a fragile and transparent material well known since antiquity as well as certain objects made of it. In scientific language, its range of meaning is much larger but difficult to precisely define. All the same, the glassy state is ubiquitous in nature and technology. Window glass, composed mostly of sand, lime and soda, is the best known example of an engineered amorphous solid. Optical fibres are made of very pure amorphous silica, occasionally carefully doped. Most engineering plastics are amorphous solids, as are some metallic glasses and alloys of interest because of their soft magnetism and corrosion resistance [3]. The silicon used in many photovoltaic cells is amorphous, and there are indications that probably most of the water in the universe is glassy. A majority of these examples entail supercooling of a liquid to take advantage of viscous retardation of nucleation and crystallization.

Figure 2.1 shows the specific volume  $V_{sp}$  as a function of temperature for a typical liquid. Upon cooling from high temperatures, a liquid may crystallize at its melting point,  $T_m$ . This first-order phase transition usually results in a decrease of the specific volume (not true for water). When a liquid goes below  $T_m$  without crystallizing, it is said to be supercooled. The specific volume and other thermodynamic properties of a supercooled liquid are what would be expected from extrapolating to lower temperature the properties of the liquid above  $T_m$ . As a supercooled liquid is cooled to lower temperatures, its viscosity increases and the molecules which comprise it move more and more slowly. At some temperature, the molecules will be moving so slowly that they do not have a chance to rearrange significantly before the temperature is lowered further. Since this rearrangements are necessary for the liquid to find the equilibrium  $V_{sp}$  for that temperature, the experimentally observed  $V_{sp}$  will begin to deviate from the equilibrium value at this point. At temperatures not much lower than this, the time scales for the molecular rearrangements become relatively very

long compared to the time scale of the experimental observations. The structure of the material is *frozen* for practical purposes, and we call this a glass.  $V_{sp}$  continues to decrease as the temperature is lowered, but the thermal expansion coefficient ( $= [\partial \ln V_{sp} / \partial T]_p$ ) in the glassy state is significantly smaller than in the liquid and supercooled liquid states. Thermal expansion in the glassy and crystalline states is similar; in each case, expansion is dominated by atomic vibrations which are very similar in the two states.

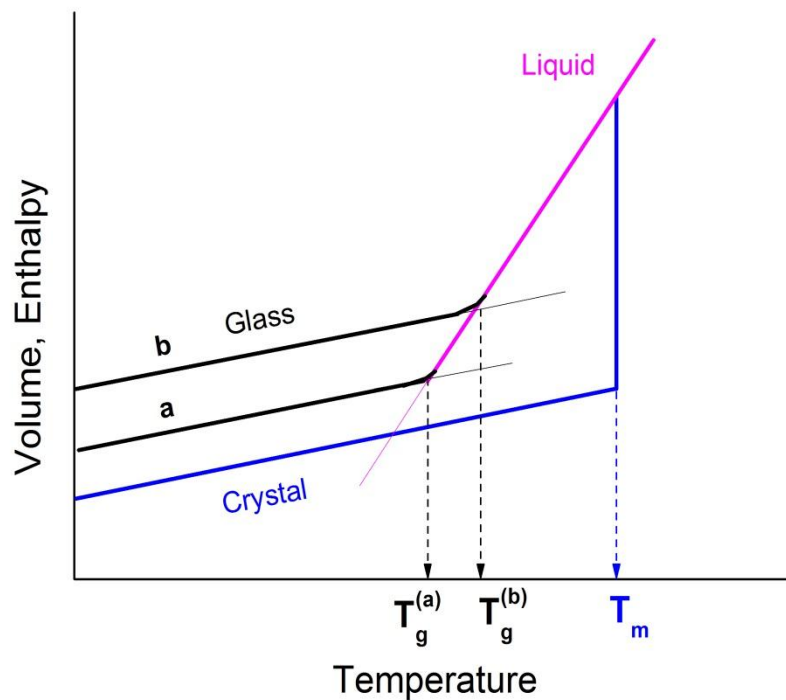


**Figure 2.1.** Temperature dependence of a liquid's specific volume  $V_{sp}$  or enthalpy  $H$  at constant pressure.  $T_m$  is the melting temperature. A slow cooling rate produces a glass transition at  $T_g^{(a)}$  while a faster cooling rate leads to a glass transition at  $T_g^{(b)}$ . The thermal expansion coefficient  $\alpha_p = (\partial \ln V_{sp} / \partial T)_p$  and the isobaric heat capacity  $C_p = (\partial H / \partial T)_p$  change abruptly but continuously at  $T_g$ . Adapted from [4] with permission.

The glass transition temperature  $T_g$  can be defined in many ways. One convenient method uses the change in the thermal expansion coefficient. As illustrated in Figure 2.1, this change is not sudden, but rather takes place over a range of temperatures (typically  $\sim 10$  K).

$T_g$  is different for different cooling rates: the slower a liquid is cooled, the longer the time available for configurational sampling at each temperature, and hence the colder it can become before falling out of liquid-state equilibrium. Therefore,  $T_g$  increases with cooling rate, although the dependence is typically weak; an order of magnitude change in cooling rate may change  $T_g$  by only 3-5 K [4]. Notwithstanding this fact,  $T_g$  is an important material property. When defined consistently, it is the single parameter which is most useful in estimating the mechanical properties of a polymeric material.

It is worth noting that the glass transition observed in the laboratory is, in actual fact, not any kind of phase transition. Rather, it is a kinetic event which depends upon the crossing of an experimental time scale and the time scales for molecular rearrangements. Its definition is dependent on conventions such as a constant cooling rate (e.g. 10 K/min) or a viscosity threshold of  $10^{12}$  Pa.s, among others [4]. Furthermore, glasses are neither crystals nor liquid crystals but simply liquids which are *frozen* on the time scale of the experimental observation. As indicated in Figure 2.1, there is not a single glassy state; the thermodynamic (and dynamic) properties of a glass depend upon its (thermal) history [5]. However, the question of whether some phase transition underlies the glass transition is a matter of continuing research [3–7].

In the high temperature limit, the dielectric relaxation time is about  $\tau_\infty \cong 10^{-13}$  s, attributed to local orientational fluctuations. The viscosity, on the other hand, has a value of about  $10^{-2}$  to  $10^{-1}$  poise. As the temperature is lowered, both the viscosity and the relaxation time increase strongly and can be approximated by the empirical Vogel-Fulcher-Tammann (VFT) [8–10] equation:

$$v(T) = \{2\pi\tau(T)\}^{-1} = v_\infty \exp \left[ \frac{-DT_0}{T-T_0} \right] \quad (2.1)$$

where  $v_\infty = (2\pi\tau_\infty)^{-1}$ ,  $D$  is a constant (commonly associated with the concept of fragility which is used to classify glass forming systems) and  $T_0$  is the so-called Vogel temperature (often also referred to as the ideal glass transition temperature) and is found – on average – to be  $\sim 40$  K below  $T_g$ . Equation 2.1 implies that as  $T \rightarrow T_0$ , the equilibrium relaxation time becomes infinite. This prediction cannot be verified simply because the system is bound to

fall out of equilibrium as  $T_0$  is approached. This divergence is also supported by the so-called Kauzmann paradox which occurs in the entropy determined from calorimetric measurements [11,12]. However, the physical meaning of this divergence remains unclear. It should be noted that although  $T_0$  should be regarded as a characteristic temperature for the dynamic glass transition due to the versatility of Eq. (2.1), this equation breaks down in high viscous regime. This is because it predicts relaxation times that are too large compared to what is experimentally obtained [13,14]. In spite of its limitations, Eq. (2.1) is still generally used for want of a better theory of the dynamic glass transition. The Williams-Landel-Ferry (WLF) equation often used to describe viscosity or relaxation times in polymers is mathematically equivalent to the VFT equation [12].

Figure 2.2 – showing the average relaxation rates for atactic polystyrene (PS) and *cis*-polyisoprene (PI) as a function of inverse temperature – provides examples of the VFT dependence. When  $T_g$  as obtained from calorimetric measurements (carried out at a cooling/heating rate of 10 K/min) is superimposed onto the relaxation map as shown in Figure 2.2, it is realized that the said  $T_g$  value occurs at a structural relaxation time of about 100 s. This coincidence provides an alternative approach to defining  $T_g$  as that temperature at which the relaxation rate is  $\sim 100$  s.

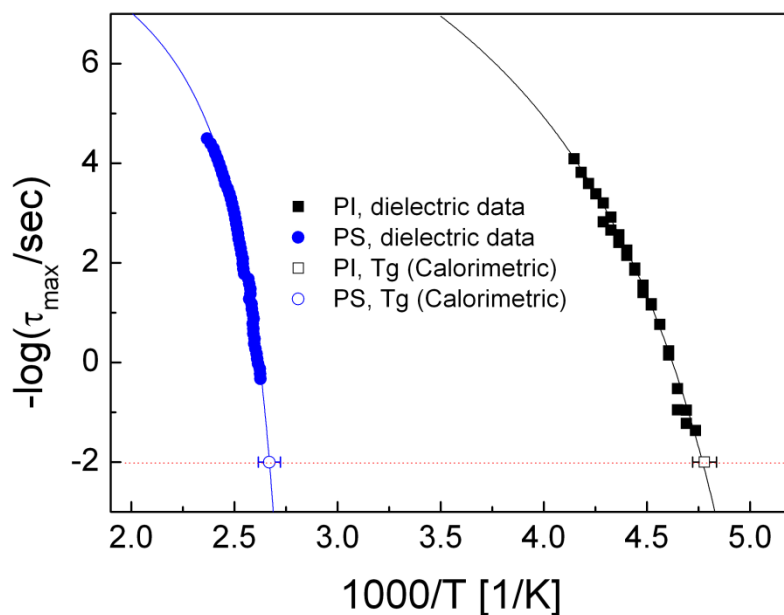


**Figure 2.2.** Structural relaxation times *versus* inverse temperature for cis-polyisoprene (PI) and atactic polystyrene (PS).  $T_g$  values for the same systems as obtained from calorimetric measurements are also shown. The lines are VFT fits to the dielectric data. Notice the agreement between the extrapolated VFT dependence and the calorimetric  $T_g$ .

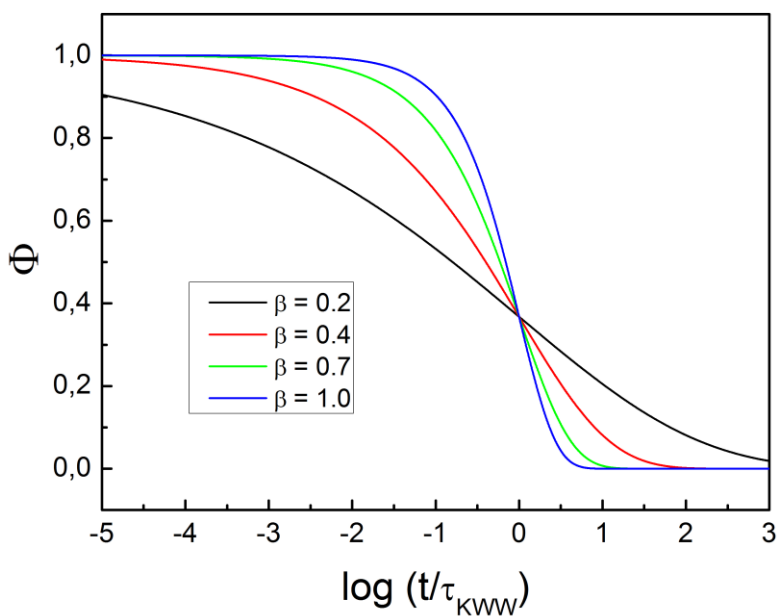


**Figure 2.3.** The response function,  $\Phi$ , for various Kohlrausch-Williams-Watts (KWW) parameters,  $\beta$ , as indicated.

An interesting feature of many supercooled liquids is the non-exponential time response of the liquid to external stimuli; the response function,  $\Phi(t)$ , obeys the so-called “stretched exponential” or Kahlrausch-Williams-Watts (KWW)[15] law:

$$\Phi(t) = \exp\left[-\left(\frac{t}{\tau}\right)^\beta\right], 0 < \beta \leq 1 \quad (2.2)$$

where  $\tau$  is the related relaxation time and  $\beta$  the KWW constant. As can be seen (Fig. 2.3), the smaller the value of  $\beta$ , the less exponential the response function. If  $\beta = 1$ , a single exponential function is recovered. For instance, if the temperature of a typical fragile supercooled liquid is suddenly lowered by half a Kelvin, the volume does not approach the new equilibrium volume exponentially. Similarly, if some net orientation is given to molecules, say by an electric field, the molecules won’t randomize their orientations exponentially. Two possible explanations have been suggested to rationalize the KWW law [16]: one may think of the existence of a heterogeneous set of environments in a supercooled liquid; in this case the relaxation in one such set is almost exponential, but the relaxation times vary significantly between the different environments. Alternatively, a supercooled liquid can be thought of as being homogeneous, and that each molecule therein relaxes nearly identically in an intrinsically non-exponential manner.

## 2.2 Theories of the glass transition

In spite of the many attempts made to understand the nature of the glass transition, the theories so far proposed do not capture all the salient features of this phenomenon. However, they provide insight into the problem, and have paved way for further experimental, computational and theoretical efforts. Broadly speaking, these theories can be classified into three categories: (i) theories that assign a phase transition to a low temperature, below  $T_g$ , where the viscosity and relaxation times appear to diverge; (ii) those that pay attention to

temperatures above  $T_g$  – they try to explain the initial features of the slowing down of the liquid-like processes; and (iii) theories that do not consider any temperature as being of unique importance. In the following Section, a select set of commonly invoked theories is discussed.

### 2.2.1 Free Volume Theories

In these theories [17], the total volume of a liquid is supposed to consist of two parts: one,  $V_{occ}$ , that is occupied by molecules, and another – so-called free volume,  $V_f$ , – where the molecules are free to move, hence accounting for diffusive motion. A redistribution of the free volume leads to the random motion of the molecules, but no free energy is required for this process. When temperature is decreased, both  $V_{occ}$  and  $V_f$  reduce, and liquid-glass transition is postulated to be a result of the decrease of  $V_f$  (of the amorphous phase) below some critical threshold [18–20]. Below  $T_g$ , the free volume becomes *frozen in* with no further redistribution taking place. The VFT-dependence is recovered starting from the Doolittle equation [21] which provides an empirical relation between the viscosity  $\eta$  and the free volume:

$$\eta = Ae^{B/\frac{V_f}{V_{occ}}} \quad (2.3)$$

where A and B are empirical constants. If the thermal expansion of a liquid is assumed to be linear, then its free volume can be expressed as:

$$V_f = (T - T_g)V_g\Delta\alpha + V_{fg} \quad (2.4)$$

where  $V_g$  is the total volume of the glass at  $T_g$ ;  $\Delta\alpha = \alpha_l - \alpha_g$  is the difference between the thermal expansion coefficient of a liquid and that of a glass;  $V_{fg} = V - V_{occ}$ , with  $V$  being the total volume.

Substituting for Eq. (2.3) into Eq. (2.4) for  $V_f$ , the VFT law for the temperature dependence of the viscosity is recovered. The free volume model was extended by Cohen and Grest [22], by applying a percolation theory to account for the exchange of free volume between nearest “liquid-like” cells. They reasoned that a free exchange of volume can occur only between liquid-like cells which are nearest neighbours and which have a sufficiently large number of other liquid-like nearest-neighbour cells that the volumes of any neighbouring solid-like cells are not constrained to change simultaneously. In this way the “communal” entropy associated with the accessibility of all the configuration volume inside the liquid clusters is determined.

It is instructive to note that although the free volume approach is simple and accounts for some aspects of the liquid-glass transition, it has inherent shortcomings: (i) it is developed from a hard sphere model [23], where no directional bonds are present, but is applied to strongly covalent glass forming materials possessing directed bonds; and (ii) it fails to explain the decoupling between the temperature dependence of the rotational and translational diffusion for supercooled liquids [24–29].

### 2.2.2 Cooperative Concepts

The idea of cooperative relaxation for glass formers was first proposed by Adams and Gibbs [30] in a theory which relates relaxation aspects to entropy considerations. In this model, the configurational changes of a liquid originate from a collective motion of an ensemble of its molecules. The smallest domains, which are capable of altering their configuration independent of their molecular neighbourhood, are called cooperatively rearranging regions (CRR). Considering the size of the CRR, this approach then suggests a characteristic length for the dynamic glass transition, which increases with decreasing temperature. The probability of cooperative rearrangements is related to the total configurational entropy,  $S_c$ , by:

$$P(T) \approx e^{-\left\{\frac{c}{TS_c(T)}\right\}} \quad (2.5)$$



where  $C$  is a constant and  $S_c$  is determined from the step in the calorimetric heat capacity at  $T_g$ :

$$S_C(T) = \int_{T_0}^T \frac{\Delta C_p}{T} dT \quad (2.6)$$

Assuming a hyperbolic form for the configurational heat capacity (the configurational heat capacity is that part of the heat capacity that is due to configurational rather than vibrational degrees of freedom)  $\Delta C_p = D/T$  [31], the following expression for the configurational entropy results:

$$S_C = D \left( \frac{T-T_0}{TT_0} \right) \quad (2.7)$$

It is easy to see that when  $T \rightarrow T_0$ , then  $S_C \rightarrow 0$ , akin to the Kauzmann paradox. Additionally, from Eqs. (2.5) and (2.6), the VFT dependence for the viscosity is recovered. Donth [32] proposed a development of the cooperative concept by presenting a model which derives the temperature dependence of the characteristic size of cooperatively rearranging regions  $\xi_{CRR}$  as:

$$\xi_{CRR}(T) \approx (T - T_0)^{-2/3} \quad (2.8)$$

where  $T_0$  represents the Vogel temperature. Based on calorimetric data, this characteristic size was estimated to be in the range of 0.7 – 2.2 nm (corresponding to ~ 100 cooperatively rearranging molecules) in the vicinity of the glass transition temperature. There have been more experimental attempts at estimating the characteristic length of the glass transition [33–36]. Although the CRRs were originally thought of as being spherical volumes with diameter  $\xi$ , some computer simulations suggest that the cooperative motion is essentially string-like [37], with the string length increasing with falling temperature. A major shortcoming of the cooperative concepts is the assumption of no interaction between neighbouring regions. Since the string-like shape is less compact compared with the spherical one, region-region interactions will be more significant and must have a unique signature for the effect of confinement on the dynamic properties of the glass-formers [38].

### 2.2.3 Mode-Coupling Theory (MCT)

Mode-coupling theory attempts to explain the complex behaviour of the supercooled liquids by invoking the concept of a non-linear feedback mechanism. From the coupling of slowly decaying correlation functions, the theory predicts the existence of a characteristic temperature  $T_c$  above the experimental glass transition temperature  $T_g$  for the liquid [39–41]. The time-dependent decay of the density-density correlation function can be expressed in the form of a non-linear, damped second order differential equation of the form:

$$\left\{ \frac{d^2}{dt^2} + \gamma \frac{d}{dt} + \omega_0^2 \right\} \Phi(t) + 4\lambda\omega_0^2 \int_0^t M(t-t')\Phi(t')dt' = 0 \quad (2.9)$$

where  $\gamma$  represents a damping parameter,  $\omega_0$  the harmonic frequency of longitudinal sound-waves while  $\lambda$  is a term characterizing the strength of the non-linear coupling. This coupling is described by a memory function  $M(t)$ , acting as another damping function for longitudinal sound waves. As a first approximation, the wave vector dependence of the memory function is neglected, and  $M(t)$  is related to the response function,  $\Phi(t)$ , simply by:

$$M(t) = \Phi^2(t) \quad (2.10)$$

Eq. (2.9), in combination with Eq. (2.10), predicts a stretched-exponential decay of  $\Phi(t)$  when the parameter  $\lambda$  approaches – from the liquid side – a critical value of  $\lambda_c = 1$ . When  $\lambda = \lambda_c$ , the density-density fluctuations are frozen-in, hence, the existence of a dynamic glass transition is predicted and is evidently entirely controlled by kinetic factors. For  $\lambda$  approaching the critical value of 1 from glass, a power-law singularity for the relaxation time is predicted:

$$\tau = \left| 1 - \frac{\lambda}{\lambda_c} \right|^{-1.765} \quad (2.11)$$

Owing to experimental findings, some extensions of the MCT have been made: key among them is the removal [42] of the ideal-glass transition singularity present in the model of Leutheuser [40]. Furthermore, the wave-vector dependence of  $M(t)$ , neglected by Leutheuser, has been treated by Bengtzelius [39], with the result that only the density fluctuations whose wave-vectors are comparable to those corresponding to the first peak in the static structure factor contribute to the feedback mechanism underlying the glass transition.

The MCT has its failures amongst which is its prediction of a sharp glass transition at a temperature  $T_C$ , but  $T_C > T_g$ . This implies a kinetic arrest to a non-ergodic phase at temperatures where the system is still ergodic and liquid. Additionally, this theory predicts a power-law divergence of transport coefficients (e.g. diffusion and viscosity) and relaxation times, but this is less accurate over a wide range of temperatures [43].

## 2.3 Dynamics of polymer chains in melt

The dynamics of linear polymer chains in the melt is influenced mainly by the chain length: for short, unentangled chains, the dynamics is determined by a balance between viscous and entropic forces; for long chains, topological constraints become dominant [44]. If a polymer molecule were stretched out by applying forces on its endgroups, upon release of these forces the molecule would return to its initial coiled conformation. This is because the transition back to an isotropic coil increases the number of available rotational isomeric states and hence the entropy. In mechanistic terms, if the endgroups – or simply two arbitrary points within the molecule – were held at a fixed distance from each other, a tensile force would arise owing to the net moment transfer onto the ends (or points). If a sequence within a chain that has a mean squared end-to-end distance  $\langle \Delta \vec{r}^2 \rangle$  is selected and its end points are a distance  $\Delta \vec{r}$ , then the tensile force is (assuming Gaussian properties) [45]:

$$\vec{f} = b \Delta \vec{r} \quad (2.12)$$

with

$$b = \frac{3kT}{\langle \Delta \vec{r}^2 \rangle} \quad (2.13)$$

This result is interesting since it implies that: a sequence behaves like a spring, showing a linear dependence of the force on the extension;  $b \propto T$ , as is characteristic for forces of entropic origin; and,  $b$  decreases with a growing size of the sequence.

A polymer chain in melt is in an environment of other chains, and therefore this surrounding influences its motion. For simplicity, the interactions with adjacent molecules can be represented by one viscous force, as is usually done for the dynamics of a colloid in solvent. If a colloid moves through a solvent with a velocity  $\vec{v}$ , the solvent molecules in contact with its surface create a force that is proportional to  $\vec{v}$ , and the solvent viscosity  $\eta_s$ ,

$$\vec{f} = \zeta \vec{v} \quad (2.14)$$

where  $\zeta$  is the friction coefficient (which is directly proportional to the solvent viscosity). Rouse developed a treatment of the dynamics of polymer chains in melt by using this idea of a viscous force, and taking into consideration the tensile forces in stretched parts of the chain. In the Rouse model, the chain is first subdivided into  $N_R$  Rouse sequences, with each sequence being sufficiently long to ensure Gaussian properties. Secondly, each Rouse sequence is substituted by a bead and a spring; the former plays the role of a centre whereupon friction forces are exerted, while the latter represents the elastic tensile forces. Then a Rouse chain is one comprising of beads interlinked by springs as schematically presented in Figure 2.4. The equations of motion of the Rouse chain are formulated neglecting all inertial effects, so that the velocity  $d\vec{r}_l/dt$  of bead  $l$  is given by

$$\zeta_R \frac{d\vec{r}_l}{dt} = b_R(\vec{r}_{l+1} - \vec{r}_l) + b_R(\vec{r}_{l-1} - \vec{r}_l) \quad (2.15)$$

where  $\zeta_R$  is the friction coefficient per bead and  $b_R$  is the force constant of the springs which depends on the mean squared end-to-end distances of the Rouse sequences,  $a_R^2$ . From Eq. (2.13), it is clear that

$$b_R = 3kT/a_R^2 \quad (2.16)$$

This set of differential equations can be solved easily by first noting that motions in the 3-D space decouple and are equivalent. Considering now the  $z$ -direction, and assuming a chain with an infinite length, then we have translational symmetry in terms of  $l$ . Therefore there must be wave-like solutions of the form

$$z_l \propto e^{(-t/\tau)} e^{(i/\delta)} \quad (2.17)$$

where an exponential time dependence is anticipated as is the case for all relaxation processes,  $\tau$  is the relaxation rate and  $\delta$  is the phase shift between adjacent beads. Substituting Eq. (2.17) into Eq. (2.15), delivers the relationship between the relaxation rate and  $\delta$  as:

$$\frac{1}{\tau} = \frac{4b_R}{\zeta_R} \sin^2\left(\frac{\delta}{2}\right) \quad (2.18)$$

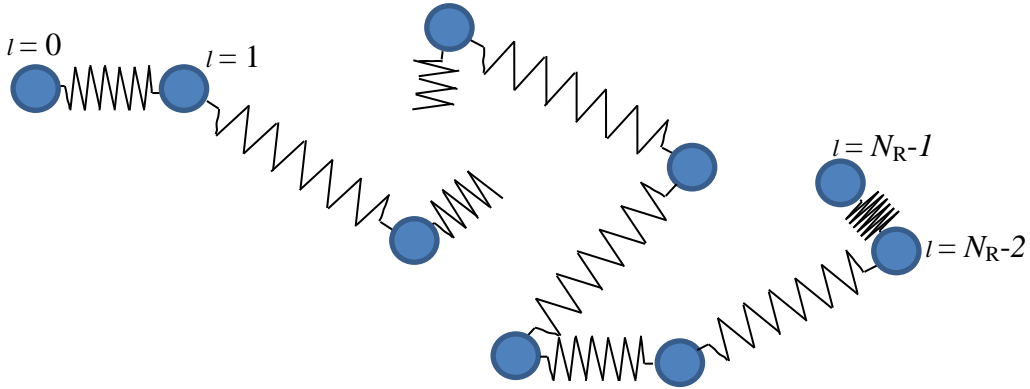


**Figure 2.4.** A Rouse chain consisting of  $N_R$  beads interlinked by springs

Since a linear chain has free tail ends where the tensile forces vanish, the boundary conditions read as,

$$z_1 - z_0 = z_{N_R-1} - z_{N_R-2} = 0 \quad (2.19)$$

or in differential form:

$$\frac{dz}{dl}(l=0) = \frac{dz}{dl}(l=N_R-1) = 0 \quad (2.20)$$

The real and imaginary parts of Eq. (2.17)

$$z_l \propto \cos(l\delta) e^{-\frac{t}{\tau}}, \text{ and } z_l \propto \sin(l\delta) e^{-\frac{t}{\tau}} \quad (2.21)$$

represent separate solutions of the equation of motion. Only the cosine solution fulfils the boundary condition at  $l=0$ . The condition for the upper end,  $l=N_R-1$ , then selects the values of  $\delta$  by

$$\frac{dz_l}{dl}(l=N_R-1) \propto \sin\{(N_R-1)\delta\} = 0 \quad (2.22)$$

Since this is solved by

$$(N_R-1)\delta = m\pi, \quad (2.23)$$

the following eigenvalues are obtained for a linear chain with free ends,  $\delta_m$ :

$$\delta_m = \frac{\pi}{N_R-1} m, \quad m = 0, 1, 2, \dots, N_R-1 \quad (2.24)$$

Therefore for the linear chain, there are  $N_R$  independent solutions, which are called Rouse modes and are differentiated by their order  $m$ . From Eq. (2.18) and Eq. (2.24) we obtain the so-called Rouse time,  $\tau_R$  as:

$$\tau_R = \frac{1}{3\pi^2} \frac{(\zeta_R/a_R^2)}{kT} R_0^4 \quad (2.25)$$

where  $R_0^2 = a_R^2(N_R-1)$ . Eq. (2.25) indicates that the ratio  $\zeta_R/a_R^2$  is independent of the choice of the sequence, which is true if the friction coefficient  $\zeta_R$  is proportional to the number of monomer units in the sequence. In fact this is a basic requirement of the Rouse

model. Eq. (2.25) also gives the dependence of the Rouse time on the molecular weight,  $M$ ; since  $R_0^2 = a^2N$ , and  $N \propto M$ , we get for the longest relaxation time,  $\tau_1$ :

$$\tau_1 \propto M^2 \quad (2.26)$$

For entangled polymers, the tube model developed by de Gennes [46] predicts a maximum relaxation time (for the so-called reptation process),  $\tau_d$ , which is different from  $\tau_1$  in the Rouse theory. The ratio between  $\tau_d$  and  $\tau_1$  is written as

$$\frac{\tau_1}{\tau_d} = \frac{a}{3L} \quad (2.27)$$

where  $L$  is the contour length of the primitive chain. This model predicts the  $M^{3.0}$  dependence of  $\tau_d$ . Experiments on high molecular melts are in qualitative agreement with the predictions of the reptation theory but yield a slightly higher exponent of 3.4, e.g., for the zero shear viscosity, which is proportional to  $\tau_d$  [47].

## 2.4 The dynamic glass transition in confinement

### 2.4.1 Experiments: State-of-the-art

Today, the nature of the glass transition remains a subject of intense studies in soft matter science even after several decades of devoted investigations. This arises from the fact that while several theoretical models (see Section 2.2) have been put forward to explain this phenomenon, none vigorously explains all aspects of the rubber-to-glass transition. In an attempt to make a break-through, considerable research effort is now focussed on understanding glass-formers in confinement. The cooperative concepts of Adam and Gibbs [30] inform this approach since it is reasoned that for a sufficiently supercooled liquid, structural relaxation can only occur when a number of constituent molecules re-arrange collectively. This cooperativity therefore suggests so-called finite size effects, that is, changes in the dynamics and glass transition temperature when the material is confined to length scales near the cooperative size. Such confinement can be achieved and studied using, *inter alia*,

nanoporous media, entangled polymeric systems, or thin films. The latter provide an ideal sample geometry since the extent of confinement can be remarkably increased simply by reducing the thickness of the films.

Another reason which informs the focus on glass-formers in confinement is their current and potential technological applications. In many of these applications (e.g. photoresists, batteries, sensors for smart drug delivery, nanolubrication, nanoadhesion, etc ), the materials are used in miniaturized dimensions for purposes of increasing performance and for convenience. Consequently, they have – due to an increased surface area to volume ratio – a large fraction of segments near an interface. How aspects of this miniaturization – confinement effects, interfacial interactions and finite size effects – influence overall properties of the system must be understood for appropriate innovation. To this end, several experimental techniques (e.g. Ellipsometry [2,48–74], X-ray Reflectivity [70,75–80], Differential Scanning Calorimetry [52,53,81–88], Positron Lifetime Spectroscopy [73,89,90], AC-Chip Calorimetry [70,91–94], Fluorescence Spectroscopy [67,95–107], Neutron Scattering [66,80,108–110], Brillouin Light Scattering [1,50,111–113], Rheology [114–116], Atomic Force Spectroscopy [117,118], Nanobubble Inflation [119–123], dewetting [124–126], Optical Waveguide Spectroscopy [127], Broadband Dielectric Spectroscopy [69–71,82,88,89,91,128–147]) have been employed to study key parameters (such as molecular weight [2,49,64,70,89,129], tacticity [51,56,148,149], measurement ambience [65,131,133,138,150,151], nature of polymer-substrate interaction [49,51,52,59,71,75,111,127,151,152], concentration of mother solutions [146] and even the type of experimental technique [59,74,144,153]) that may influence the observed dynamics in confinement. In this section, two important parameters, i.e. polymer-substrate interaction and preparative aspects, are reviewed.

Interactions at the polymer-substrate interface may be attractive, repulsive or neutral. Several studies have reported an increase in  $T_g$  when the film-substrate interactions are polar in nature and hence dominated by attractive forces, e.g., isotactic poly(methylmethacrylate) (PMMA) [49,51,59] or poly-(2)-vinylpyridine (P2VP) [152] on SiO<sub>2</sub> wafers. In such cases, interaction is feasibly presumed to be via hydrogen bonding between surface hydroxyl



(OH) groups and electronegative groups, e.g. the oxygen atoms in methacrylate. PMMA, for instance, has two oxygen atoms in each methacrylate side group, and both oxygen atoms contain a pair of unshared electrons, a criterion for hydrogen bonding [154]. This bonding is hypothesized to restrict (segmental) mobility, and hence result in higher-than-bulk  $T_g$  values. However, in a recent study [147] where isolated P2VP chains were deposited onto SiO<sub>2</sub> substrates, it was shown that only about ~10% of the polymer segments make bonds with the terminal OH groups on the surface, and that this leads to a broadening – but no shift – of the  $\alpha$ -relaxation peak.

For thin films with free surfaces or in contact with repulsive surfaces, some studies have reported  $T_g$  reductions with reducing film thickness [48,49,75,127,155–157]. Prucker *et al.* [127], for example, deposited PMMA thin films on HMDS {hexamethyldisilazane}-treated, hence hydrophobic glass substrates, and found a  $T_g$  depression of up to ~15 K for a spincoated 10-nm-thin sample. This, and similar results by other authors, has been rationalized by thinking of polymers at air interfaces or in contact with repulsive surfaces as being dominated by entropic effects such as chain-end segregation [75], confinement effects, or disentanglement [111], which lead to a speed-up of the relaxation. While these ideas seem plausible, this picture becomes complicated when we consider the fact that divergent results have been reported for the case where exactly the same polymer-substrate combination was investigated. For instance Keddie *et al.* [48] and Wallace *et al.* [76] studied polystyrene on hydrogen-terminated silicon surfaces and observed a decrease and an increase in  $T_g$ , respectively, with reducing film thickness. Furthermore, in a substantive study of this parameter, Erber *et al.* [71] systematically varied the interfacial interactions for atactic PMMA from attractive (native silicon oxide -SiOx) to weak and strongly repulsive interactions (as realized by gold-coated and HMDS-treated SiOx surfaces, respectively). Their results (see Fig. 2.5) revealed no dependence of the calorimetrically-determined  $T_g$  and the BDS-accessed dynamics, within the limits of experimental uncertainty, on the nature of polymer-substrate interactions.

There's no doubt that in the thin-film geometry, the overall system significantly comprises of surfaces and hence polymer-substrate interactions and free interfaces must play a nota-

ble role on the resultant dynamics. Nonetheless, what exactly that role is remains a subject of scientific debate. Changes in  $T_g$  as often reported in literature should mean increased or retarded molecular mobility in thin films. Based on diffusion experiments, however, it is unclear how and to what extent mobility is altered in supported films [158–161].

Aspects of sample preparation and treatment before and during actual measurements must also play a key role in determining the dynamics in thin polymer layers. As already evident from the scheme in Figure 2.1, the glass transition temperature – and of course, the molecular dynamics – of any given bulk material depends on the material’s thermal history. This, and other related aspects like the remaining solvent content and measurement ambient, becomes more significant as the surface-to-volume ratio of the material increases.

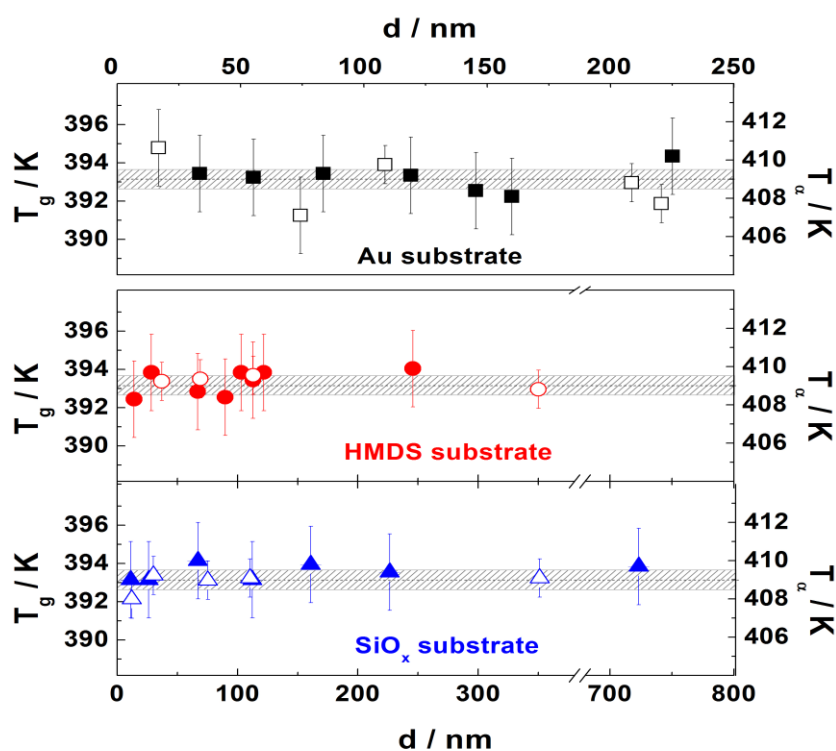


**Figure 2.5.** The glass transition temperature,  $T_g$ , of atactic-PMMA thin films measured by ellipsometry (filled symbols) and the characteristic temperature,  $T_a$ , of its segmental relaxation at 120.74 Hz measured by BDS (open symbols) plotted *versus* layer thickness  $d$ . The measurements were carried out on different substrates having hydrophobic (gold-coated and HMDS-treated) and hydrophilic ( $\text{SiO}_x$ ) surfaces. The calorimetrically determined  $T_g$  of the bulk is shown by dashed lines, and the experimental error of  $\pm 0.5$  K (shaded region) is included for comparison. Adapted from [71] with permission.

In a majority of studies, thin layers are prepared by spin-coating from solution. Typically, a polymer solution is first placed on a substrate, before the substrate is spun rapidly. Because of the centrifugal force, a film of the solution is formed, and the excess is ejected off the edge of the substrate. The film continues to thin slowly till disjoining pressure effects cause the film to reach an equilibrium thickness or until it turns solid-like due to a dramatic rise in viscosity resulting from solvent evaporation [162]. Even though most of the solvent evaporates in the course of spin-coating, it has been shown that a significant fraction remains in the polymer film [163] and preferentially accumulates at the polymer-substrate interface [162,164]. Such remaining solvent acts as a plasticizer and artefactually speeds up the dynamics [88,162,165]. Additionally, the process of spin-coating results in polymer chains being quenched in a non-equilibrated state due to the torque-induced changes in their conformation. Serghei and Kremer [138] have demonstrated that such non-equilibrium states may have not-bulk-like dynamics, and that their metastable character can be ostensibly reproducible.

Therefore, in order to remove solvent and to allow the films to relax to equilibrium, an appropriate annealing procedure must be applied. Typically, an annealing temperature tens of Kelvins above  $T_g$  is sufficient when applied for at least 12 h [69,70,146,147]. To avoid chemical degradation likely to occur in the presence of water or oxygen at elevated temperatures, the use of an inert atmosphere – such as high vacuum (better than  $10^{-6}$  mbars) or argon or dry nitrogen ambience – is inevitable. Serghei *et al.* [131,133] investigated polystyrene films in different ambients and observed that the dynamics became faster-than-bulk for samples measured in air, but remained bulk-like for samples probed in dry nitrogen atmosphere or vacuum (Fig. 2.6). Infrared measurements revealed that the former result was due to a reduction in molecular weight occasioned by oxygen-induced chain scissions.

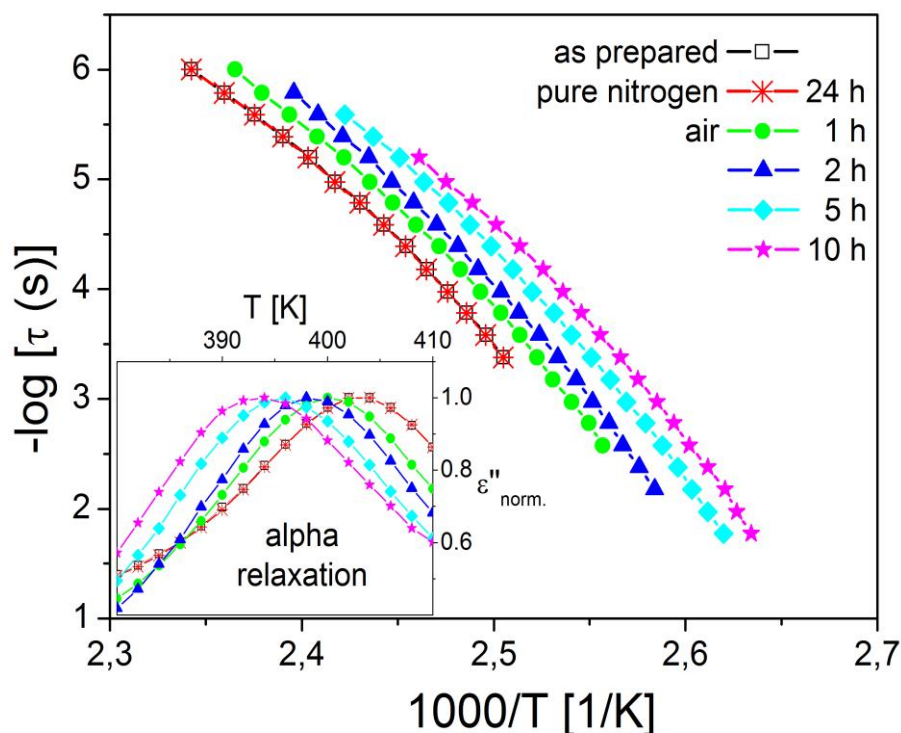


**Figure 2.6.** The Relaxation rate *versus* inverse temperature (alpha process) for a 63 nm thin polystyrene film as prepared, after 24 hours annealing at 180 °C in a pure nitrogen atmosphere, and after 1, 2, 5 and 10 hours annealing at the same temperature in air. Adopted from [131] with permission.

#### 2.4.2 Theoretical attempts at explaining dynamics in confinement

P.G. de Gennes [166,167] developed what he called a sliding-model in an attempt to explain the drastic reductions of the glass transition temperature as observed in thin free-standing polymer films. In this approach, the chain loops which are in contact with the free interface are presumed to exhibit a special type of relaxation, the so-called *sliding* motion. These sliding modes, promoted by the enhanced mobility due to the presence of the free interface, are held responsible for the reported faster dynamics. In the framework of this model, the experimentally observed thickness- and molecular-weight-dependent  $T_g$  shifts are qualitatively reproduced. Nonetheless, the interaction between the polymer and the substrate is not considered.

Another attempt to explain  $T_g$  shifts has been put forward by Long, Lequeux and Sotta [168,169] who propose a thermodynamic model for the glass transition. Their picture, whose basic ideas spring from the free volume model, is based on the concept of dynamic heterogeneity. Considering the thermally induced density fluctuations in the bulk, the authors suppose that the glass transition is controlled by the percolation of small domains of slower dynamics. In this context, the differences between the 3D glass transition (as in the bulk) and the quasi-2D glass transition (characteristic for thin films) are discussed. It is shown that the  $T_g$  shifts reported in the literature can be well-reproduced. In addition, a pronounced dependence of the confinement-effects on the interactions of the polymer at the interfaces is revealed. Thus, for freely-standing films, it is demonstrated that the domains of slower dynamics percolate at lower temperatures than in the bulk, and hence the  $T_g$  reduction. In the case of strongly adsorbed films, an enhanced percolation occurs, resulting in a broadening of the glass transition and in an increase of the glass transition temperature. In both cases – strongly and weakly adsorbed films – the  $T_g$  shifts depend on film thickness as a power law with an exponent related to the inverse correlation length of the 3D percolation.

Herminghaus [170–172] has also proposed a theoretical understanding of the confinement effects observed in thin polymer films. The focus here is on small molecular weights for which changes in the chain conformation due to geometrical finite size effects are excluded. Two main assumptions are made: the glass transition temperature in thin polymer films is determined by the spectrum of their viscoelastic eigenmodes which are affected by the vicinity of the free surface; and, the glass transition is physically caused by memory effects in the polymer material. This theory succeeds to rationalize a number of experimental findings reported in the literature. Fundamentally, it attempts to explain (i) why  $T_g$  shifts show no significant molecular weight dependence; (ii) the pronounced confinement effects in freestanding films as compared to their supported counterparts; (iii) the dependence of the  $T_g$  shifts on the substrate's chemical composition; and (iv) the fact that in some cases an increase of  $T_g$  is to be expected.



# 3 Sample Preparation and Experimental Techniques

---

In this chapter, the procedure of preparing and characterizing thin film samples is presented. Furthermore, the basic theory underlying the employed experimental techniques is briefly reviewed.

## 3.1 Thin film preparation by spin-coating

### 3.1.1 Films on glass slides

Glass slides measuring 1 cm x 1 cm x 1 mm are mounted on a Teflon rack and cleaned in an ultra-sound alkaline bath (of deionized water and Hellmanex<sup>TM</sup> (Sigma Aldrich) – an alkaline concentrate commonly used in the glass industry) at a temperature of 334 K for 15 minutes. They are then rinsed in pure acetone and dried under nitrogen flow before being mounted on a mask, and put in an evaporation chamber where aluminium electrodes (~0.8 mm wide, ~80 nm thick) are deposited in oil-free high vacuum ( $10^{-6}$  mbar). Subsequently, thin polymer films are spin-coated onto the slides from solution at a moderate rate of 50 rev/sec, to avoid possible chain breaking. The thickness of the polymer layers is varied by changing the concentration of the polymer in solution. Prior to the evaporation of a second Al counter-electrode, the films are annealed (typically at  $T_{g\text{-bulk}} + 50$  K, where  $T_{g\text{-bulk}}$  is the calorimetric glass transition temperature of the bulk material) in oil-free vacuum ( $10^{-6}$  mbar) for at least 24 hours to remove remaining solvent, and equilibrate them. Before dielectric measurements, the films were annealed again for several hours to remove any water that may be adsorbed in the course of transfer. The final sample geometry resulting from this preparation is displayed in Figure 3.1. It is simply referred to as the capped geometry and is the conventional approach widely employed (e.g. in [69,70,129,173–175]) for confinement studies.

### 3.1.2 Films on silicon wafers

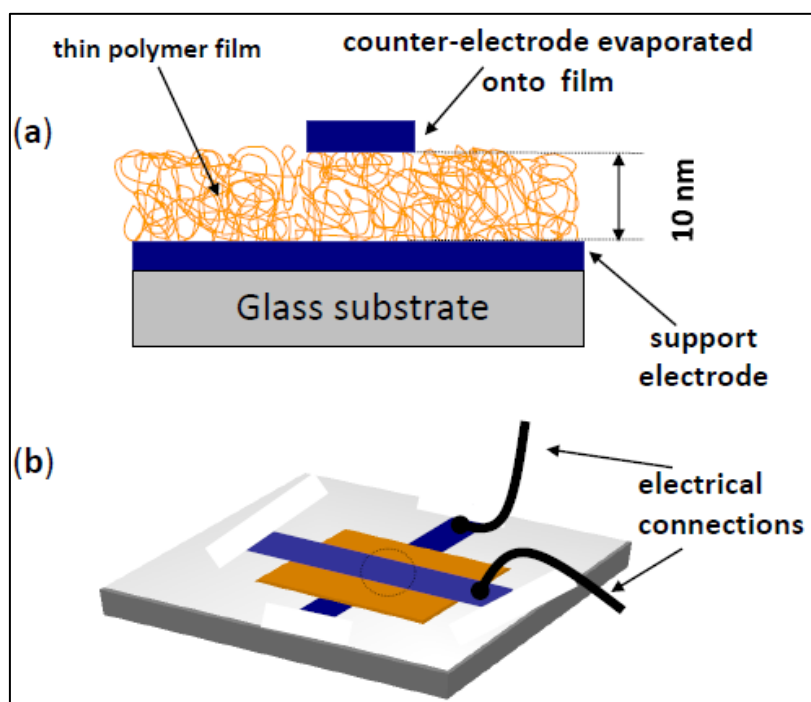


**Figure 3.1.** (a) A schematic representation of a cross-sectional view of the conventional capped geometry for thin film studies; the thin polymer film is sandwiched between two metal electrodes. (b) A display of how electrical contacts are made on the resulting capacitor for purposes of dielectric measurements.

Highly doped silicon wafers with orientation (100) were purchased from MicroFab Bremen. These wafers have a root mean square (rms) roughness of 0.23 nm (as determined on a scan area of  $1 \mu\text{m}^2$  by Atomic Force Microscopy), specific resistivity less than  $3 \text{ m}\Omega\text{cm}$ , and a 30-nm thermally oxidized surface layer. First, a layer of Al ( $\sim 80 \text{ nm}$ ) is evaporated on the backside of the wafers in high vacuum ( $10^{-6} \text{ mbar}$ ) and a coating of photoresist then spincoated on the frontside. These two layers serve as electrical contacts, and protection during subsequent cutting (into smaller pieces), respectively. Thereafter, the wafer dice (typically  $4 \text{ mm} \times 8 \text{ mm}$ ) are rinsed in acetone to remove the photoresist; purged with a plasma cleaner and a snow-jet gun to eject any organic contaminants; sonicated successively in acetone (10 minutes) and dichloromethane (10 minutes); and, dried under nitrogen flow and



on a hot plate (at 423 K for 5 minutes) before eventual spin-coating of polymer films in the same manner as described in section 3.1.1 above. Details on how a capacitor for dielectric measurements is assembled having polymer films on silicon dice are provided in Section 3.2.

### 3.1.3 Reproducibility of sample preparation

The reproducibility of samples both for the capped and uncapped geometries has been carefully checked. Figure 3.2 shows representative data for two identical polyisoprene thin film samples of thickness  $\sim 20$  nm prepared using the same recipe and measured in the uncapped geometry; it is clearly seen that the dielectric data thus obtained is reproducible, within the limits of experimental uncertainty.

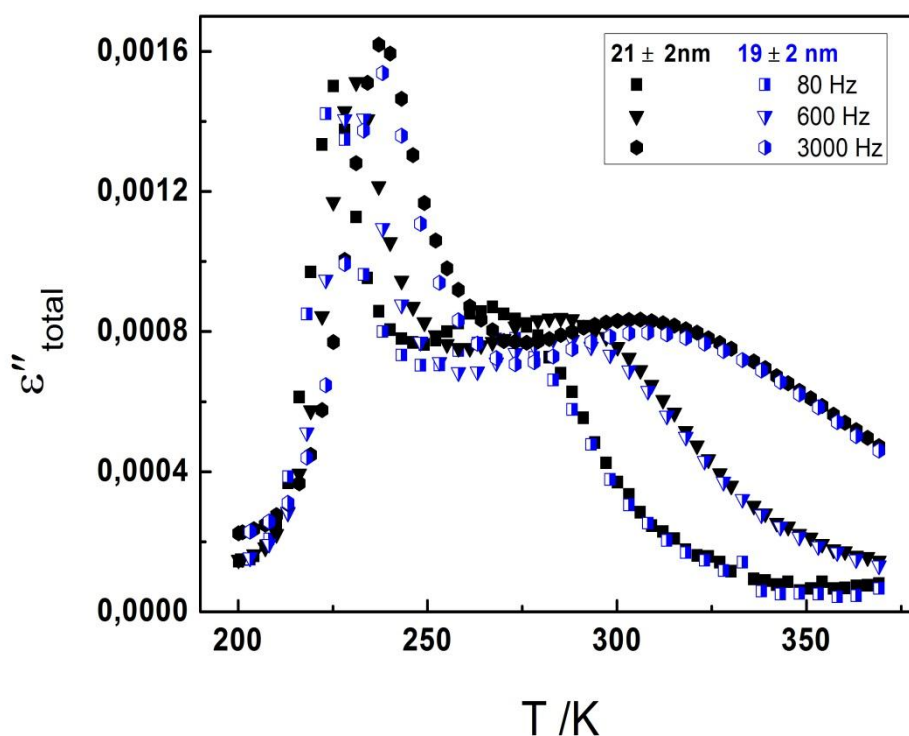


**Figure 3.2.** Dielectric loss  $\epsilon''_{total}$  as a function of temperature, at different frequencies, for two polyisoprene ( $M_w = 11\,600$  g/mol) samples prepared from the same solution, and hence having nearly the same thickness (as indicated) and measured in the uncapped geometry (s. Section 3.2)

### 3.1.4 Stability of thin film samples

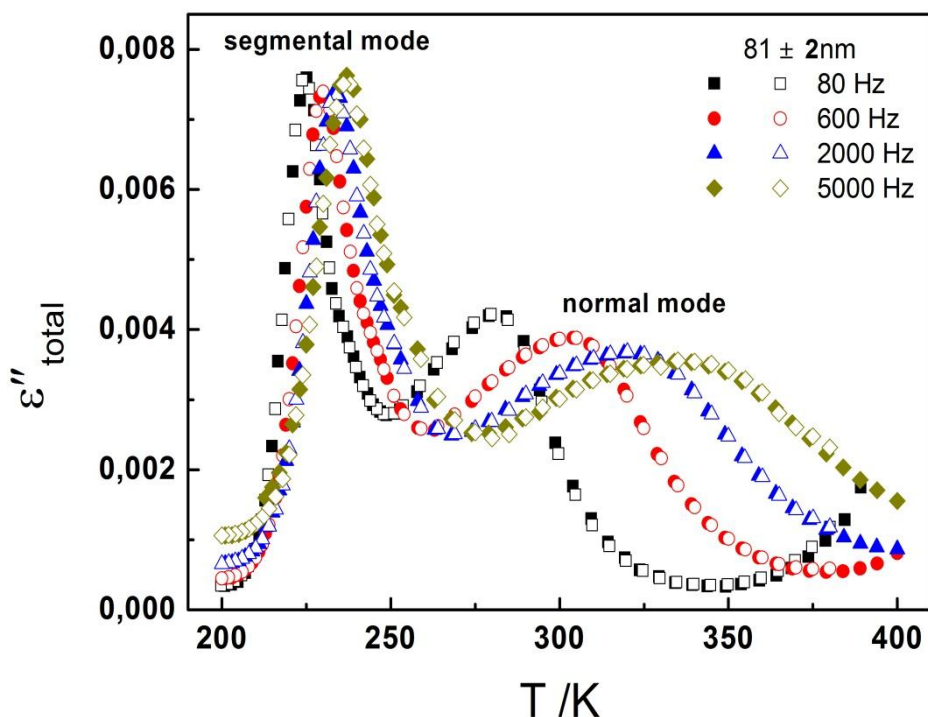


**Figure 3.3.** Dielectric loss  $\epsilon''_{total}$  as a function of temperature, at different frequencies, for a polyisoprene ( $M_w = 11\,600 \text{ g/mol}$ ) sample of thickness  $81 \text{ nm}$  measured (in the uncapped geometry) after 24 hrs of annealing at  $400 \text{ K}$  (filled symbols), and after a subsequent annealing for 48 hrs (empty symbols).

The thermal stability of the thin polymer films was also checked. It was revealed that so long as the films are kept in inert atmosphere (oil-free high vacuum -  $10^{-6} \text{ mbar}$ , or dry nitrogen flow), their dielectric response is reproducible even after being kept at elevated temperatures far above their glass transition for several days. Figure 3.3 provides the results of such an experiment: a thin PI film with a thickness of  $81 \text{ nm}$  was annealed for 24 hrs at  $400 \text{ K}$  in high vacuum before the first dielectric measurements. Thereafter, this sample was kept at  $400 \text{ K}$  in dry nitrogen flow for 48 hrs and re-measured. No changes are observed both for the segmental and chain dynamics as accessed by Broadband Dielectric Spectroscopy. The surface topography of this sample was also inspected by Atomic Force Microscopy; its root-mean-square (rms) roughness remains unchanged – within the limits

of experimental uncertainty – when comparison is made between the as-prepared film, and the film after all heat-treatment and dielectric measurements (see Figure 3.4).

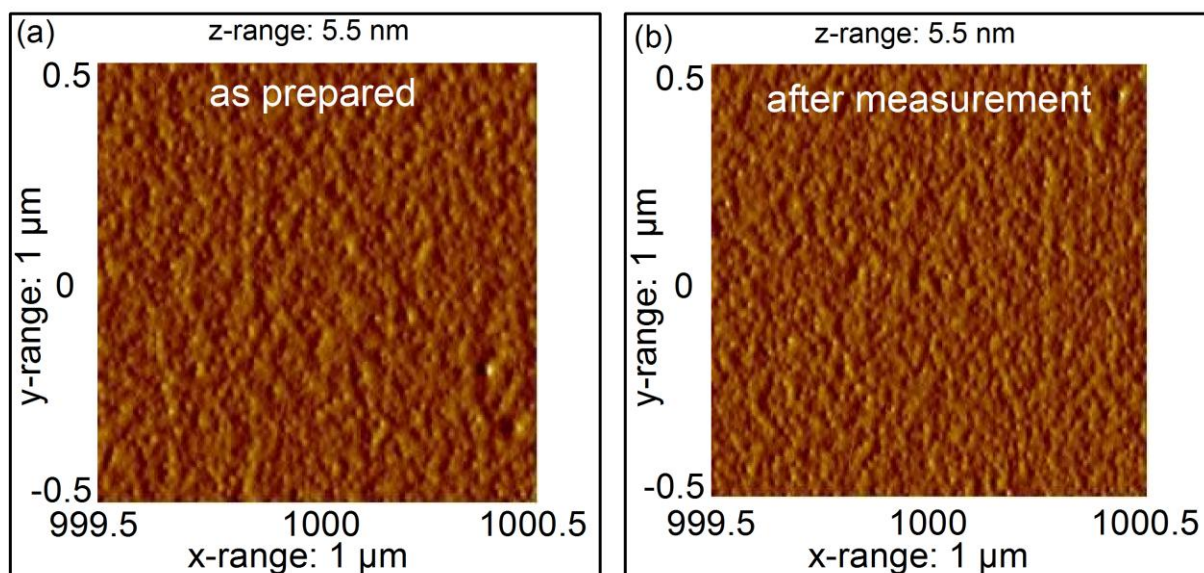


**Figure 3.4.** AFM images of the surface of a thin polyisoprene layer (thickness, 81 nm) as prepared (a) and after annealing and dielectric measurements (b). The rms roughness values are  $1.7 \pm 0.1$  and  $1.6 \pm 0.1$  nm, respectively.

### 3.1.5 Film thickness determination

The thickness of a polymer film is conventionally the most important parameter in confinement studies since it defines the extent of expected restriction on molecular dynamics. Its determination is therefore a critical aspect of experiments of the kind reported in this work. There are several means of finding the thickness of thin films; these include interferometry, ellipsometry, x-ray reflectivity, spectrophotometry, stylus profilometry, microgravimetry, capacitive measurements and atomic force microscopy [176,177]. The last two were used in the current report, and are discussed herebelow.

The capacitive technique was used for determining the thickness of capped samples. The procedure demands measurement of the sample capacitance,  $C(\omega)$ , in a spectral region where dielectric dispersions are minimal, i.e, at high frequencies and low temperatures ( $10^5$  Hz and 300 K in this work). Both the area of the sample and  $\epsilon'_{\infty}$  (the real part of the dielectric permittivity of the polymer in the high frequency limit) must be known. The former is obtained by measuring the length and width of the electrodes with the aid of an optical microscope, while the latter is determined from dielectric measurements of the bulk material in a sample holder of known dimensions. The  $\epsilon'_{\infty}$  thus obtained was compared with values readily available in literature, and agreements within uncertainties better than 1 % ascertained. Notably, it is assumed here that  $\epsilon'_{\infty}$  is thickness-invariant, a fact that has been experimentally proven, at least for linear polymers [178,179], but may not be valid for their architecturally-modified counterparts such as star-branched and grafted polymers. The thickness,  $d$ , of the film is then calculated assuming a parallel-plate capacitor from the well-known equation,  $d = (\epsilon_0 \epsilon'_{\infty} A) / C(\omega)$  where  $\epsilon_0 (= 8.854 \times 10^{-12} \text{ AsV}^{-1} \text{ m}^{-1})$  and  $A$  are the permittivity of free space and area of the active capacitor, respectively. The value of  $d$  obtained in this manner assumes ideally ultra-flat interfaces. Atomic Force Spectroscopy (AFM) was therefore used as a counter-check; deviations of up to 3% were observed between these two approaches.

The absolute film thickness and the surface topography were determined by employing a Veeco Dimension 3000 Metrology Atomic Force Microscopy (AFM) (Digital Instruments, Veeco Metrology Group) operated in tapping mode by using silicon tips (nominal radius of curvature  $< 10$  nm) with a force constant of about 40 N/m and a resonance frequency in the range 200-400 kHz. The AFM approach requires that some part of the polymer film be stripped off the substrate (say, using a sharp steel blade) and the resulting groove or step scanned in tapping mode. An appropriate image (with 512×512 pixels) is obtained by scanning in such a way as to capture both the groove and the intact film surface. In this way, the surface topography of both the substrate and the polymer film is analyzed (using the Gwyddion software 2.25 [180]) and the thickness estimated (with a 1-2 nm precision) by making a linecut through the AFM image as shown in Figure 3.5a.

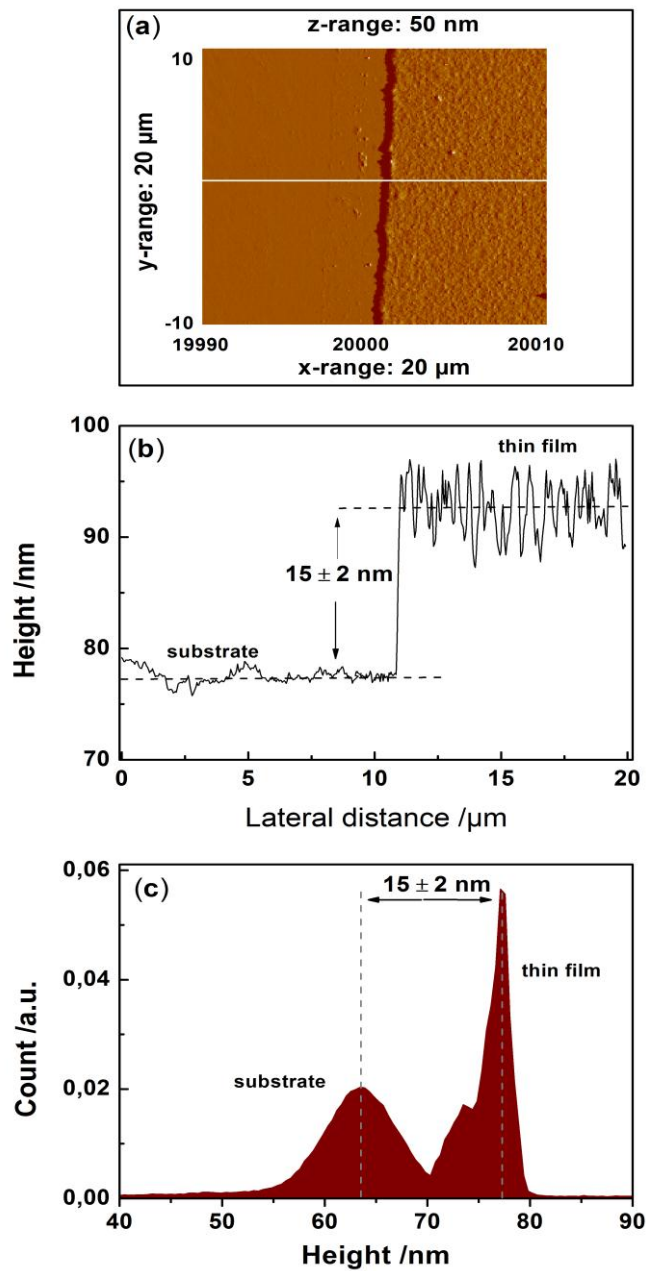


**Figure 3.5.** (a) AFM image ( $20 \mu\text{m} \times 20 \mu\text{m}$ ) of a 15-nm-thin polystyrene (PS-60) film scanned in such a way as to include both the scratched area and the unharmed film surface; (b) a vertical surface profile corresponding to the linecut shown in (a); (c) the corresponding histogram displaying the height distribution in the AFM image.

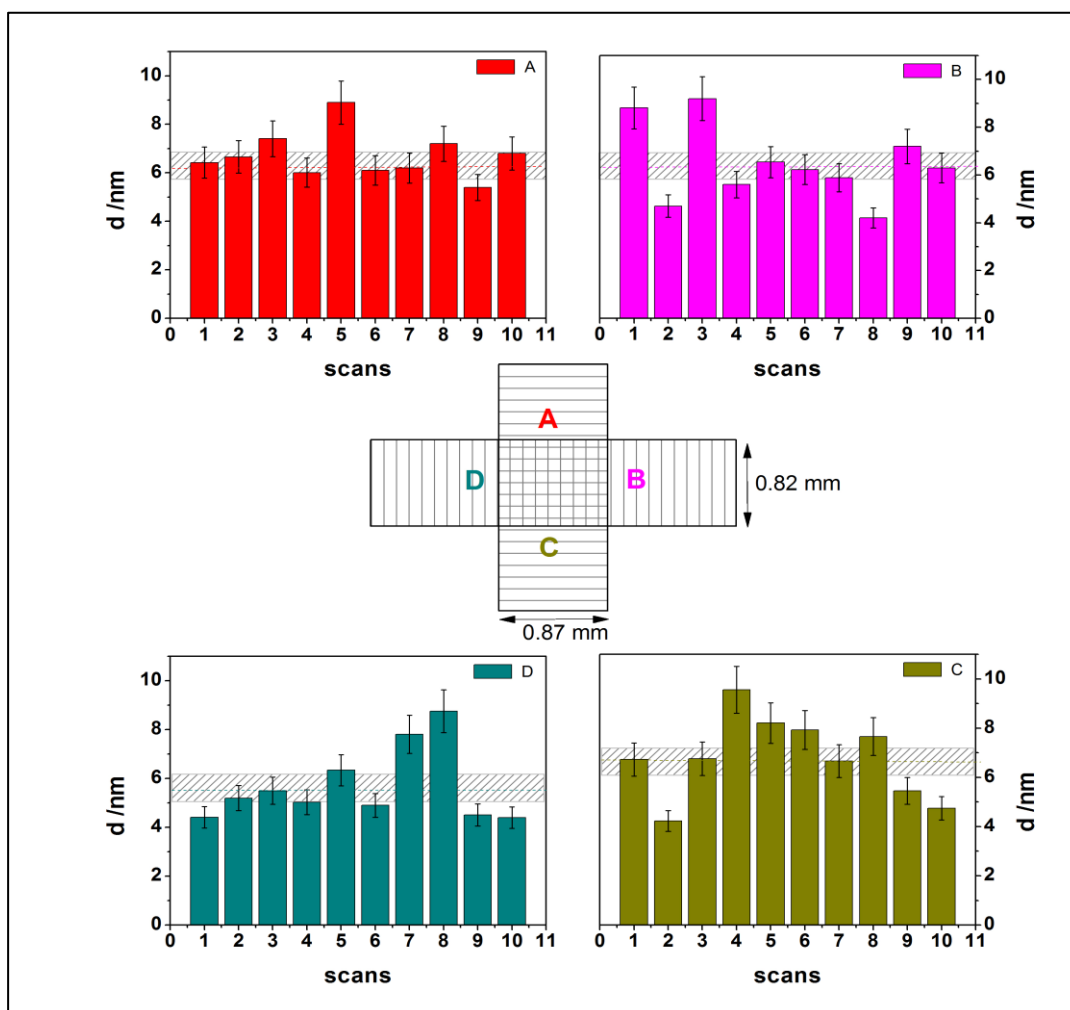


**Figure 3.6.** Thicknesses as determined from the analyses of various scratches made in regions A, B, C and D of a capped thin film sample. The mean thickness thus determined is  $6 \pm 2$  nm. Inset – a scheme of the sample showing the different regions in which scratches were made, and scanned.

From the line-cut, a vertical surface profile is plotted (Fig. 3.5b), and the film thickness is simply the height difference between the substrate and the film. To take care of the height distributions on the image – which is the more accurate approach – the histogram of the vertical heights is obtained, from which two peaks emerge. These correspond to the height distributions on the substrate and the film surface (Fig. 3.5c.) The distance between the maximum positions of the peaks is the film thickness, averaged over the whole area of the

AFM scan. In comparison with the capacitive method, which provides the average thickness over the whole sample area, AFM allows only a local determination. Therefore, for good statistics, AFM measurements have to be performed at many points on the sample. For uncapped samples, the scratches were made in the actual active capacitor area since the counter-electrode can be easily removed. Figure 3.6 illustrates how this was done for capped samples. Ten (10) scans each were carried out in regions A, B, C and D (inset, Fig. 3.6), which lie in the immediate neighbourhood of the capacitor of interest (whose typical dimensions are indicated).

### **3.1.6 Sample annealing experiments**

An important step in the sample preparation is the annealing procedure applied. This annealing – carried out in oil-free high vacuum ( $10^{-6}$  mbars) at temperatures above  $T_g$  (of the bulk material) for several hours – is required in order to remove solvent and equilibrate the thin layer before dielectric measurements. In order to estimate the duration of time needed for sufficient annealing, the dielectric response of a test sample is monitored during annealing. Figure 3.7 provides a representative illustration for a 111-nm thick polyisoprene sample. There's a sharp decrease in the dielectric loss (as monitored at fixed frequencies) immediately after reaching the annealing temperature (400 K), followed by a gradual fall observed over several hours. From this experiment, it is determined that annealing must last for at least 12 h before substantive dielectric measurements.

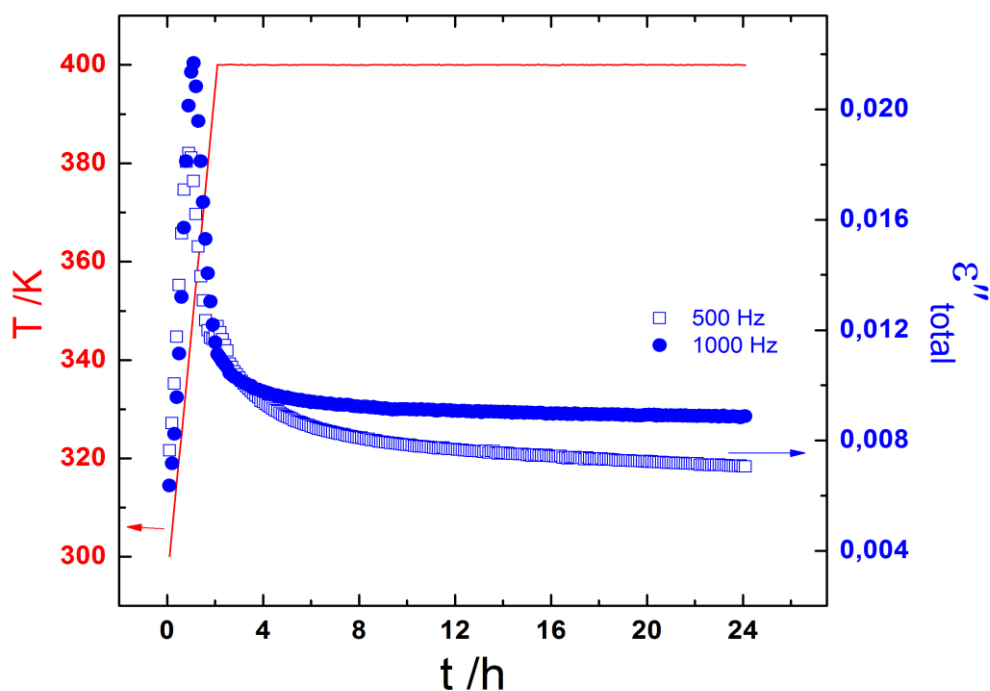


**Figure 3.7.** The imaginary part of the measured permittivity,  $\epsilon''_{total}$ , as monitored at two chosen frequencies for a thin polyisoprene sample prepared with nanostructured electrodes, and the temporal evolution of the temperature  $T$  (red line) in the annealing chamber.

### 3.2 Use of nanostructured electrodes – a novel approach

A current hot topic in soft matter research is focussed on determining how the molecular dynamics underlying the glass transition phenomenon change due to interfacial interactions. The experimental tool employed to unravel this must grant access to the glassy dynamics occurring on a molecular scale and, as well, quantitatively determine the corresponding relaxation time distribution function. Broadband dielectric spectroscopy fulfils these requirements but, in its conventional application, is limited due to the fact that it is a volume-specific technique. For instance, the common approach (Section 3.1.1) to studying thin polymer layers by dielectric spectroscopy – where the sample must be assembled in a capacitor arrangement - involves evaporating a metal electrode onto the polymeric material. This however demands that only fairly thick layers ( $\geq 10$  nm) can be probed since elec-



trical shortcuts arise when the thickness is further diminished. Additionally, the evaporation of a metal onto soft matter introduces artefactual effects – as will be shown later in this work.

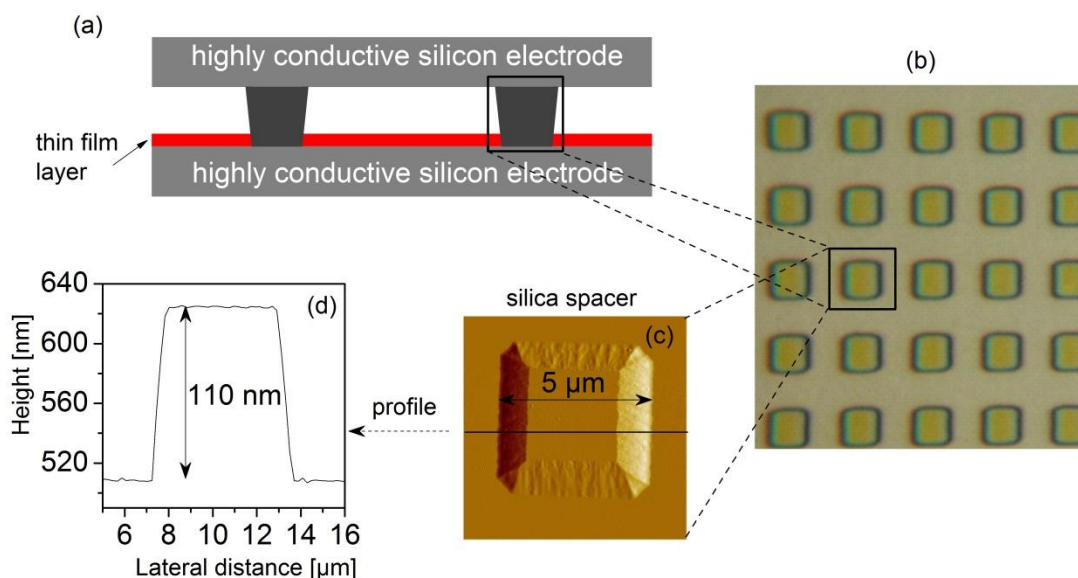


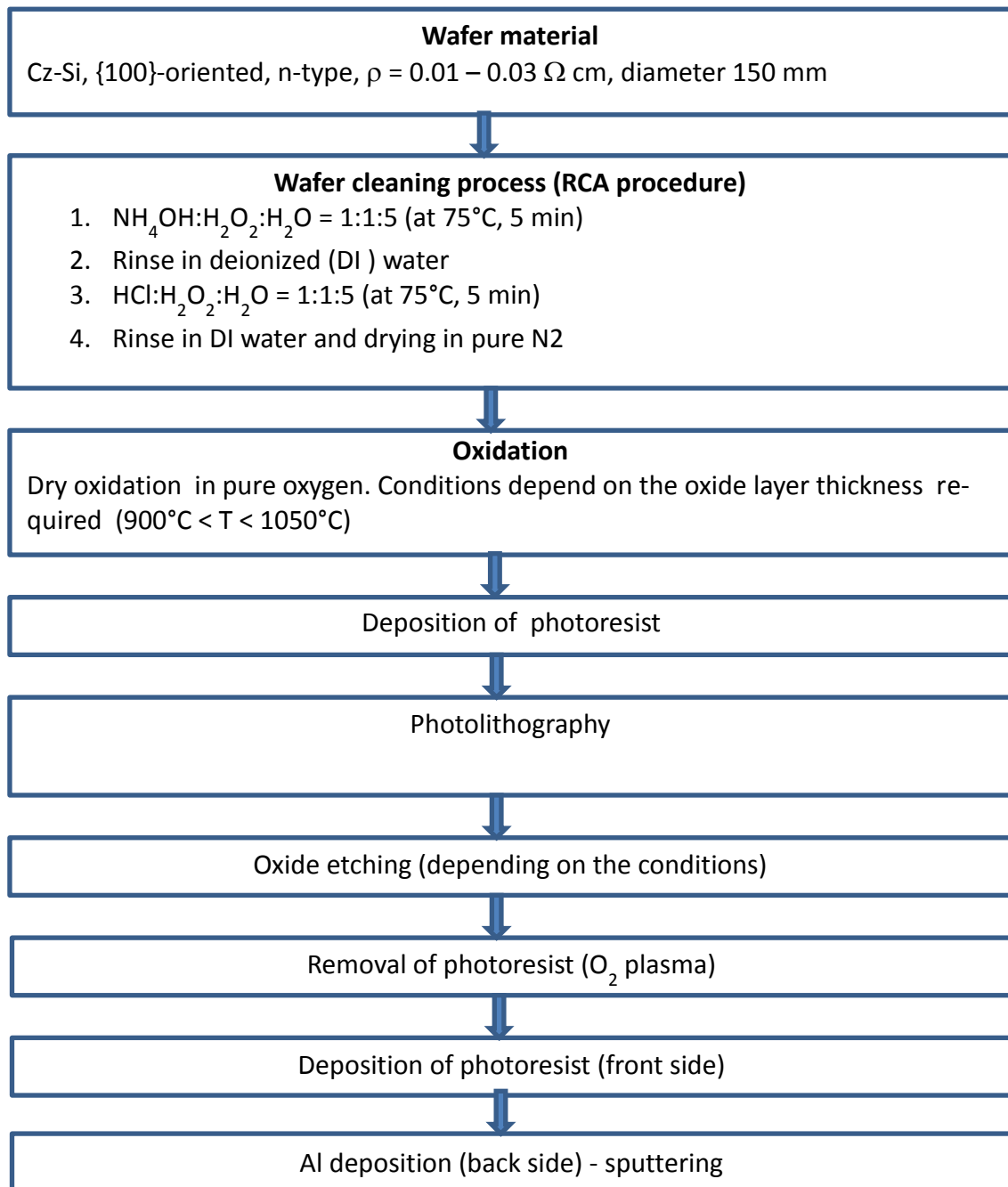
**Figure 3.8.** (a) A scheme of the cross-section of the sample capacitor assembled for dielectric measurements employing ultra-flat highly conductive silicon wafers as electrodes, and insulating silica nano-pillars as spacers; (b) optical microscope image of an array of silica nano-pillars embedded on a conductive silicon wafer; (c) tapping mode AFM height image of a spacer (height 110 nm, lateral dimension 5 μm); and (d) the corresponding profile of the height image.

A different approach [181] – developed about seven years ago, and recently improved to increase sensitivity – is schematically described in Figure 3.8. Here, ultra-flat (rms roughness of 2.3 Å as determined on a scan area of 1 μm<sup>2</sup>) and highly conductive (specific resistivity less than 3 mΩcm) silicon wafers are used as electrodes, and a regular matrix of insulating silica nano-pillars as spacers. The quadratic spacers having a lateral dimension of 5 μm, and variable height, in the range 35 – 1500 nm, are produced by thermal oxidation and optical lithography (see Scheme 3.1) on the surface of a conductive silicon wafer (at the Max Planck Institute for Microstructure Physics, Halle (Saale), Germany). On a second

conductive wafer, a thin polymer layer is deposited by spin coating from solution (under extra-clean conditions). After spin coating, the two wafer pieces (that is, one with the thin layer and the second one having silica nano-pillars) are brought in contact, and slightly pressed together using a spring. This delivers a capacitor inside which is the sample material with its upper interface free.

Figure 3.9 shows the dielectric response of an empty (i.e., without a polymer film) capacitor of the kind schemed in Figure 3.8a. It reveals that the dielectric response of the whole set-up is stable (given the concurrence between heating and cooling runs over a wide range of temperatures). Furthermore, it shows that the dielectric loss of the nanostructures is very low, and hence ultra-thin layers prepared from many polymeric (and low-molecular weight) materials, including those with low dielectric strengths, can be studied in this geometry. This approach therefore achieves a new possibility for broadband dielectric spectroscopy: the ability to measure interfacial molecular dynamics. It is instructive to note that a systematic adjustment of the interfacial interactions is readily possible as can be realized by controlled deposition of various metallic or organic layers [71] on the surface of the electrodes prior to deposition of the thin films. Recently, nano-pillars with heights as low as 35 nm were successfully produced, making it possible to study isolated polymer coils [147].

**Scheme 3.1.** The process of producing silica nanopacers



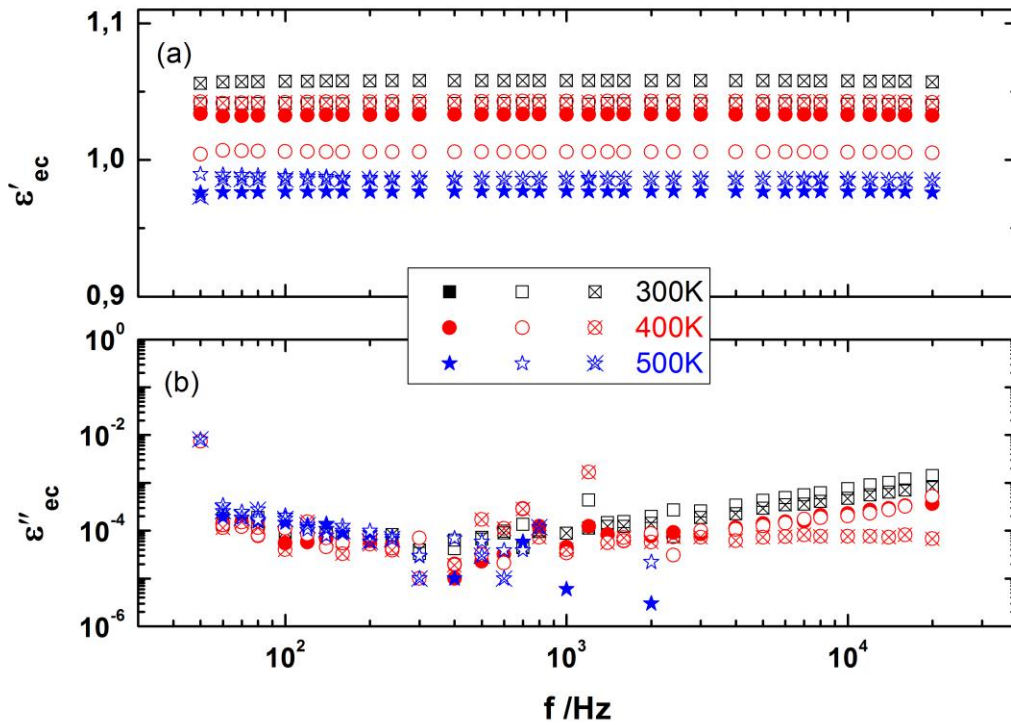


**Figure 3.9.** The real,  $\epsilon'_{ec}$ , and imaginary,  $\epsilon''_{ec}$ , parts of the complex permittivity as measured for an empty capacitor (assembled using nanostructured electrodes) recorded during subsequent heating (closed symbols), cooling (open symbols) and re-heating (crossed-symbols) runs.

### 3.3 Poly(*cis*-1,4-isoprene) (PI) in porous media

Aluminium can be oxidized by means of an electrochemical procedure which changes the surface chemistry of the metal to produce an anodic oxide layer. During this anodization process, a self-organized, highly ordered array of cylindrical shaped pores is produced (in dependence on oxidation parameters) with controllable pore diameters, periodicity and porosity [182,183]. Anodic aluminium oxide (AAO) membranes are therefore used as templates in a variety of nanotechnology applications because the need for expensive lithographical techniques is circumvented.

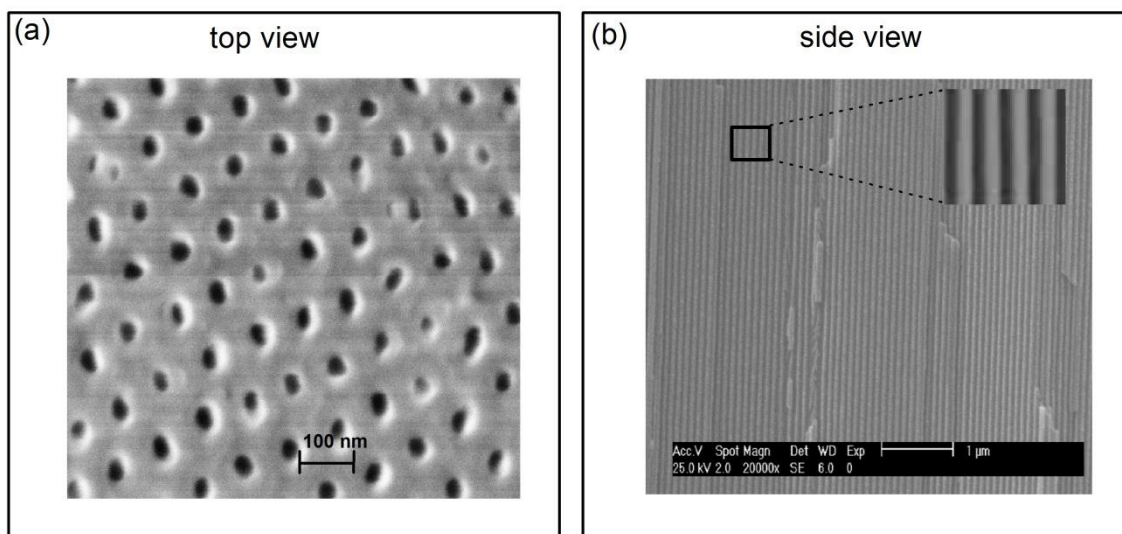


**Figure 3.10.** Scanning Electron Microscope images of an AAO membrane with pores having a mean diameter of 55 nm, viewed from the top (a), and from the side after cleaving along the pore direction (b). The first image displays the well-known hexagonal array of cylindrical pores [184], while the second demonstrates the uni-directional nature of the channels. The inset shows a zoom-in over a small area of the image.

AAO membranes with uni-directional pore channels (Fig. 3.10) were infiltrated with poly(cis-1,4-isoprene) for dielectric studies. The experimental procedure was carried out as follows: (i) the empty membrane was weighed before being annealed at 573 K for 24 h in oil-free high vacuum ( $10^{-6}$  mbar); (ii) the system was cooled down to 300 K to allow for injection of 0.5 ml of a PI/chloroform (23 vol% PI) onto the membrane (still in high vacuum); (iii) after 12 h of infiltration at 300 K, the membrane was annealed at 374 K for 1 h to remove solvent, and then (iv) cooled down again to 300 K for the next injection of solution. This was repeated over several days, and a filling factor (as determined from weight measurements) of  $\geq 70\%$  achieved in 6 days (for PI-53 in 55-nm pores). Figures 3.11 and 3.12, respectively, show schemes of the pore-filling procedure and vacuum (and annealing) chamber used in this work. The latter evacuates the sample chamber using a two-step se-

quence: initially, a membrane pump brings the pressure to the mbar level, before a turbomolecular system pumps down to the nano-bar range. By this method, a vacuum better than  $10^{-6}$  mbar is achieved, and the sample is not exposed to oil vapour via hydrocarbon backstreaming, as would be the case for conventional oil-based roughing pumps. Very significantly, the vacuum area can be accessed, without breaking it, via the natural rubber membrane using a sharp needle. The rubber membrane acts as a kind of *septum* through which solutions can be injected onto the AAO template, without exposure to oxygen or water vapour.

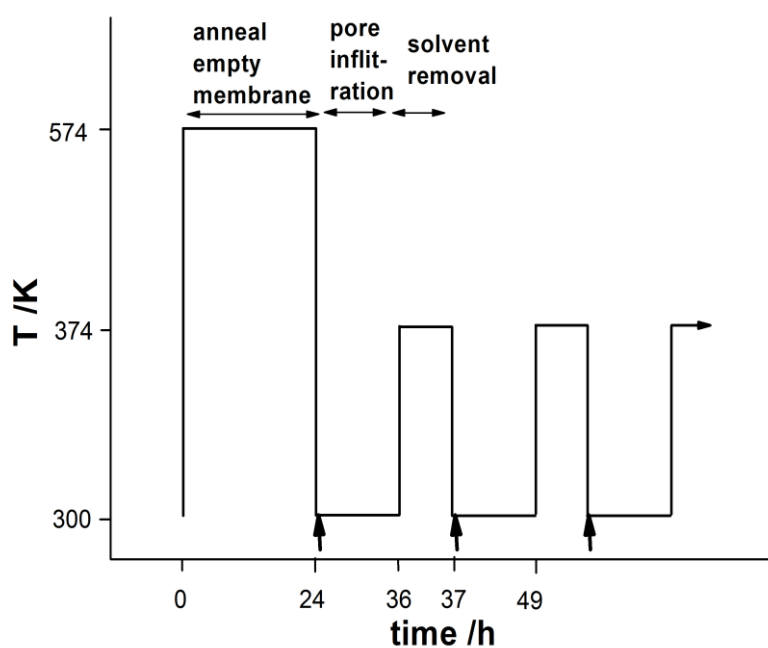


**Figure 3.11.** A scheme describing the fractionated pore-infiltration procedure applied in this work. The thick arrows show the instances when injection of the solution is made.

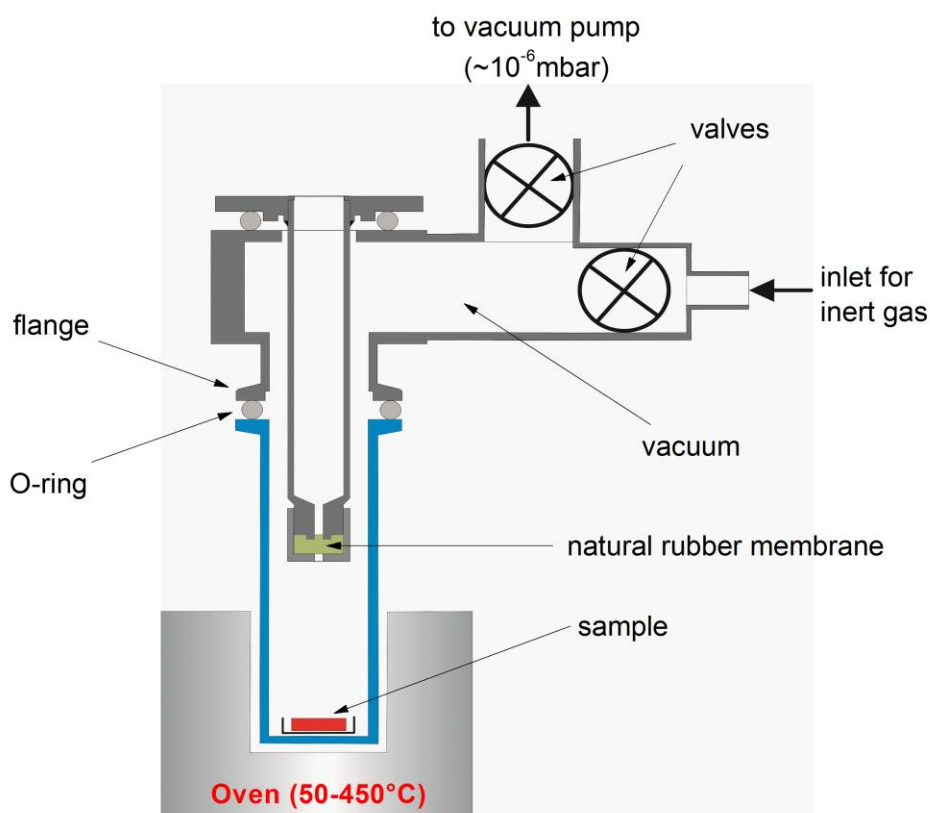


**Figure 3.12.** A custom-made<sup>1</sup> vacuum annealing chamber consisting of a two-step pumping system that employs a turbo molecular pump and an oil-free membrane pump. A wide range vacuum gauge is connected via four angle valves. The sample is placed in a chamber (made of fused silica glass) which is heated by an oven equipped with a temperature controller. Importantly, access into the vacuum (without breaking it) is gained via the natural rubber membrane using a sharp needle.

## 3.4 Experimental Techniques

### 3.4.1 Broadband Dielectric Spectroscopy (BDS)

Broadband dielectric spectroscopy (BDS) [12] probes the interaction of electromagnetic (EM) waves with matter in the frequency regime between  $10^{-6}$  and  $10^{12}$  Hz. This extraordinarily extended dynamic range covers the dispersion and absorption phenomena of molec-

<sup>1</sup> I am grateful to Wiktor Skokov for courteously preparing this schematic.

ular and collective dipolar relaxations, charge transport and polarization effects at inner and outer boundaries which determine the dielectric properties of the material under investigation. These processes, originate, respectively, from molecular reorientations of permanent dipole moments; electric conduction arising from the translational motions of electric charges (electrons, ions, holes); and, separation of charges at the interfaces (electrode or Maxwell-Wagner polarization). BDS therefore facilitates access to a wealth of information on the dynamics of bound (dipoles) and mobile charge carriers, depending on the details of the molecular system.

### 3.4.1.1 Polarization

The interaction of matter with EM fields is described by Maxwell's equations:

$$\text{rot } \mathbf{E} = -\frac{\partial \mathbf{B}}{\partial t} \quad (3.1)$$

$$\text{rot } \mathbf{H} = \mathbf{j} + \frac{\partial \mathbf{D}}{\partial t} \quad (3.2)$$

$$\text{div } \mathbf{D} = \rho_e \quad (3.3)$$

and

$$\text{div } \mathbf{B} = 0 \quad (3.4)$$

where  $\mathbf{E}$  and  $\mathbf{H}$  describe the electric and magnetic fields,  $\mathbf{D}$  the dielectric displacement,  $\mathbf{B}$  the magnetic induction,  $\mathbf{j}$  the current density and  $\rho_e$  the density of charges. For small electric field strengths ( $\leq 10^6$  V/cm),  $\mathbf{D}$  can be expressed by

$$\mathbf{D} = \varepsilon^* \varepsilon_0 \mathbf{E} \quad (3.5)$$

where  $\varepsilon^*$  is the complex dielectric function, and  $\varepsilon_0 (= 8.854 \times 10^{-12} \text{ As V}^{-1}\text{m}^{-1})$  is the permittivity of free space. According to Eqs. (3.1 – 3.4),  $\varepsilon^*$  is time (or frequency) dependent if time-dependent processes take place in the sample. For a periodic electrical field  $\mathbf{E}(t) = \mathbf{E}_0 \exp(i\omega t)$ , where  $\omega$  is the radial frequency, the complex dielectric function is given by

$$\varepsilon^*(\omega) = \varepsilon'(\omega) - i\varepsilon''(\omega) \quad (3.6)$$



where  $\varepsilon'(\omega)$  and  $\varepsilon''(\omega)$  are the real and imaginary parts of the complex dielectric function. The latter is also commonly referred to as the dielectric loss.

When an external field is applied to a dielectric, the material responds by undergoing a dielectric displacement, mainly characterized by the polarization,  $\mathbf{P}$ :

$$\mathbf{P} = \mathbf{D} - \mathbf{D}_0 = (\varepsilon^* - 1)\varepsilon_0\mathbf{E} = \chi^*\varepsilon_0\mathbf{E} \quad (3.7)$$

where  $\chi^* = (\varepsilon^* - 1)$  is the dielectric susceptibility of the material under the influence of an outer electric field. Generally, a macroscopic polarization  $\mathbf{P}$  is related to microscopic dipole moments  $\mathbf{p}_i$  of the molecules present within a volume  $V$  by

$$\mathbf{P} = \frac{\sum \mathbf{p}_i}{V} \quad (3.8)$$

Microscopic dipole moments – which arise when the electric centres of gravity of positive and negative charges of a molecule or particle do not match – can be divided into two categories: induced and permanent dipole moments. The former, which include electronic and atomic polarizations, result from the deformation of a neutral distribution of charges by local electrical fields,  $\mathbf{E}_{loc}$ . Their contribution to the total macroscopic polarization can be summarized in a common term denoted as  $\mathbf{P}_\infty$  and defined as

$$\mathbf{P}_\infty = \alpha n \mathbf{E}_{loc} = \frac{\rho N_A}{M} \alpha \mathbf{E}_{loc} \quad (3.9)$$

where  $\alpha$  represents the polarizability,  $n$  the dipole number density,  $\rho$  the density,  $N_A$  the Avogadro number, and  $M$  the molecular weight. For sufficiently small densities, the local electric field  $\mathbf{E}_{loc}$  can be approximated by the external electric field  $\mathbf{E}$ . For higher densities, shielding effects must be considered because the influence of the surrounding medium on a test dipole moment is no longer negligible. In this case, according to the calculations of Lorenz using a cavity model:

$$\mathbf{E}_{loc} = \mathbf{E} + a \frac{\mathbf{P}}{\epsilon_0} \quad (3.10)$$

where  $a = 1/3$  for a spherical cavity and a homogeneous dielectric material. In combination with Eqs. (3.7) and (3.9), Eq. (3.10) can be used to derive the relation between the static dielectric permittivity  $\epsilon_s$  and the polarizability  $\alpha$  (Clausius-Mosotti relation [185]):

$$\epsilon_s = \frac{1-2x}{1-x} \quad (3.11)$$

where  $x = n\alpha/3\epsilon_0$ .

The second contribution to the total macroscopic polarization, referred to as the orientational polarization, emanates from molecules or particles which possess permanent dipole moments which can be oriented in an external electric field:

$$\mathbf{P}_{or} = \frac{1}{V} \sum_i \mathbf{\mu}_i = \frac{N}{V} \langle \mathbf{\mu} \rangle \quad (3.12)$$

where  $N$  is the total number of dipoles,  $V$  the volume and  $\langle \mathbf{\mu} \rangle$  the mean dipole moment. Neglecting inertia effects on  $\mathbf{P}_{or}$  and assuming that the local electrical field is given by the external field, and that the dipoles do not interact with each other, the mean dipole moment is given only by a counterbalance between orientational polarization and thermal fluctuations. According to Boltzmann statistics, one gets:

$$\langle \mathbf{\mu} \rangle = \frac{\int_{4\pi} \mathbf{\mu} \exp\left(\frac{\mathbf{\mu} \cdot \mathbf{E}}{k_B T}\right) d\Omega}{\int_{4\pi} \exp\left(\frac{\mathbf{\mu} \cdot \mathbf{E}}{k_B T}\right) d\Omega} \quad (3.13)$$

where  $T$  is the temperature,  $k_B$  Boltzmann constant and  $d\Omega$  the differential space angle. The factor  $\exp\left(\frac{\mathbf{\mu} \cdot \mathbf{E}}{k_B T}\right) d\Omega$  gives the probability that the dipole moment vector has an orientation between  $\Omega$  and  $\Omega + d\Omega$ . Only the component of the dipole moment lying parallel to the direction of the outer electric field contributes to the polarization. For interaction energies smaller than the thermal energy ( $\mu E \ll k_B T$ ), the above expression is simplified to:

$$\langle \boldsymbol{\mu} \rangle = \frac{\mu^2}{3k_B T} \mathbf{E} \quad (3.14)$$

Inserting Eq. (3.14) into Eq. (3.12) yields

$$\mathbf{P}_{or} = \frac{\mu^2}{3k_B T} \frac{N}{V} \mathbf{E} \quad (3.15)$$

Further, using Eq. (3.7), the contribution of the orientational polarization to the dielectric function can be calculated as

$$\varepsilon_S - \varepsilon_\infty = \frac{1}{3\varepsilon_0} \frac{\mu^2}{k_B T} \frac{N}{V} \quad (3.16)$$

where  $\varepsilon_S = \lim_{\omega \rightarrow 0} \varepsilon'(\omega)$  while  $\varepsilon_\infty = \lim_{\omega \rightarrow \infty} \varepsilon'(\omega)$  covers all contributions to the dielectric function which are due to electronic and atomic polarization  $\mathbf{P}_\infty$  in the optical frequency range. If a term corresponding to the orientational polarization is included to Eq. (3.11), the Debye-formula is obtained:

$$\frac{\varepsilon_S - 1}{\varepsilon_S + 2} = \frac{1}{3} \frac{N_A}{\varepsilon_0} \frac{\rho}{M} \left[ \alpha + \frac{\mu^2}{3k_B T} \right] \quad (3.17)$$

Onsager [186] developed a reaction theory that provides an extension to the Debye-formula to account for polar molecules by considering the enhancement of the permanent dipole moment  $\mu$  of a molecule by the polarization of the environment (reaction field). Considering a test dipole in a spherical cavity, Onsager obtained

$$\varepsilon_S - \varepsilon_\infty = \frac{1}{3\varepsilon_0} \frac{N}{V} \frac{\mu^2}{k_B T} F \quad (3.18)$$

with

$$F = \frac{\varepsilon_s(\varepsilon_\infty + 2)^2}{3(2\varepsilon_s + \varepsilon_\infty)} \quad (3.19)$$

For polar associating liquids, the Onsager formula (i.e., Eq. (3.19)) fails because static orientation correlations (e.g. hydrogen bonding, steric interactions etc.) between molecules are not considered in its derivation. Hence the equation does not deliver correct values for the dipole moments for such liquids. This has been reconsidered by Kirkwood and Fröhlich [187,188] who introduced a correlation factor  $g$  in the Onsager formula:

$$\varepsilon_s - \varepsilon_\infty = \frac{1}{3\varepsilon_0} \frac{\mu^2}{k_B T} \frac{N}{V} F g \quad (3.20)$$

with

$$g = \frac{1}{N\mu^2} \langle \sum_i \boldsymbol{\mu}_i \sum_j \boldsymbol{\mu}_j \rangle = 1 + \frac{1}{N\mu^2} \langle \sum_i \sum_{i < j} \boldsymbol{\mu}_i \boldsymbol{\mu}_j \rangle = \frac{\mu_{interact.}^2}{\mu^2} \quad (3.21)$$

Here,  $\mu_{interact.}^2$  is the effective dipole moment when interactions are considered, and the angle brackets indicate the averaging over the whole system taking into account all interactions. This formula was simplified by considering a region containing  $\tilde{N}$  molecules which are treated explicitly. The remaining  $N - \tilde{N}$  molecules (which are outside the region) are considered as an infinite continuum whose dielectric behaviour is characterized by  $\varepsilon_s$ . In this case factor  $g$  is given by

$$g = 1 + \frac{1}{\tilde{N}\mu^2} \langle \sum_{i=1}^{\tilde{N}} \sum_{i < j} \boldsymbol{\mu}_i \boldsymbol{\mu}_j \rangle \quad (3.22)$$

The accuracy of this method can be improved by making  $\tilde{N}$  as large as needed. A first approach to calculate  $g$  is to take into account only the nearest neighbours of a selected test dipole. In that case,  $g$  is approximated by

$$g = 1 + z \langle \cos \psi \rangle \quad (3.23)$$

where  $z$  is the coordination number and  $\psi$  is the angle between the test dipole and a neighbour.

### 3.4.1.2 Dielectric relaxation

When a dielectric material is perturbed by a time dependent external electric field  $x(t) = E(t)$ , its response is the polarization  $y(t) = P(t)$ . For an isotropic system, the linear response theory provides that

$$\mathbf{P}(t) = \mathbf{P}_\infty + \varepsilon_0 \int_{-\infty}^t \varepsilon(t-t') \frac{d\mathbf{E}(t')}{dt'} dt' \quad (3.24)$$

where  $\varepsilon(t)$  is the time dependent dielectric function and  $\mathbf{P}_\infty$  covers all contributions arising from induced polarization. Eq. (3.24) is based solely on linearity and causality, that is, the assumption of the facts that the response of the system to two disturbances is the sum of the two single reactions, and that only disturbances in the past are responsible for the response at time  $t$ , respectively. If a stationary periodic disturbance  $\mathbf{E}(t)(\omega) = \mathbf{E}_0 \exp(-i\omega t)$  is applied to the system (where  $\omega$  is the angular frequency), Eq. (3.24) becomes

$$\mathbf{P}(t)(\omega) = \varepsilon_0(\varepsilon^*(\omega) - 1)\mathbf{E}(t)(\omega) \quad (3.25)$$

where  $\varepsilon^*(\omega) = \varepsilon'(\omega) - i\varepsilon''(\omega)$  is the complex dielectric function,  $\varepsilon'(\omega)$  and  $\varepsilon''(\omega)$  are, respectively, proportional to the energy stored reversibly in the system per period and the energy which is dissipated per period.  $\varepsilon^*(\omega)$  is related to  $\varepsilon(t)$  by

$$\varepsilon^*(\omega) = \varepsilon'(\omega) - i\varepsilon''(\omega) = \varepsilon_\infty - \int_0^\infty \frac{d\varepsilon(t)}{dt} \exp(-i\omega t) dt \quad (3.26)$$

Eq. (3.26) is a full imaginary Laplace transformation; consequently, the real and the imaginary part of the complex dielectric function are related to each other by the Kramers-Kronig relations [189]:

$$\varepsilon'(\omega) - \varepsilon_\infty = H[\varepsilon''(\omega)] = \frac{1}{\pi} \oint \frac{\varepsilon''(\xi)}{\xi - \omega} d\xi \quad (3.27a)$$

and

$$\varepsilon''(\omega) = -H[\varepsilon'(\omega) - \varepsilon_\infty] = -\frac{1}{\pi} \oint \frac{\varepsilon'(\xi) - \varepsilon_\infty}{\xi - \omega} d\xi \quad (3.27b)$$

The function  $H[ ]$  denotes the Hilbert transformation. Eq. (3.27) means that both  $\varepsilon'(\omega)$  and  $\varepsilon''(\omega)$  carry the same information, at least from an experimental point of view. The dielectric strength  $\Delta\varepsilon$  can be obtained directly by integrating the imaginary part:

$$\Delta\varepsilon = \varepsilon_s - \varepsilon_\infty = \frac{2}{\pi} \int_0^\infty \varepsilon''(\omega) d \ln \omega \quad (3.28)$$

Figure 3.13 is a scheme showing how – generally – the complex dielectric function depends on frequency in the spectral range covered by BDS (and optical spectroscopy). On the low frequency side, the first two peaks observed in dielectric loss  $\varepsilon''(\omega)$ , and the corresponding steps in  $\varepsilon'(\omega)$ , are related to relaxation processes whose origin is the microscopic fluctuations of permanent dipole moments in an external electric field. The contribution to the dielectric function displayed at frequencies above 1 THz is that of induced polarization.

As a result of stochastic thermal motions, thermodynamic quantities such as polarization fluctuate about their mean values. The fluctuation-dissipation theory advanced by Callen and Welton [190] provides the relationship between the response of a system to an external perturbation and the dipole thermal fluctuations in equilibrium. In the stationary state, the autocorrelation function,  $\Phi(t)$ , of the polarization is given by:

$$\Phi(t) = \frac{\langle \Delta P(t) \Delta P(0) \rangle}{\langle \Delta P^2(0) \rangle} \quad (3.29)$$

For classical systems,  $\Phi(t)$  is expressed as

$$\Phi(t) = -\frac{1}{k_B T} \frac{\varepsilon(t)-1}{\Delta\varepsilon} \quad (3.30)$$

Eq. (3.30) – in the framework of the linear response theory – relates the dielectric function, as the macroscopic response occasioned by a small (linear) external excitation, to the polarization in equilibrium.

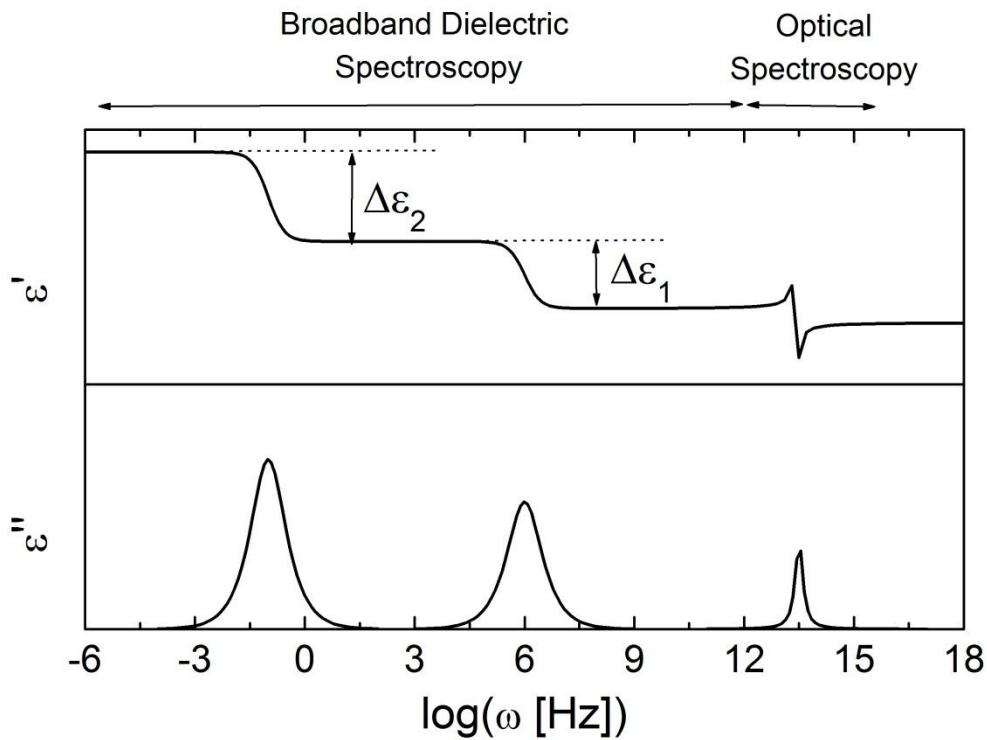


**Figure 3.13.** A schematic representation of the frequency-dependence of the real and imaginary parts of the complex dielectric permittivity,  $\varepsilon^*$ . Adapted from [12] with permission.

### 3.4.1.3 Debye relaxation

The most simplified ansatz – neglecting inertia effects and the interactions with neighbouring molecules – to calculate the time dependence of dielectric response is the assumption that the change of polarization is proportional to its actual value [191] so that

$$\frac{dP(t)}{dt} = -\frac{1}{\tau_D} P(t) \quad (3.31)$$

where  $\tau_D$  is a characteristic relaxation time. Solving eq. (3.31), one obtains

$$P(t) = P(0)e^{(-t/\tau_D)} \quad (3.32)$$

which leads to an exponential decay for the correlation function

$$\Phi(t) = e^{(-t/\tau_D)} \quad (3.33)$$

Eq. (3.33) does not fulfil the conditions demanded for a correlation function when  $t \rightarrow 0$ , and therefore, for short times, it should be replaced by other mathematical relationships, e.g., a Gaussian function. According to Eq. (3.26), the complex dielectric permittivity as a function of frequency can be obtained from the Fourier Transformation of the corresponding time-dependent function. Therefore for  $\varepsilon^*(\omega)$  one obtains the Debye equation:

$$\varepsilon^*(\omega) = \varepsilon_\infty + \frac{\Delta\varepsilon}{1+i\omega\tau_D} \quad (3.34)$$

whose real and imaginary parts are expressed as:

$$\varepsilon'(\omega) = \varepsilon_\infty + \frac{\Delta\varepsilon}{1+\omega^2\tau_D^2} \quad (3.35)$$

$$\varepsilon''(\omega) = \frac{\omega\tau_D\Delta\varepsilon}{1+\omega^2\tau_D^2} \quad (3.36)$$

Figure 3.14 exemplifies the Debye equation with the following parameters:  $\varepsilon_\infty = 2$ ,  $\Delta\varepsilon = 1.5$  and  $\tau_D = 10^{-2}$ . It is easy to notice that the maximum position of the peak in  $\varepsilon''$ , as well as the mid-point in the step of  $\varepsilon'$  are located at a frequency given by  $\omega = 1/\tau_D$ .



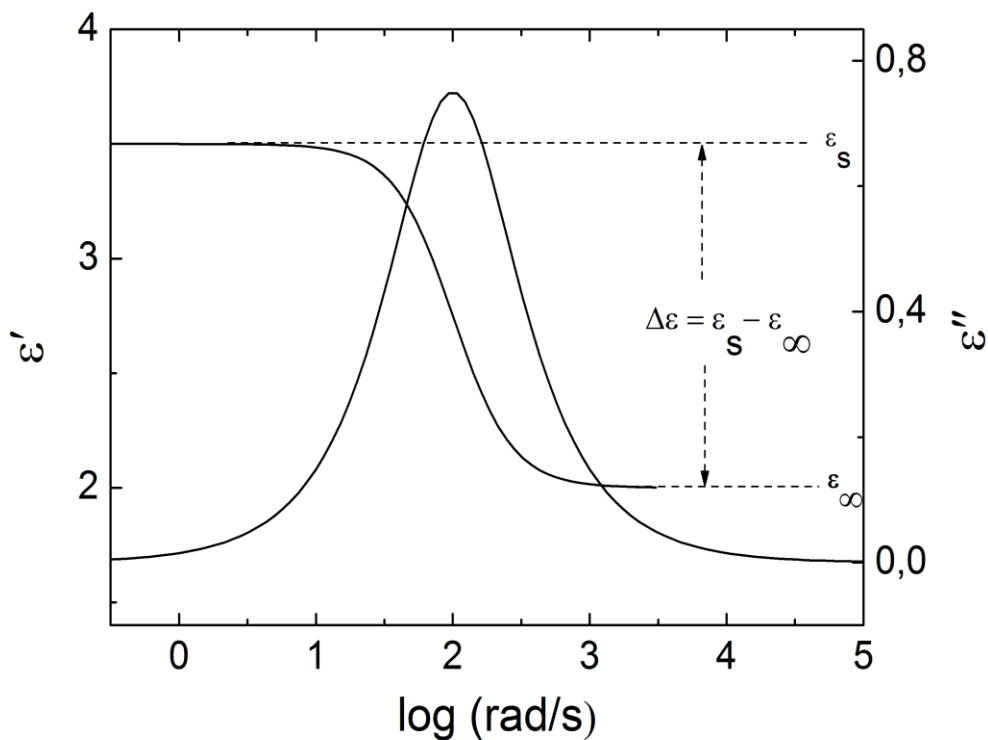


**Figure 3.14.** Real  $\varepsilon'$  and imaginary part  $\varepsilon''$  of the complex dielectric permittivity as functions of frequency for a Debye relaxation process.

There are several molecular models which justify Eq. (3.33); these include the simple double potential, the rotational diffusion, and the memory function models. A detailed discussion is available in [12].

#### 3.4.1.4 Non-Debye relaxation

It is uncommon to observe – in real experiments – relaxation processes that can be fully described by the Debye function. Usually, the measured dielectric functions are much broader than predicted by Eq. (3.33) or Eq. (3.34), and very often, asymmetric. The latter aspect means that the high frequency behaviour is more pronounced than the low frequen-

cy one. This then is what is referred to in literature as non-Debye or non-ideal dielectric relaxation behaviour. Although one may choose to express non-Debye behaviour by a superposition of several Debye functions with different relaxation times, this approach does not justify a molecular interpretation in accord with independent Debye-like relaxation processes [192]. Such an interpretation might be strictly true for special types of molecular motions (e.g. local molecular motions) where the dielectric response may be argued to originate from a distribution of different environments. However, it fails for relaxation processes which have a cooperative nature.

Several empirical model functions – most of which are generalizations of the Debye function – have been advanced to describe broadened and asymmetric loss peaks. These include the Cole-Cole ( $\epsilon_{CC}^*$ ) [193], the Cole-Davidson ( $\epsilon_{CD}^*$ ) [194] and Havriliak-Negami [195] ( $\epsilon_{HN}^*$ ) functions. A broadened dielectric function is described by the Cole-Cole equation as:

$$\epsilon_{CC}^*(\omega) = \epsilon_{\infty} + \frac{\Delta\epsilon}{1+(i\omega\tau_{CC})^{\beta}} \quad (3.37)$$

where  $0 < \beta \leq 1$  leads to a symmetrical broadening for the relaxation function compared to Eq. (3.34). For the case  $\beta = 1$ , the Debye function is recovered.  $\tau_{CC}^{-1} = 2\pi\nu_p = \omega_p$  is the Cole-Cole relaxation time (with  $\nu_p$  and  $\omega_p$  being the frequency and characteristic relaxation rate at maximum loss, respectively).

The complex dielectric function may also show an asymmetric broadening as is the case for many liquids and low molecular-weight glass-formers. This is well-captured by the Cole-Davidson formula which reads

$$\epsilon_{CD}^*(\omega) = \epsilon_{\infty} + \frac{\Delta\epsilon}{1+(i\omega\tau_{CD})^{\gamma}} \quad (3.38)$$

where the parameter  $\gamma$  ( which satisfies the condition  $0 < \gamma \leq 1$ ) describes an asymmetric broadening of the relaxation function for frequencies  $\omega > 1/\tau_{CD}$ ,  $\tau_{CD}$  being the Cole-Davidson relaxation time. For  $\gamma = 1$  the Debye function is recovered again.

The Havriliak-Negami model function – which is actually a combination of the Cole-Cole and Cole-Davidson equations – is more generalized and defines the complex dielectric response as

$$\varepsilon_{HN}^*(\omega) = \varepsilon_{\infty} + \frac{\Delta\varepsilon}{(1+[i\omega\tau_{HN}]^{\alpha})^{\beta}} \quad (3.39)$$

where  $\tau_{HN}$  is the Havriliak-Negami relaxation time. The real and the imaginary parts of Eq. (3.39) are:

$$\varepsilon' = \varepsilon_{\infty} + \frac{\Delta\varepsilon \cos \beta\phi}{\left[1+(\omega\tau_{HN})^{2\alpha}+2(\omega\tau_{HN})^{\alpha} \cos\left(\frac{\pi\alpha}{2}\right)\right]^{\frac{\beta}{2}}} \quad (3.40)$$

$$\varepsilon'' = \frac{\Delta\varepsilon \sin(\beta\phi)}{\left[1+(\omega\tau_{HN})^{2\alpha}+2(\omega\tau_{HN})^{\alpha} \cos\left(\frac{\pi\alpha}{2}\right)\right]^{\frac{\beta}{2}}} \quad (3.41)$$

where

$$\phi = \arctan \left\{ \frac{(\omega\tau_{HN})^{\alpha} \sin\left(\frac{\pi\alpha}{2}\right)}{1+(\omega\tau_{HN})^{\alpha} \cos\left(\frac{\pi\alpha}{2}\right)} \right\} \quad (3.42)$$

The fractional parameters  $\alpha$  and  $\beta$  describe, respectively, the symmetric and asymmetric broadening of the complex dielectric function, and satisfy the condition  $0 < \alpha, \alpha\beta \leq 1$ .

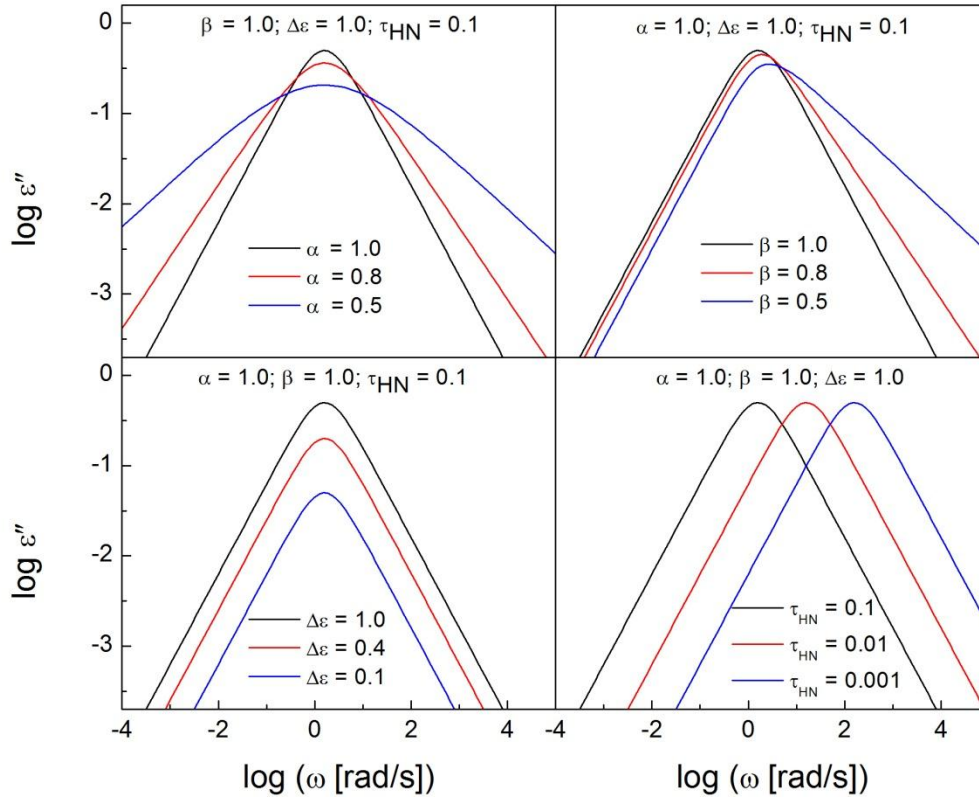


**Figure 3.15.** The Havriliak-Negami function and its dependence on the parameters  $\alpha$ ,  $\beta$ ,  $\Delta\varepsilon$  and  $\tau_{HN}$ .

These parameters are also related to the asymptotic behaviour of the complex dielectric permittivity at low and high frequencies (with respect to the position of maximum loss) by:

$$\varepsilon_s - \varepsilon'(\omega) \sim \omega^\alpha \text{ and } \varepsilon''(\omega) \sim \omega^\alpha \text{ for } \omega\tau_{HN} \ll 1, \quad (3.43)$$

$$\varepsilon'(\omega) - \varepsilon_\infty \sim \omega^{-\alpha\beta} \text{ and } \varepsilon''(\omega) \sim \omega^{-\alpha\beta} \text{ for } \omega\tau_{HN} \gg 1. \quad (3.44)$$

The position of maximum loss,  $\tau_{max}$  is related to  $\tau_{HN}$  by:

$$\tau_{max} = \tau_{HN} \left[ \frac{\sin\left(\frac{\alpha\beta\pi}{2+2\beta}\right)}{\sin\left(\frac{\alpha\pi}{2+2\beta}\right)} \right]^{1/\alpha} \quad (3.45)$$

Figure 3.15 illustrates the shape of the HN model function in dependence on the four parameters  $\alpha$ ,  $\beta$ ,  $\Delta\varepsilon$  and  $\tau_{HN}$ .

### 3.4.1.5 Dielectric data in the time domain

Dielectric relaxation measurements of materials are predominantly carried out in alternating fields, i.e., the frequency domain. However, some investigations demand measurements at very low frequencies ( $f \ll 1$  Hz); it turns out that classical alternating current methods are very slow in the frequency range below 1 Hz, and that in this range too, the dielectric loss becomes dominated by the conductivity of the sample. For these reasons, it is preferable to study the dielectric response in the time domain by measuring the depolarization current  $I(t)$  after switching off the electric field at  $t = 0$ .  $I(t)$  is related to the time dependent dielectric permittivity  $\varepsilon(t)$  by

$$I(t) = C_0 V_0 \frac{d\varepsilon(t)}{dt} \quad (3.46)$$

where  $C_0$  and  $V_0$  are, respectively, the geometric capacitance of the sample, and the height of the applied step voltage. Within the framework of the linear response theory,  $d\varepsilon(t)/dt$  is related to  $\varepsilon^*(\omega)$  by [196]:

$$\frac{d\varepsilon(t)}{dt} = L^{-1}[\varepsilon^*(\omega) - \varepsilon_\infty] = \frac{1}{\pi} \int_0^\infty [\varepsilon^*(\omega) - \varepsilon_\infty] e^{i\omega t} d\omega \quad (3.47)$$

One can therefore describe non-Debye relaxation in the time domain by using a function obtained from the inverse Laplace transformation of the Havriliak-Negami equation, which reads:

$$\frac{d\varepsilon(t)}{dt} = \frac{1}{\pi} \int_0^{\infty} \frac{\Delta\varepsilon}{[1+(i\omega t)^\alpha]^\beta} e^{i\omega t} d\omega \quad (3.48)$$

Eq. (3.48) – a model function with four fit parameters – cannot be analytically solved; however, a numerical evaluation has been presented by Schönhals [197].

Alternatively, time-domain non-Debye relaxation can be described by the empirical Kohlrausch-Williams-Watts (KWW) [15] function:

$$\varepsilon(t) = \varepsilon_\infty + \Delta\varepsilon \left[ 1 - \exp\left(-\frac{t}{\tau_{KWW}}\right)^{\beta_{KWW}} \right] \quad (3.49)$$

or

$$\frac{d\varepsilon(t)}{dt} = \Delta\varepsilon \left(\frac{t}{\tau_{KWW}}\right)^{\frac{1}{\beta_{KWW}} - 1} \frac{\beta_{KWW}}{\tau_{KWW}} \exp\left(-\frac{t}{\tau_{KWW}}\right)^{\beta_{KWW}} \quad (3.50)$$

where the stretched exponential parameter  $\beta_{KWW}$  accounts for the asymmetric broadening of  $\varepsilon(t)$  at shorter times compared to an exponential decay (i.e.  $\beta_{KWW} = 1$ ), and  $\tau_{KWW}$  is the corresponding relaxation time.

### 3.4.1.6 Conductivity contribution

In many cases, dielectric materials have a non-negligible electrical conductivity arising from mobile charge carriers, that is, the translational diffusion of electrons, ions or holes. As a result, a current density  $j$  builds up in the material, which according to Ohm's law, is written as  $j = \sigma^*(\omega)E$ , where  $\sigma^*(\omega) = \sigma'(\omega) - i\sigma''(\omega)$  is the complex conductivity. Applying Maxwell's equation for current density (Eq. (3.2)), one obtains:

$$\sigma^*(\omega) = i\omega\varepsilon_0\varepsilon^*(\omega) \quad (3.51)$$

which can be separated into:

$$\sigma'(\omega) = \omega \varepsilon_0 \varepsilon''(\omega) \quad (3.52)$$

$$\sigma''(\omega) = \omega \varepsilon_0 \varepsilon'(\omega) \quad (3.53)$$

For pure electronic conduction, there is no contribution to the real part of the complex permittivity while  $\varepsilon''(\omega) = \sigma_0/\varepsilon_0\omega$ , where  $\sigma_0$  is the dc-conductivity. Because of phenomena like electrode- or Maxwell-Wagner-polarization arising due to ionic charge carriers, the relation  $\varepsilon''(\omega) \sim 1/\omega$  does not hold anymore, but instead  $\varepsilon''(\omega) \sim 1/\omega^s$ , with  $s$  being less than unity. The total dielectric loss is therefore a sum of two terms: a conductivity term and another containing the contribution of all dipolar relaxation processes:

$$\varepsilon''(\omega) = \frac{\sigma_0 a}{\varepsilon_0 \omega^s} + \sum_j \text{Im} \left[ \frac{\Delta \varepsilon_j}{\left\{ 1 + (i\omega\tau_{HN}^j)^{\alpha_j} \right\}^{\beta_j}} \right] \quad (3.54)$$

where  $a$  is a factor having the dimensionality of  $1/\text{Hz}$ .

### 3.4.1.7 The distribution of relaxation times

The characteristic frequencies or times which contribute to the measured dielectric response can also be expressed in terms of the relaxation time distribution  $G(\ln \tau)$ . For Debye-relaxations, the complex dielectric function is related to  $G(\ln \tau)$  by

$$\varepsilon^*(\omega) - \varepsilon_\infty = \Delta \varepsilon \int_{-\infty}^{\infty} \frac{G(\ln \tau)}{1 + i\omega\tau} d \ln \tau \quad (3.55)$$

with  $G(\ln \tau)$  fulfilling the normalization condition:  $\int_{-\infty}^{\infty} G(\ln \tau) d \ln \tau = 1$ .

For non-Debye relaxations, the function  $G(\ln \tau)$  can be analytically derived from the Cole-Cole, Cole-Davidson, Havriliak-Negami or Kohlrausch-Williams-Watts functions expressions. The last two which are the most commonly used, respectively, provide that [12,198]:

$$G(\ln \tau)_{HN} = \frac{(\sin(\beta\theta))/\pi}{\left[1+2\left(\frac{\tau}{\tau_{HN}}\right)^\alpha \cos\left(\frac{\pi\alpha}{2}\right)+\left(\frac{\tau}{\tau_{HN}}\right)^{2\alpha}\right]^{\beta/2}} \quad (3.56)$$

where  $\theta = \frac{\pi}{2} - \tan^{-1} \left( \frac{(\tau_{HN}/\tau)^\alpha + \cos(\pi\alpha)}{\sin(\pi\alpha)} \right)$

$$G(\ln \tau)_{KWW} = \frac{1}{\pi} \int_0^\infty e^{-x} e^{-u \cos(\pi\beta_{KWW})} \sin[u \sin(\pi\beta_{KWW})] dx \quad (3.57)$$

with  $u = \left( \frac{x\tau}{\tau_{KWW}} \right)^{\beta_{KWW}}$

### 3.4.1.8 BDS – Summary

In conclusion, broadband dielectric spectroscopy – the main experimental technique for the current work – measures the molecular dynamics (and charge transport) of polar materials in a wide frequency range. One of the most important applications of dielectric spectroscopy is its use for investigating relaxation processes which are due to rotational fluctuations of molecular dipoles. Since these are related to characteristic parts of the molecule (e.g. functional groups) or to the whole molecule, a wealth of information about the dynamics of the molecular ensemble is obtained by analysing the dielectric function. The essential quantities which characterize a dielectric relaxation process are: the frequency of maximal loss (which is related to the characteristic relaxation time of the fluctuating dipoles); the shape of the loss peak (from which the distribution of the relaxations times can be deduced) and the dielectric strength of the relaxation process (which is a measure of the number density of fluctuating units).



### 3.4.2 Spectroscopic Ellipsometry (SE)

Ellipsometry is a very sensitive, non-destructive and indirect measurement technique that uses polarized light to characterize thin films, surfaces, and material microstructure. Usually, the polarization of light changes upon reflection; these changes are measured by an ellipsometer and interpreted on the basis of model calculations. The change in the state of polarization is a direct consequence of interference within the system. It is captured by the so-called ellipsometric angles  $\Delta$  and  $\Psi$ . In this section, a brief review of the basic theory [199,200] underlying ellipsometry is presented.

The complex refractive index  $N^* = n - ik$  is related to the dielectric function  $\varepsilon^*$  of a material by

$$\varepsilon^* = N^{*2} \quad (3.58)$$

so that (using Eq. (3.6)) the real and imaginary parts can be expressed as:

$$\varepsilon' = n^2 - k^2 \quad (3.59a)$$

$$\varepsilon'' = 2nk \quad (3.59b)$$

where  $n$  is the real index of refraction while  $k$  is the extinction coefficient of the medium. If the propagation direction of an electromagnetic wave is chosen to be the  $z$ -axis of a Cartesian coordinate system, then the electric field of the electromagnetic plane can be written as

$$\mathbf{E}(z, t) = \mathbf{E}_0 e^{[i\omega N^* (\frac{z}{c} - t)]} \quad (3.60)$$

where  $c$  is the velocity of propagation of plane waves and  $\mathbf{E}_0$  is a complex vector in the  $x$ - $y$  plane whose components, in general, have amplitude and phase terms to represent a polarized electromagnetic plane wave of angular frequency  $\omega$ . Taking  $x$  and  $y$  to be orthogonal

vectors in the Cartesian coordinate system,  $\mathbf{E}_0$  – which determines the polarization state of the wave in the  $x$ - $y$  plane – can be expressed as

$$\mathbf{E}_0 = E_{0x}e^{(i\varphi_x)x} + E_{0y}e^{(i\varphi_y)y} \quad (3.61)$$

where  $\varphi_x$  and  $\varphi_y$  represent the absolute phases of the electric field components  $E_x$  and  $E_y$ , respectively, at  $z = 0$  and  $t = 0$ .

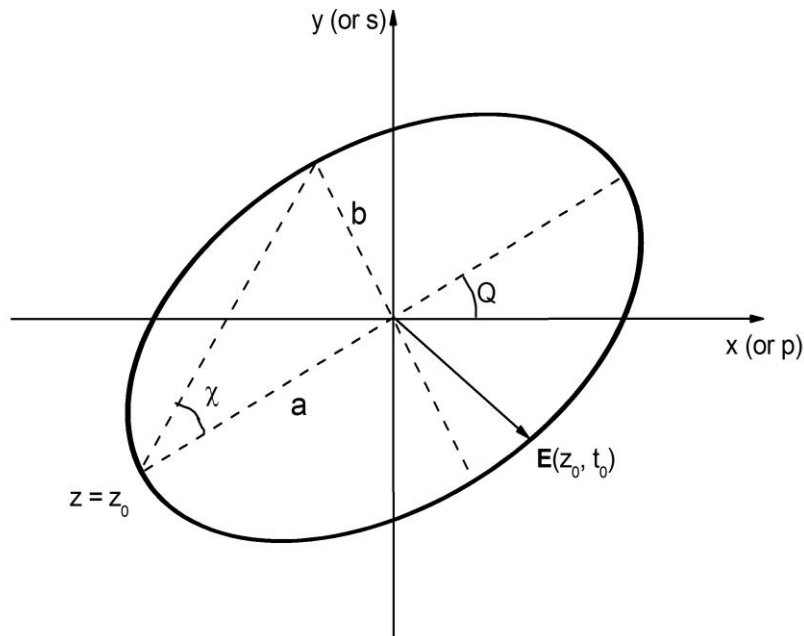


**Figure 3.16.** A schematic representation of the electric field vector trajectory  $\mathbf{E}(z_0, t)$  for an elliptically polarized light wave. For a given  $z = z_0$ ,  $\mathbf{E}$  traces out an ellipse over time. The sense of rotation determines whether the wave exhibits left or right polarization.  $Q$  is the tilt angle between the ellipse major axis  $a$  and the  $x$ -axis, measured in a counterclockwise-positive sense while facing the source of the light beam.  $\chi$  is the ellipticity angle given by  $\tan^{-1}(b/a)$ .

In its most general progression, the electric field of a plane wave of light propagating along the  $z$ -direction, as given by Eqs. (3.59) and (3.61), traces out an ellipse in the  $x$ - $y$  plane as a

function of time  $t$ , at a fixed point in space,  $z = z_0$  as sketched in Figure 3.16. The two special cases of polarization are: (i) linear polarization with  $\varphi_x = \varphi_y$ , and (ii) circular polarization where  $\varphi_x = \varphi_y \pm \pi/2$  and  $E_{0x} = E_{0y}$ . The most general polarization state can be described by an ellipse having the tilt angle  $Q$  ( $-90^\circ < Q < 90^\circ$ ) between its major axis and the  $x$ -axis, and the ellipticity angle determined by the ratio  $\chi$  ( $= \tan^{-1}[b/a]$ ) of the minor axis,  $b$ , to the major axis,  $a$ . This ratio lies in the range  $-45^\circ \leq \chi \leq 45^\circ$ .

By convention in ellipsometry, the arbitrary orthogonal coordinates  $x$ - $y$  are redefined to those based on the plane of incidence in a (non-normal) reflection experiment. The electric field, conventionally as well, is resolved into  $p$ - and  $s$ -components, parallel and perpendicular, respectively, to the plane of incidence, as shown in Figure 3.17. Hence, in this  $p$ - $s$  coordinate system, the effect of a specularly reflecting surface on an incident plane electromagnetic wave can be described by the complex amplitude whose reflection coefficients are defined as:

$$r_p = |r_p| e^{(i\varphi_p)} = \frac{E_p^r}{E_p^i} \quad (3.62)$$

$$r_s = |r_s| e^{(i\varphi_s)} = \frac{E_s^r}{E_s^i} \quad (3.63)$$

where  $E$  and  $\varphi$  represent the complex electric field components and the phase shifts due to reflection, respectively. The superscripts  $i$  and  $r$  denote the incident and reflected fields of the corresponding waves. In reflection ellipsometry, the ratios of the  $p$  and  $s$  reflection coefficients are of interest rather than their absolute values. Thus, the complex amplitude reflection ratio  $\rho_r^*$  is defined as:

$$\rho_r^* \equiv \frac{r_p}{r_s} = \frac{|r_p|}{|r_s|} \exp[i(\varphi_p - \varphi_s)] \quad (3.64)$$

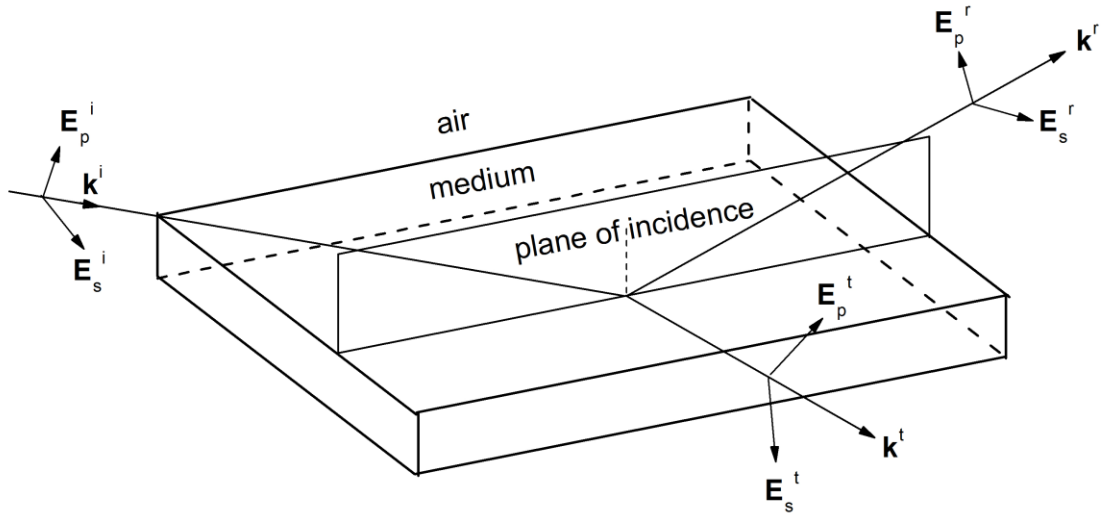


**Figure 3.17.** A schematic representation of the plane of incidence showing the propagation vectors (incident), (transmitted) and reflected. This scheme demonstrates the definition of  $p$ - and  $s$ -polarized waves.

The complex quantity  $\rho_r^*$  can be described in terms of the well-known ellipsometric angles ( $\Psi, \Delta$ ) which define the relative ( $p$ -to- $s$ ) field amplitude ratio ( $\tan \Psi$ ) and the phase shift difference ( $\Delta$ ) between the  $p$  and  $s$  waves:

$$\rho_r^* = \tan \Psi \exp(i\Delta) \quad (3.65)$$

where

$$\tan \Psi = \frac{|r_p|}{|r_s|} \text{ and } \Delta = \varphi_p - \varphi_s.$$

### 3.4.3 AC-Chip Calorimetry (ACC)

Conventional Differential Scanning Calorimetry (DSC) – until recently, an experimental tool limited to bulk samples – has been extended (especially by the Groups of Prof. Allen [83,84,201] and Prof. Schick [92–94]) to make it a very sensitive technique capable of measuring a few nanograms of matter, and hence suitable for investigations of confined systems. Differential AC-chip calorimetry, one of the several variants of approaches now developed - is based on the thermal behaviour of a single sensor under non-adiabatic conditions. For this, the apparent heat capacity is given by

$$C_{ap}(\omega) = \frac{P_0}{i\omega T_A} \quad (3.66)$$

where  $P_0$  is the amplitude of the applied power at the frequency  $\omega$  and  $T_A$  is the complex amplitude of the temperature modulation. If one considers a chip calorimeter based on a thin (so thin that heat transfer through the gas is dominant, and lateral transfer through the membrane can be ignored in a first approximation) membrane in a gas surrounding, then the heat flux through the system can be solved to get the temperature modulation amplitude of the heated membrane as:

$$T_A(\omega) = \frac{P_0}{(i\omega C + H_{ec})} \quad (3.67)$$

where  $C$  is the total heat capacity of the sample with the addenda,  $H_{ec}(= 4\pi r_0 \lambda_g)$  is the heat exchange coefficient,  $r_0$  being the radius of the heated area (which is small compared to the lateral dimension of the membrane, and the distance from the heater to the nearest boundary), and  $\lambda_g$  the thermal conductivity of the gas. Using Eqs. (3.66) and (3.67), one finds that

$$C_{ap} = C + \frac{H_{ec}}{i\omega}. \quad (3.68)$$

The second term in Eq. (3.68) describes the heat loss through the surrounding gas medium. Further contributions to  $C_{ap}$  can be determined as proven in [92]. In terms of measured quantities, the heat capacity of the sample,  $C_s$ , for the non-ideally symmetric system is given by

$$C_s = [\Delta U - \Delta U_0] \frac{i\omega \cosh(\alpha_0) \tilde{c}^2}{SP_0} \quad (3.69)$$

where  $U$  is the voltage amplitude at the thermopile;  $\Delta U_0$  and  $\Delta U$  are, respectively, the differential thermopile signals for two empty sensors, and for the case with the sample; the factor  $\cosh(\alpha_0)$  accounts for the difference between the measured temperature and the actual temperature of the sample because of the distance between the heater and the thermopile; and  $S$  is the thermopile sensitivity. The sensitivity of the thermopile and the heat exchange coefficient  $H_{ec}$  are obtained simultaneously for any fixed temperature from frequency-dependent measurements.

In the current measurements, the differential AC calorimeter is based on a commercially available pressure gauge (Xensor Integrations) (see Figure 3.18a). A small heater – around which are arranged six hot junctions of a thermopile – is placed in the centre of a free-standing 0.5- $\mu\text{m}$ -thick. For protection, the heater, thermopile and conducting stripes are covered by 0.7- $\mu\text{m}$  silicon oxide layer. The sample (a polymer layer) is spread over the whole sensor by spin coating. Figure 3.18b shows a scheme of the electrical setup of the device. The heaters on the chips are driven by an alternating current at frequency  $\omega/2$  from the oscillator of the lock-in amplifier, resulting in an oscillating power with frequency  $\omega$ . The amplitude and phase of the resulting oscillating temperature (with frequency  $\omega$ ) is measured with the thermopile using a digital lock-in amplifier. The oscillator voltage is applied to the two sensors and a known constant resistor  $R$  in series. The applied power is then calculated from the voltage over  $R$  (measured by a digital multimeter) taking the oscillator voltage and its internal resistance into account. All measurements were carried out in a dry nitrogen atmosphere.

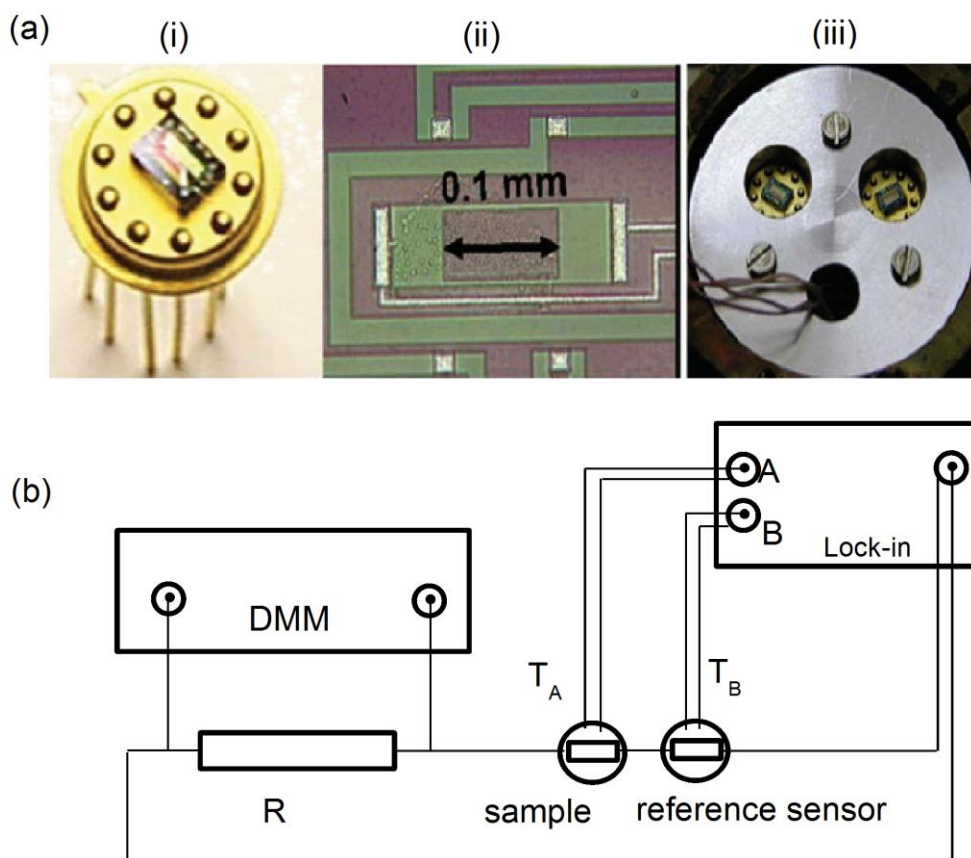


**Figure 3.18.** (a) The Chip sensor for the AC calorimeter. Picture (i) shows the thermal conductive vacuum gauge from Xensor Integrations; (ii) is a magnified centre area of the membrane which has a heater and four hot junctions of the thermopile (bright squares); (iii) the chip sensors mounted in the differential setup. (b) Schematic representation of the electric setup. Using the internal generator of the lock-in amplifier results in better phase stability. The differential signal A–B of the thermopiles is analyzed and further processed. The voltage over the known resistor  $R$  is measured with a digital multimeter (DMM) in order to calculate heater power. Adopted from [92] with permission.

Figure 3.19 shows exemplary data for a 100-nm *cis*-polyisoprene ( $M_w = 53\,000$  g/mol) thin layer measured isothermally at a frequency of 160 Hz, and how the dynamic glass transition temperature is obtained.

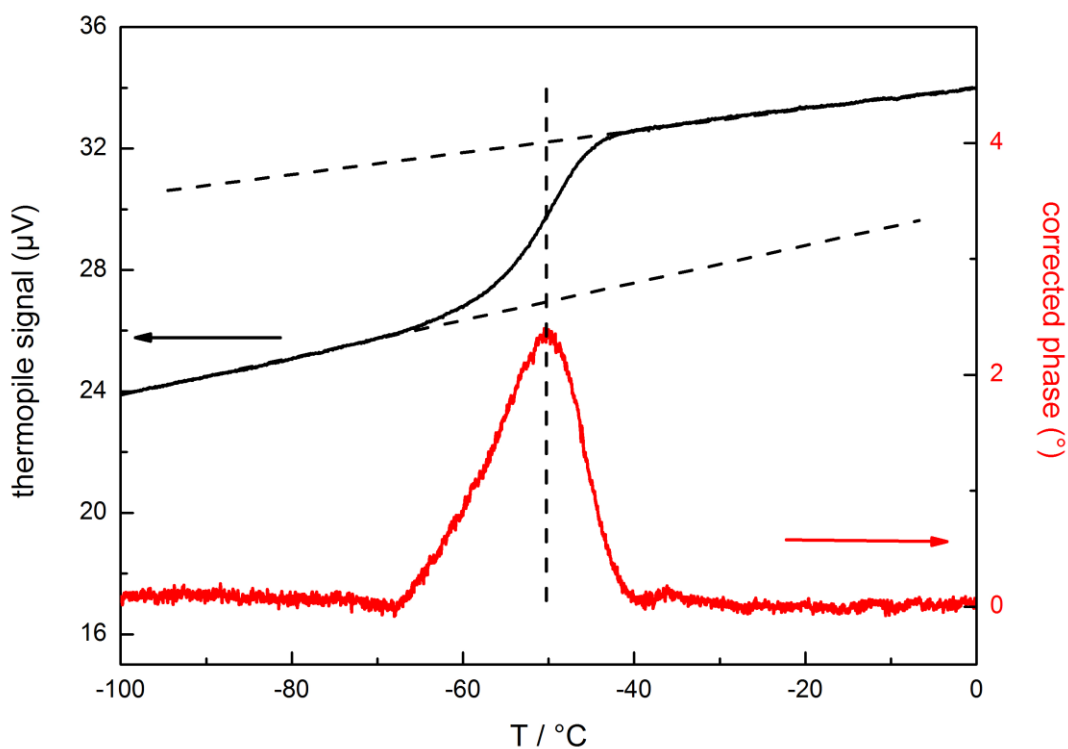


**Figure 3.19.** Temperature dependence of the thermopile signal and the (corrected) phase angle as measured at a frequency of 160 Hz for a 100-nm-thin *cis*-polyisoprene layer. The measurement was carried out a heating rate of 1 K/min. The dynamic glass transition temperature is obtained as the peak maximum in the phase, or the half-step in the thermopile signal (indicated by the vertical dashed line). Adopted from [146] with permission.



# 4 Results and Discussion

---

In this chapter, the dielectric properties of a low-molecular weight and several polymeric glass formers – under conditions of confinement – are investigated in broad frequency and temperature ranges. The main techniques utilized are Broadband Dielectric Spectroscopy, Spectroscopic vis-Ellipsometry, chip AC Calorimetry and Differential Scanning Calorimetry. Additionally, Atomic Force Microscopy is employed to check the surface topography and determine layer thickness – the major variable parameter in these investigations – for all studied samples. Both qualitative and quantitative understanding of the observed effects arising from confinement is presented. Glassy as well as chain dynamics are analyzed with reference to the behaviour in the corresponding unperturbed bulk system, and discussed in the context of the on-going worldwide debate on dynamics in confinement.

## 4.1 Effect of sample geometry on the measured dynamics

### 4.1.1 Introduction

In order to investigate matter by means of Broadband Dielectric Spectroscopy, one has to assemble the sample of interest as part of a capacitor, with the immediate consequence being that the material being probed comes in contact with the electrodes. For thin films, when the nanometric length scale is approached, this becomes a technologically demanding task. The conventional approach to solving this problem involves sandwiching the thin layer between two evaporated (and conductive) metal electrodes (Fig.3.1). This is a fairly simple procedure and has been used by the majority of researchers in this field [e.g., 1–4]. It must, however, be noted that the evaporation of a metal involves emission of great amounts of thermal energy; the possibility that this energy may harm the chemical structure of the soft matter (e.g. polymer) under study is real, but not substantively investigated. Besides, the evaporated metal electrodes penetrate the surface of the polymer layer to some extent, thereby causing electrical short cuts if the polymer layer falls below a certain thickness (typically ~10 nm). Recently, a new approach to assembling the capacitor for dielectric investigations was developed [181,202]; it entails the use of ultra-flat highly conduc-

tive silicon wafers with insulating silica nano-pillars employed as spacers (Fig. 3.2). Importantly, this technique circumvents the need for evaporating metal electrodes, and – given the free (upper) interface – makes it possible to study ultra-thin films, or even isolated polymer chains. For simplicity, the first approach is referred to as “capped” while the second one is “uncapped”. In this Section, polystyrene (PS) thin layers are studied in both geometries, and straight-forward comparisons, calculations<sup>2</sup> and discussions made to vividly unravel the effect of sample geometry on the measured (total) dielectric response.

#### 4.1.2 Experimental details

Atactic polystyrene (PS-300) (molecular weight  $M_w = 319$  kg/mol, with a polydispersity index of 1.05) and toluene (Sigma-Aldrich; purity  $\geq 99.8\%$ ; used as solvent), were purchased, respectively, from Scientific Polymer Products and Sigma-Aldrich, and used as received. Thin films were prepared by spin-casting the solutions at a constant rate of 3000 rpm, while the thickness was systematically scaled down by reducing the concentration of polystyrene in toluene. All solutions were filtered through the 200-nm pores of polytetrafluoroethylene (PTFE) membranes (Merck Millipore). The substrates for the capped and uncapped geometries were cleaned as described in Sections 3.1.1 and 3.1.2. For both geometries, the films were always annealed at 425 K ( $\sim T_g^{bulk} + 50$  K) for at least 24 h in a high oil-free vacuum ( $10^{-6}$  mbar) before dielectric measurements, to avoid effects of remaining solvent. Dielectric measurements were carried out using an Andeen-Hagerling 2700A impedance bridge which has an accuracy of  $\leq 10^{-5}$  in  $\tan(\delta)$ , corresponding to an error in the dielectric loss,  $\epsilon''_{total}$ , smaller than the symbol size in all presentations. For the temperature regulation, a Quatro System (Novocontrol) was applied ensuring a relative error of  $\leq 0.1$  K and an absolute error of less than 2 K.

---

<sup>2</sup> First calculations were performed by Dipl. Phys. Martin Treß in a joint project on polystyrene in confinement. A detailed consideration is available in his PhD dissertation to be published in December 2014.

### 4.1.3 Results and discussion

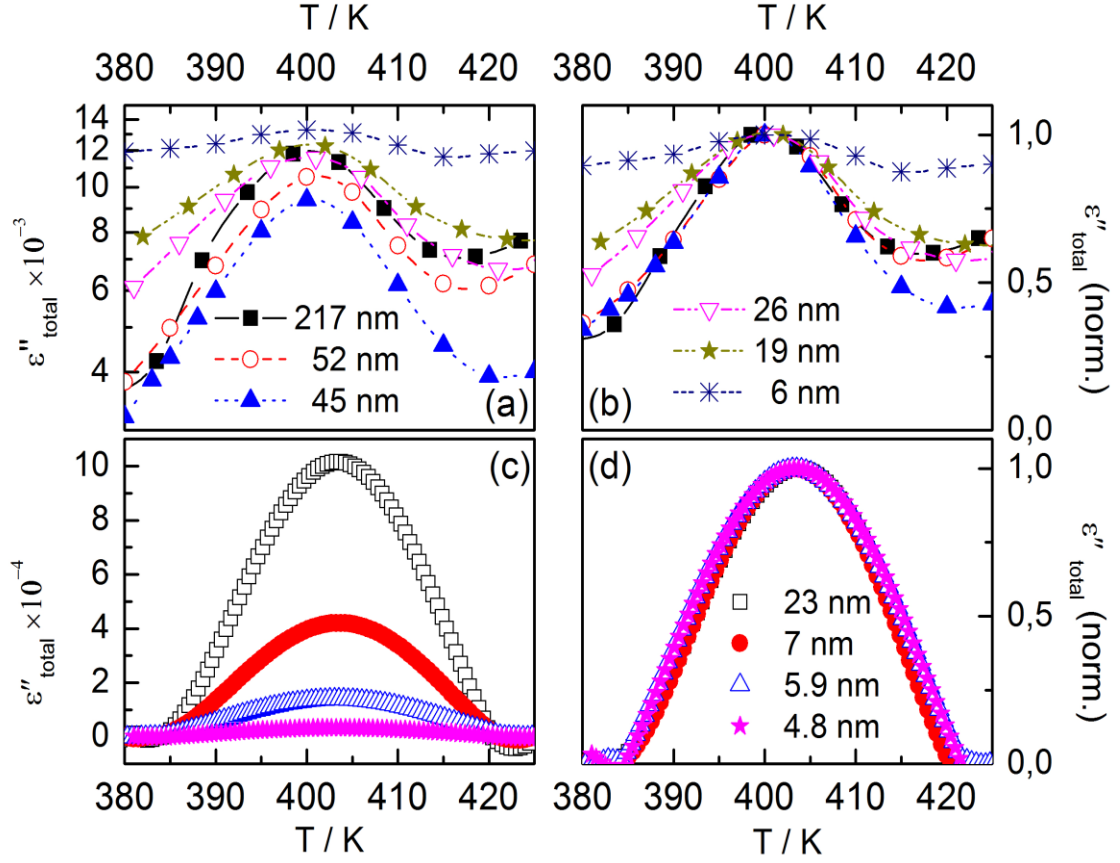


**Figure 4.1.** The dielectric loss,  $\epsilon''_{total}$  of PS-300 layers (with thicknesses as indicated) measured in (a) the conventional geometry that employs evaporated metal electrodes (at 1 kHz), and (c) a nanostructured electrode arrangement (at 0.8 kHz). Panels (b) and (d) display the same curves normalized with respect to the maximum loss values. (a) and (b) share a common legend, as do (c) and (d). Adapted from [69] with permission.

In the frequency and temperature range studied by BDS, polystyrene exhibits a well-resolved ( $\alpha$ -) relaxation process assigned to the fluctuation of its structural units. Figure 4.1 shows the dielectric loss,  $\epsilon''_{total}$ , as measured in both geometries. It is observed – as summarized in Figure 4.2 – that the  $\alpha$ -relaxation remains unchanged in its mean relaxation rate for all studied layer thicknesses. However, the spectra reveal fundamental differences between the two geometries: for the capped arrangement, the measured dielectric response exhibits an increase in its relaxation strength,  $\Delta\epsilon$ , when the layer thickness is decreased

from 45 to 6 nm (Fig. 4.1a). This contrasts sharply with what is observed for the uncapped geometry where the dielectric strength falls with decreasing sample thickness – a phenomenon which is expected because the volume of PS in the capacitor reduces as well. Another difference is clearly portrayed by the normalized plots: while the data obtained using evaporated electrodes undergoes dramatic broadening with reducing layer thickness, that from the nanostructured electrode arrangement remains unchanged. For the latter case, Figure 4.1d actually shows coinciding curves for all investigated thicknesses.

It is therefore important to note that although the same material is studied, differences occur in the measured response in dependence on the measurement geometry employed. This is why it is necessary to treat the measured function as  $\epsilon''_{total}$  since it, no doubt, contains several contributions, all of which are not necessarily related to the polystyrene. For instance, apart from the interfacial layers which may have reduced or broadened dynamics, oxide layers can also cause the broadening of relaxation peak, or, depending on the dielectric strength of the sample under study, even shift the measured mean relaxation time [203].

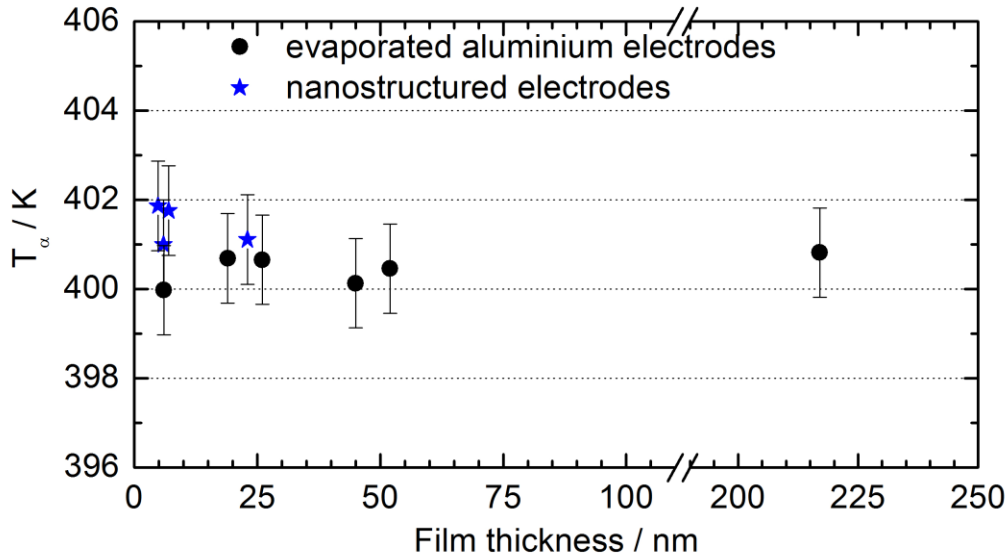


**Figure 4.2.** Thickness-dependence of the dielectrically determined characteristic temperature,  $T_\alpha$ , for the conventional geometry (at 1 kHz) and for the preparation with nanostructured electrodes (at 0.8 kHz). Adapted from [69] with permission.

In order to explain these differences in the measured dielectric response, a layer model [203,204] is employed, taking into account all (major) possible contributions. Figure 4.3 provides a scheme of the layers expected to play a significant role for both geometries; these are, the PS layer (assumed to be all bulk-like), native alumina and the aluminium electrode for the capped geometry, and PS, native silica, silicon and an air gap for the novel approach.

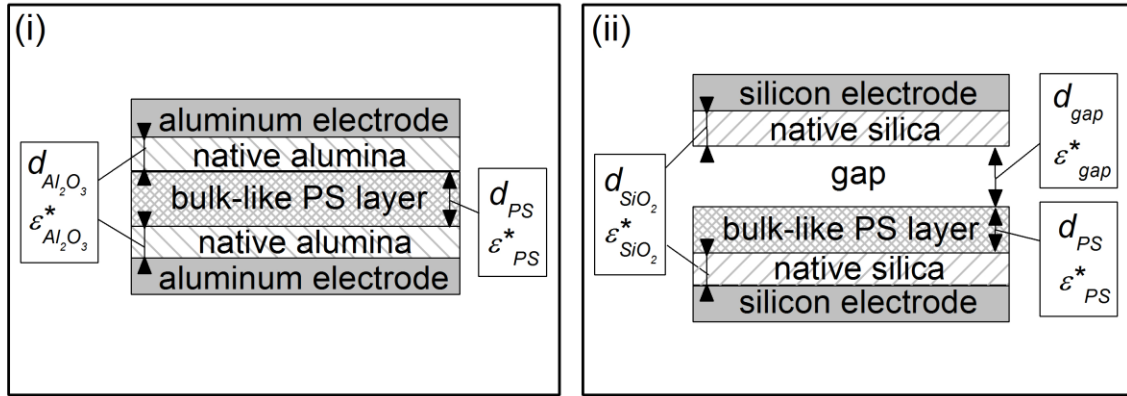


**Figure 4.3.** A scheme of the layered arrangement assumed for modelling the dielectric results in the (i) capped and (ii) uncapped geometries. The specific thickness values of the oxide layers and their respective complex dielectric function ( $\epsilon^* = \epsilon' - i\epsilon''$ ) are specified in the text. Adapted from [69] with permission.

The oxide layers are treated as being dielectrically *dead* in the sense that they do not show relaxation processes, but instead have constant dielectric loss; their contributions are therefore included as additional impedances. The measured dielectric loss for the capped and uncapped arrangements can then be modelled, respectively, as:

$$\epsilon_{total}^* = \frac{D}{\left[ \frac{d_{PS}}{\epsilon_{PS}^*} + \frac{2d_{Al_2O_3}}{\epsilon_{Al_2O_3}^*} \right]} \quad (4.1)$$

$$\epsilon_{total}^* = \frac{D}{\left[ \frac{d_{PS}}{\epsilon_{PS}^*} + \frac{2d_{SiO_2}}{\epsilon_{SiO_2}^*} + \frac{d_{AG}}{\epsilon_{AG}^*} \right]} \quad (4.2)$$

where  $D$ ,  $d_{PS}$ ,  $d_{Al_2O_3}$ ,  $d_{SiO_2}$ , and  $d_{AG}$  are the thickness values for the whole capacitor, the polystyrene (PS) layer, the aluminium oxide, silicon oxide and the air gap (AG), respectively. Their respective complex dielectric permittivities are given by  $\epsilon_{PS}^*$ ,  $\epsilon_{Al_2O_3}^*$ ,  $\epsilon_{SiO_2}^*$  and  $\epsilon_{AG}^*$ . A bulk-like dielectric function of the PS layers is modelled using the Havriliak-Negami equation (Eq. 3.39) with parameters:  $\epsilon_\infty = 2.5$ ,  $\Delta\epsilon = 0.04$ ,  $\alpha = 0.72$  and  $\beta = 0.46$ .

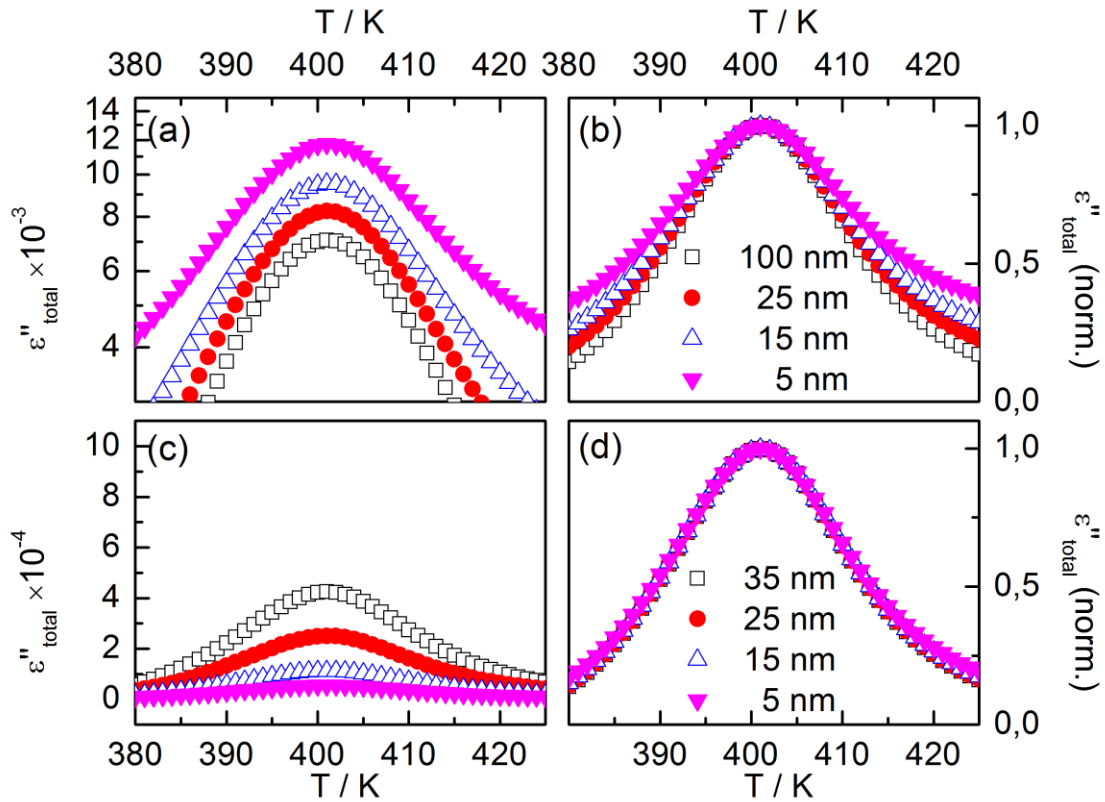


**Figure 4.4.** Calculated dielectric loss  $\epsilon''_{total}$  (PS thicknesses indicated) at a frequency of 1 kHz considering sample geometries of (a) conventionally evaporated and (c) nanostructured electrodes. For both cases, a PS layer having bulk-like dynamics is assumed, together with oxide layers with properties as specified in the discussion. (b) and (d) display normalized plots of the data in (a) and (c), respectively. Adapted from [69] with permission.

Concerning the oxide layers, to the best of our knowledge only the properties of the bulk materials are known. Furthermore, in the case of alumina, the dielectric properties are sen-

sitive to the type and amount of impurities; even small amounts of different elements can have a strong impact on the dielectric spectra [205]. Thus, the total dielectric functions  $\epsilon''_{total}$  for both geometries, and different polymer layer thicknesses, were calculated assuming appropriate bulk values for the real and imaginary parts (alumina:  $\epsilon'_{Al_2O_3} = 9.6$ ,  $\epsilon''_{Al_2O_3} = 0.03$  [205] with a thickness of 3 nm [206] at each interface in the case of evaporated electrodes; silica:  $\epsilon'_{SiO_2} = 4$ ,  $\epsilon''_{SiO_2} = 10^{-3}$  of a thickness of 2 nm [207] at each interface in the case of silicon wafers). The quoted values for SiO<sub>2</sub> were obtained from dielectric measurement of an evaporated 200-nm thick silica film. Figure 4.4 shows that this leads to qualitative agreement with the measured data since all features observed in Figure 4.1 are recovered. In an attempt to improve the model presented in Figure 4.3, note is taken of the fact that some studies (e.g. [143]) have shown evidence of immobilized polymer layers at the solid-polymer interface(s). Figure 4.5 demonstrates – assuming a 0.5 nm-thick immobilized PS layer (with  $\epsilon' = 2.5$  and  $\epsilon'' = 10^{-5}$ ) at the interfaces – that indeed the calculation yields better results, although quantitative agreement is still not achieved.

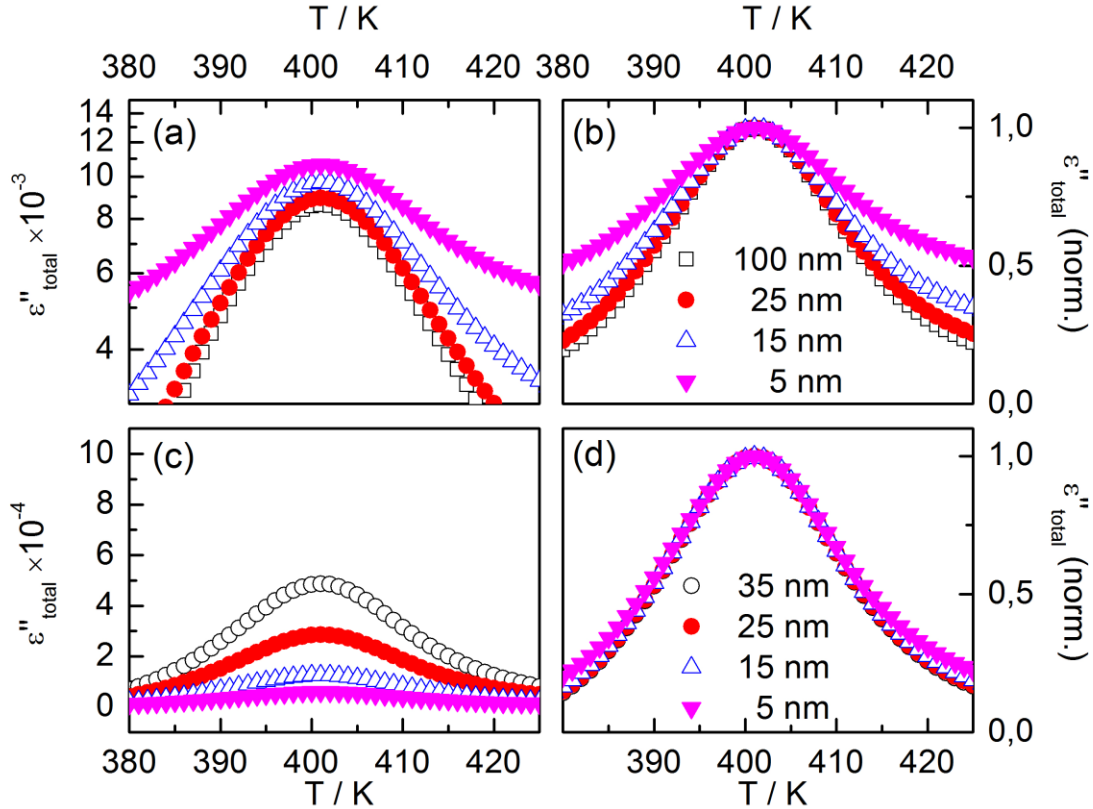


**Figure 4.5.** Calculated dielectric loss  $\epsilon''_{total}$  (PS thicknesses indicated) at a frequency of 1 kHz considering metal oxide as well as immobilized polymer layers at the interfaces for the (a) capped and (c) uncapped geometries. Panels (b) and (d), respectively show normalized plots of the data in (a) and (c).

The following reasons are advanced to explain why a quantitative replication of the measured data is not realized: (i) The fact that, apart from the oxide and immobilized layers, one too has to consider that some polymer segments at the interface have slowed down dynamics (compared to the bulk material) [147], and that this slow-down may have its own distribution. Krutyeva *et al.* [208] suggest the existence of the so-called interphase – a region comprising chains which, although not in direct contact with the surface, are confined by virtue of their interaction with those immediately on the interface. (ii) For the nanostructured electrode arrangement, one interface is free. At such an interface, the works of Paeng *et al.* [106,107] find evidence of a surface layer with faster dynamics. Additionally, (iii) for this geometry, inaccuracies in the macroscopic (at extensions of  $\sim 4$  nm) evenness are present, implying a reduction in the precision with which the exact geometry is known.

#### 4.1.4 Summary

Two geometries applied – for Broadband Dielectric Spectroscopy – to study molecular dynamics in confinement have been substantively investigated. It is shown that the traditional approach where metal electrodes are evaporated, introduces an artificial broadening to the measured relaxation peaks. This view springs from the fact that the inclusion of metal oxide and immobilized polymer layers in the calculation model reproduces – albeit qualitatively – the measured dielectric response for both geometries. It follows therefore that there's an additional significant contribution for the case of evaporated electrodes which is not taken care of in the modeling. While the determination of the exact cause of the broadening of the dielectric peaks requires further experimentation, it is clear that the analysis of data obtained using evaporated electrodes must always be done with care, especially when the dielectric strength has to be determined. The mean relaxation times obtained, however, are not affected and are therefore reliable.



## 4.2 Molecular dynamics of polystyrene in a wide range of molecular weights

### 4.2.1 Introduction

Polystyrene (PS) – due to its abundant availability and the fact that it has no propensity to crystallize – is the most studied polymer system in the field of dynamics in confinement. In order to provide answers to some of the questions that still remain open in this field, it is therefore important to investigate the same system further, because clear comparisons can be made with already reported data in literature. Three fundamental questions form the basis of the work reported in this Section: 1) How do dynamics in confinement depend on the size (molecular weight) of the molecules involved? 2) Do different experimental techniques deliver coinciding results? 3) What could be the possible reasons for the disparities in the reported results on polystyrene? Broadband Dielectric Spectroscopy (BDS) is therefore combined with spectroscopic vis-ellipsometry (SE)<sup>3</sup> to study the glassy dynamics of confined PS in the molecular weight range  $27\,000 < M_w < 10\,000\,000$  g/mol. In addition, complementary experiments employing X-ray reflectometry (XRR), AC calorimetry (ACC) and Differential Scanning Calorimetry (DSC) are reported.

### 4.2.2 Experimental details

Six different samples of atactic polystyrene (purchased from Polymer Standards Service GmbH) with varying molecular weights and polydispersity indices (Table 4.1) were studied by BDS and SE. Highly polished (monocrystal 100) silicon wafers (purchased from microFab and [www.University-Wafer.com](http://www.University-Wafer.com) for BDS and SE, respectively) with a native oxide layer of about 2 nm were used as substrates for film preparation. Glass (microscope) slides (Carl Roth GmbH & Co. KG) were also used as substrates in some of the BDS measurements. Toluene (99.9% pure) and acetone (99.8% pure) were used as solvents for film preparation and cleaning purposes, respectively, and were obtained from Sigma-

---

<sup>3</sup> SE and XRR measurements were carried out at the Leibniz Institute for Polymer Research (IPF), Dresden, Germany by Michael Erber and Jan Müller, respectively, in a joint research project between the Groups of Professors B. Voit (IPF) and F. Kremer (Universität Leipzig).

Aldrich GmbH. Except for filtering (Millex syringe filters, PTFE membrane with 0.2  $\mu\text{m}$  pore size) of the solutions before spin-casting, the polymer materials and solvents were used as received without further purification.

**Table 4.1.** Characteristics of PS samples studied in this work

Sample	M <sub>w</sub> (kg/mol)	M <sub>w</sub> /M <sub>n</sub>	R <sub>g</sub> (nm) <sup>a</sup>
PS-30	27.5	1.03	4.6
PS-60	58.9	1.01	6.7
PS-300	319	1.05	15.7
PS-700	749	1.10	24.0
PS-1 000	1 103	1.14	29.1
PS-10 000	8 090	1.17	78.8

<sup>a</sup>Radii of gyration in  $\Theta$  solvent were calculated according to [209].

Regarding BDS measurements, the two sample geometries discussed in Section 4.1 were used. In both cases, the films were always annealed at 430 K (i.e.,  $T_g + 50$  K) for at least 24 h in oil-free high vacuum ( $10^{-6}$  mbar) before dielectric measurements. For ellipsometric measurements, an alkaline cleaning procedure was used for purifying the silicon substrate surfaces. First, the wafers were cleaned in an ultrasonic bath of  $\text{CH}_2\text{Cl}_2$  at room temperature for 15 min. Then, they were transferred to an alkaline hydroperoxide solution consisting of Millipore water, resistivity  $\geq 18$  M $\Omega$  cm,  $\text{H}_2\text{O}_2$  (30%) and  $\text{NH}_3$  (25%) in the ratio 20:1:0.2 for 20 min at 354 K. Thereafter, the wafers were carefully rinsed by Millipore water, dried by argon flow, and directly used. The layers (for both BDS and SE studies) were deposited by spin-casting at 3000 rpm for 20 s and their thicknesses adjusted by varying the toluene-polystyrene concentration. Thickness determination was achieved by means of atomic force microscopy (AFM) and found to be within a variability of  $\pm 10\%$  for layers down to  $\sim 20$  nm and up to  $\pm 20\%$  for thinner samples.

Dielectric measurements were carried out using an Andeen-Hagerling impedance bridge; a Quatro temperature controller (Novocontrol Technologies) was used for temperature regulation. Measurements were made in the frequency range 50 Hz-20 kHz at temperatures between 380 and 430 K. During measurement, samples were always kept in a pure nitrogen atmosphere. In a temperature representation of the dielectric spectra, the  $\alpha$ -relaxation peak

for polystyrene is clearly seen in the temperature window mentioned above. Therefore, one is able to obtain the characteristic (maximum loss) temperature,  $T_\alpha$ , at a chosen frequency, which effectively corresponds to the relaxation rate at this temperature.

For spectroscopic vis-Ellipsometry, temperature dependent measurements were carried out at a fixed angle of incidence of  $70^\circ$  using a Multi Wavelength (370 –1680 nm) Rotating Compensator Ellipsometer (RCE) M2000VI (J. A. Woollam Co., Inc., USA) connected to a heat-cell (INSTECH Inc., USA). Both annealing (425K for at least 24 h) and measurement were performed under dry argon flow (Alphagaz<sup>TM</sup>1, purity 99.999 %) and the latter done at a rate of 2 K/min without exposing the sample to ambient air. For this technique, the polystyrene layers were prepared on ultra-flat silicon wafers similar to those ones used in the BDS measurements. The layer thickness  $d$  and the refractive index  $n$  were fitted to the ellipsometric angles  $\Psi$  and  $\Delta$  in the entire wavelength range assuming an appropriate layer stack (Si/SiO<sub>2</sub>/Cauchy/ambient) as optical model. A Cauchy dispersion ( $k = 0$ ) for the wavelength dependence of the polymer refractive index is assumed. The temperature position of the discontinuity (“kink”) in either  $d$  or  $n$  is known to be the (ellipsometrically determined) glass transition temperature  $T_g$ . However, in this study the second derivatives of interpolated curves of  $d(T)$  and  $n(T)$  (interpolation was done by applying a 9<sup>th</sup> order polynomial fit) were used to determine  $T_g$  because a higher accuracy is thereby attained [210] although this interpolation introduces an error of  $\pm 2$  K.

### 4.2.3 Results and discussion

Figure 4.6 shows the thickness-dependence of the dynamic glass transition for polystyrene layers prepared from different molecular weights in the capped geometry: PS-60, PS-300, and PS-1000 all measured at 1 kHz, and PS-700 (at 0.5 kHz). Similar data is presented for the uncapped geometry in Figure 4.7: PS-1 000 (at 0.24 kHz) and PS-10000 (at 1 kHz). Down to a thickness of 29 nm (PS-60), 6 nm (PS-300), 17 nm (PS-700), 11 nm (PS-1 000) and 9 nm (PS-10 000), no shifts in the dynamics glass transition are observed, as compared to bulk. As already shown in Section 4.1 (see Fig.4.1), the same observation is made for a polystyrene layer as thin as 4.8 nm ( $\sim 0.3R_g$ ). The high temperature wings (Fig. 4.6) are

conductivity contributions, while the apparent broadening of the loss peaks is mainly attributed to the presence of oxide and immobilized layers at the interface.

Ellipsometric measurements on PS for different molecular weights show clear discontinuities in the determined temperature dependences of the layer thickness (Fig. 4.8a,b) due to the transition from the glassy to rubberlike state. Within error margins, no thickness dependence of the (ellipsometrically determined)  $T_g$  is exhibited by PS layers down to  $\sim 20$  nm for all the investigated molecular weights. Furthermore, X-ray reflectometry (XRR) was applied to measure thin layers (20-88 nm) of PS-300. In all investigated samples, the temperature dependence of the recorded layer thickness shows a distinct discontinuity indicating the glass transition temperature (see Fig. 4.8c). The measurements reveal no thickness dependence of the  $T_g$  within error margins of  $\pm 3$  K and coincide with the ellipsometrically determined  $T_g$  values as displayed in panel c of Figure 4.10.

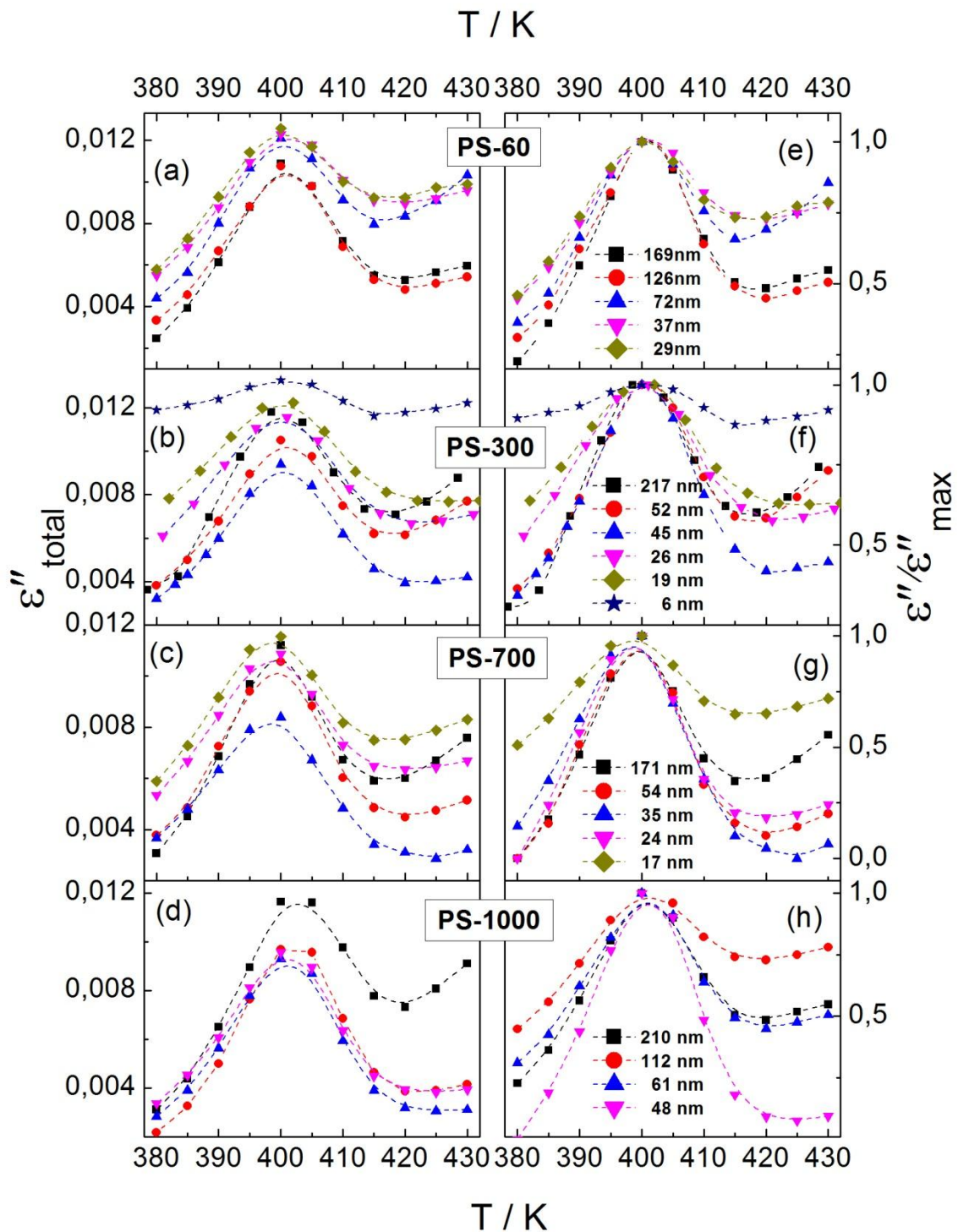


**Figure 4.6.** Temperature dependence of the dielectric loss  $\epsilon''_{total}$  for capped samples prepared from four different molecular weights of PS (as indicated) with varying layer thickness (also shown) as measured at 1 kHz (for PS-60, PS-300 and PS-1 000) and 0.5 kHz (PS-700). The graphs in (e)-(h) are normalized w.r.t. the maximum loss value in the corresponding raw data (a)-(d).

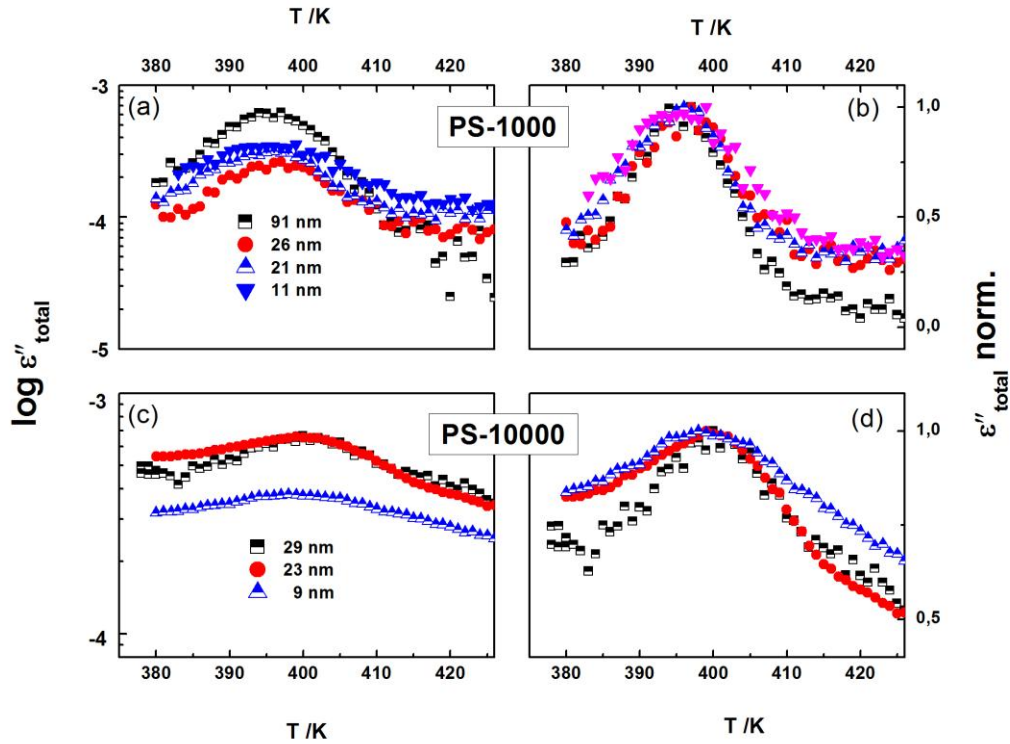


**Figure 4.7.** Temperature dependence of the dielectric loss  $\varepsilon''_{total}$  for uncapped samples prepared from two molecular weights (indicated) with reducing layer thickness (also shown) as measured at 0.24 kHz (for PS-1 000 (a)) and 1 kHz (PS-10 000 (c)). (b) and (d) are the corresponding normalized (w.r.t. the maximum loss) plots. Adapted from [70] with permission.

Figure 4.9 presents the relaxation map as obtained from the results of several experimental techniques. Here, the mean relaxation rate is plotted against inverse temperature for a selected set of the investigated samples. It is evident that – over a range of more than 2 decades of relaxation rate – both sample geometries employed in the BDS experiments deliver coinciding results which are in full accord with AC calorimetric measurements. No deviation from bulk-like glassy dynamics in PS layers down to 5 nm is revealed in these measurements. Further, ellipsometry and X-ray reflectometry deliver coinciding  $T_g$  values which are in good agreement with the DSC measurements and the dielectrically-determined  $T_g$  (obtained by extrapolating VFT fits to the BDS data to a time of 100 s).

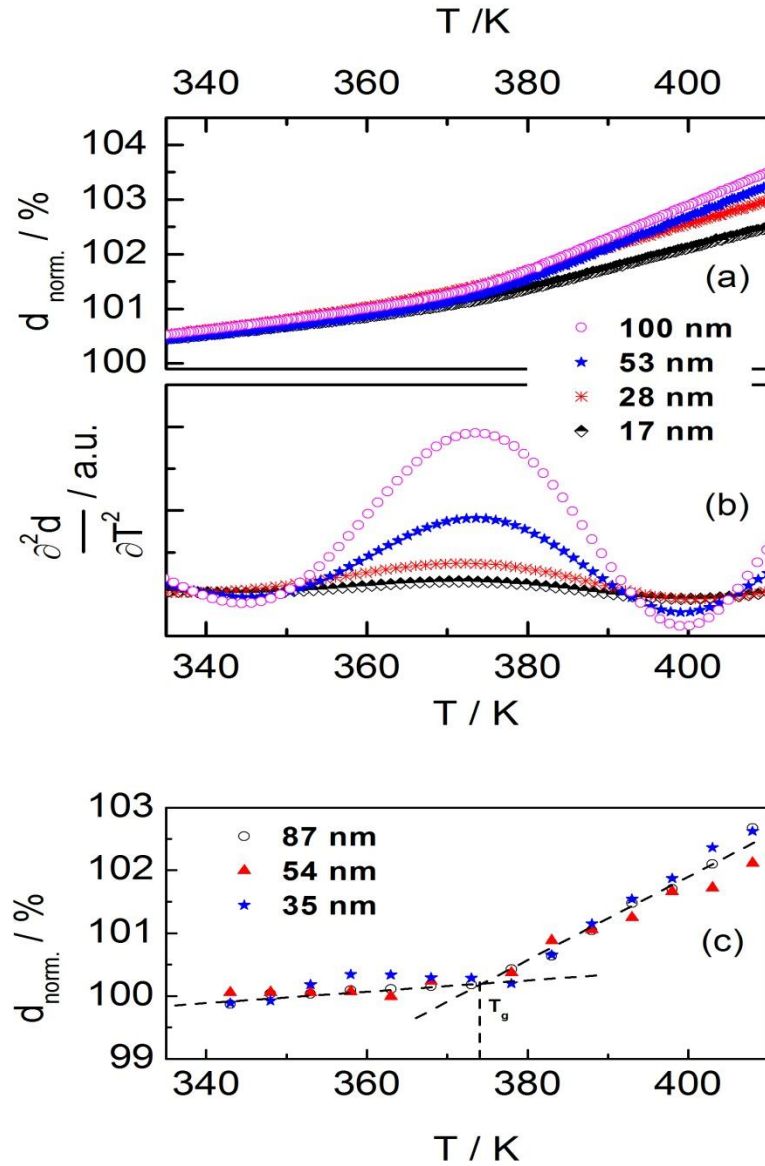


**Figure 4.8.** The ellipsometrically determined temperature dependence of the layer thickness of PS films (initial thicknesses as indicated) normalized w.r.t. the layer thickness at 300 K (a). The second derivative of each curve was used for determination of the kink position (b). Panel (c) shows the temperature dependence of normalized thickness  $d_{norm.}$  of PS-300 layers (with indicated thicknesses) as measured by XRR. The dashed lines are linear fits to the data in the glassy and rubbery state for the 35 nm thin sample. Their intersection point is the glass transition temperature,  $T_g$ . Adapted from [69,70] with permission.

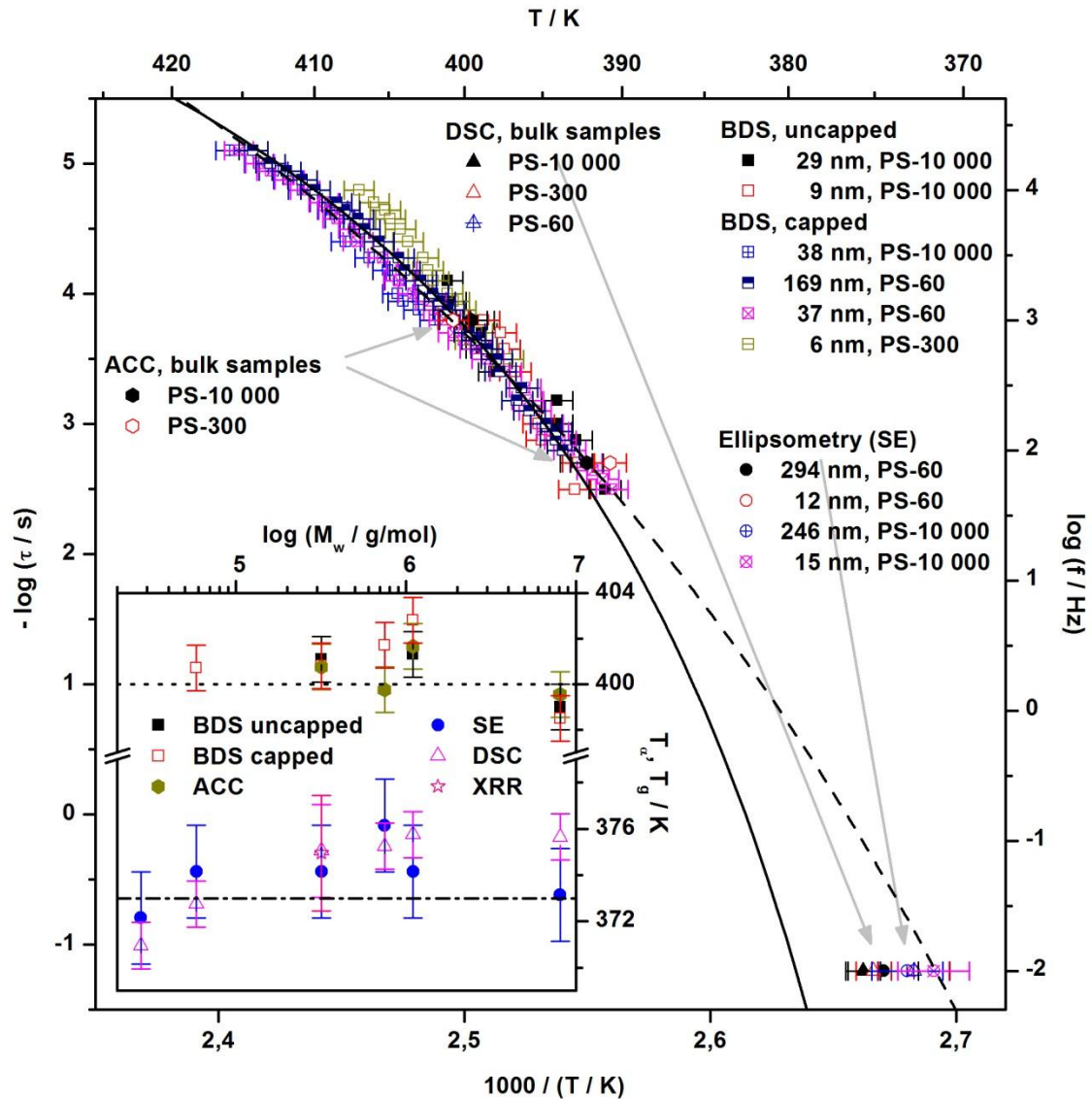


**Figure 4.9.** The activation map showing the mean relaxation times (as functions of inverse temperature) of a selected set of measurements as determined by various experimental techniques for different layer thicknesses, as indicated. Within the error margins, the measurements carried out by BDS (in capped and uncapped geometries) (squares), AC calorimetry (hexagons), and DSC (triangles) coincide. Additionally, VFT fits to the data for two PS-60 samples having thicknesses of 169 nm (solid line) and 37 nm (dashed line) are plotted. The inset displays the  $M_w$ -dependence of  $T_\alpha$  as measured at 1 kHz by BDS and AC calorimetry as well  $T_g$  as determined SE, XRR, and DSC for bulk-like samples. The dotted and dash-dotted lines at 400 and 373 K, respectively, serve only as guides to the eye. Adapted from [70] with permission.



In the inset of Figure 4.9,  $T_\alpha$  (obtained at 1 kHz) and  $T_g$  values of bulk-like samples as determined by the various experimental techniques are plotted as functions of molecular weight. Once again, the coincidence of BDS and ACC measurements, and an invariance of the characteristic temperatures with molecular weight are revealed. Similarly, the  $T_g$  values of the bulk as measured by ellipsometry, X-ray reflectometry, and DSC are in agreement, although the DSC results exhibit a  $T_g$  reduction (of  $\sim 5$  K) with decreasing molecular weight.

Figure 4.10 summarizes the experimental results for all the six molecular weights investigated in this work. Here, the thickness dependencies for the temperature position of the  $\alpha$ -relaxation peak  $T_\alpha$  (as measured by BDS at specified frequencies) and for  $T_g$  (as measured by SE) are shown. It is clear that changes in the dielectrically determined  $T_\alpha$  and ellipsometrically determined  $T_g$  mostly lie within the error margins of  $\pm 1$  and  $\pm 2$  K, respectively, and never exceed  $\pm 3$  K from the thickest (bulk-like) sample. However, it is noteworthy that in four of the six investigated molecular weights (PS-60, PS-700, PS-1 000, and PS-10 000), there are indications of thickness-dependent  $T_g$  values, though all lie within the error margins; as the layer thickness is reduced, the  $T_g$  tends to decrease (not randomly scattered around the bulk value). This trend, however, is not observed in an intermediate molecular weight of 319 000 g/mol (PS-300) therefore forestalling a generalized conclusion. In summary, it is proven – for a wide range of molecular weights of polystyrene – that down to layer thicknesses of  $\sim 5$  nm, alterations in the glassy dynamics do not exceed  $\pm 3$  K.

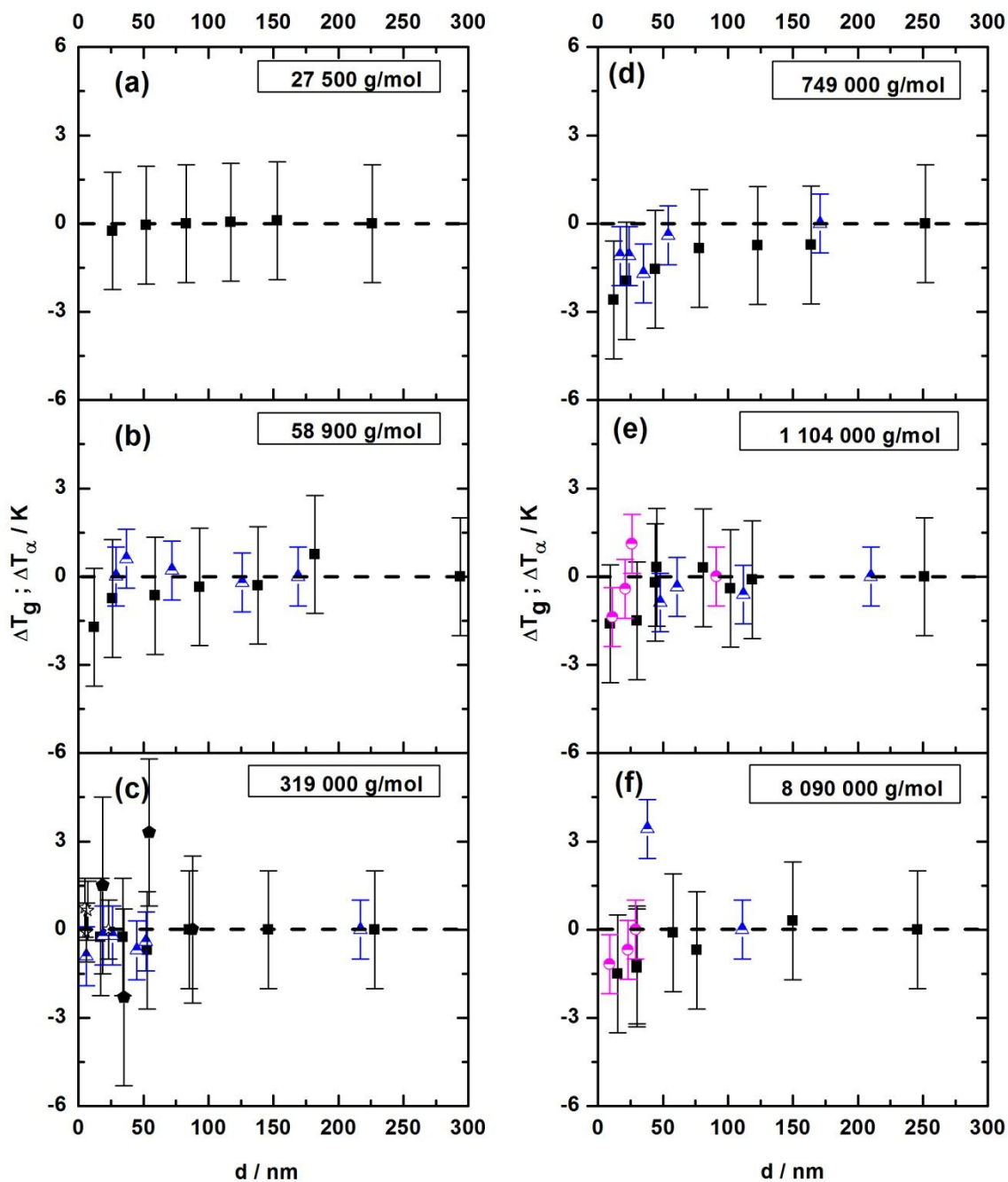


**Figure 4.10.** Deviations (from the value of the thickest sample) of the characteristic temperature  $T_\alpha$  (BDS as measured at 1 kHz) or  $T_g$  (SE, ACC, DSC) in dependence on layer thickness for various molecular weights of polystyrene. Half-filled triangles, and half-filled circles represent data obtained from capped and uncapped samples, respectively; solid squares are  $T_g$  data from SE; the stars in (c) represent complementary data obtained by XRR. Error margins as big as  $\pm 1$  K for BDS,  $\pm 2$  K for SE, and  $\pm 2.5$  K to  $\pm 3$  K for XRR are indicated.

These results compare well with some in literature [e.g., 21–26], but also differ sharply with others [e.g., 1,27–31]; in the latter case, thickness and  $M_w$ -dependent shifts in the glass transition temperature are reported. Since exactly the same polymer system is studied, one must raise the question: what is the reason for this discrepancy? It is now well known that the segmental dynamics of a polymer and hence the dynamic and calorimetric glass transition are influenced by a variety of factors: (i) remaining solvent acting as plasticizer in the polymer causes a pronounced increase in the segmental mobility [214] (ii) physical aging [131,133] and (iii) chemical degradation [131] shift as well the dynamic glass transition. Evidently these factors play an especially important role in nanometric thin polymer layers as demonstrated in detail by Serghei and Kremer [138]. Perlich *et al.* [164] studied the solvent content in thin spin-coated PS homopolymer layers by neutron reflectometry and found – in freshly prepared samples before annealing – a pronounced thickness and molecular weight dependence. They showed that annealing for 8 h in vacuum ( $10^{-2}$  mbar) at  $T_g + 20$  K reduced the solvent content by only 1.0 vol % while a 3.2 vol % effect is registered for annealing at  $T_g + 60$  K. Furthermore, an enrichment of solvent at the polymer/substrate interface was revealed. In view of these multiple parameters influencing the dynamic glass transition, it is expected that details of the sample preparation play a significant role in the reported disparities.

#### 4.2.4 Summary

Thin layers of polystyrene (in a wide molecular weight range of  $27\,000 < M_w < 10\,000\,000$  g/mol) have been investigated using a multi-technique approach. It has been shown that the glassy dynamics and glass transition temperature remain within a margin of  $\pm 3$  K of the bulk value even when the system is confined to a layer thickness as small as  $\sim 0.3R_g$ . Where comparison of results is possible, it is proven that BDS, SE and XRR deliver results which are in quantitative agreement. Furthermore, no dependence on molecular weight is established. It is argued here that preparative details account for the diversity in the results reported on PS in the literature. An overview is presented in Chapter 5.

## 4.3 Molecular dynamics of itraconazole confined in thin supported layers

### 4.3.1 Introduction

Thermotropic liquid crystals (LC) are a class of matter with properties intermediate between those of the crystalline and isotropic liquid state. Liquids have maximal mobility and minimal (positional and translational) order while the reverse is true for crystals. In LCs, aspects of both states co-exist, and mesomorphic phases develop with a competing interplay between order and mobility. The most significant liquid crystalline structures are the smectic and nematic mesophases, the latter being the mesophase with the least order. In the nematic regime, molecules have all translational degrees of freedom and hence no long range positional order. Their long axes are favorably aligned with respect to a common unit vector  $\mathbf{n}$ , the so-called nematic director. The degree of orientation [215] of the molecules is described by an order parameter  $S$ , given by  $S = \langle 3\cos\theta - 1 \rangle / 2$ , where  $\theta$  is the angle between the director  $\mathbf{n}$  and the direction of the long axis of the molecule; the brackets denote statistical averaging. It is easy to see that for a fully aligned LC phase,  $S = 1$ . The aspect of mobility presents the opportunity to modify the orientations of the molecules by use of external electric (or magnetic) fields. Consequently, broadband dielectric spectroscopy is a versatile tool to study LCs. Liquid crystalline properties arise due to the anisotropy in the shape of the molecules; most of them have a rod-like unit in their structure, although bent-shaped and disc-like units in molecules are also known to give rise to liquid crystalline properties [216]. Since LCs are anisotropic systems, their dielectric properties are anisotropic as well, and the complex dielectric function  $\varepsilon^*(\omega)$  – where  $\omega$  is the angular frequency – is given by a tensor. This tensor, in the case of uniaxial nematic phases, has two components  $\varepsilon_{\parallel}^*$  and  $\varepsilon_{\perp}^*$  parallel and normal, respectively, to the nematic director. For a detailed discussion of the theory of dielectric relaxations in LCs, the reader is referred to other publications [12,217–219]. Briefly described, the starting point is the fact that the molecular dipole moment vector of a mesogenic unit has two components, one oriented longitudinal and the other transverse to its long axis. The dielectric response arises from

correlation functions of the polarization fluctuations parallel and normal to the nematic director. In this semi-microscopic framework, the measured dielectric function parallel  $\varepsilon_{\parallel}^*(\omega)$  and normal  $\varepsilon_{\perp}^*(\omega)$  to the director has different weighted sums of four underlying relaxation modes depending on the macroscopic orientation of the sample. The relaxation mode with the lowest frequency is due to rotational fluctuations of the molecule around its short axis, and it determines  $\varepsilon_{\parallel}^*(\omega)$ . This process is called the  $\delta$ -relaxation [220–224]. The remaining three relaxations – different tumbling fluctuations of the molecules about their long axis – have nearly the same relaxation rate and may form one broad relaxation process, which is related to  $\varepsilon_{\perp}^*(\omega)$ . This tumbling mode is located at higher frequencies than the  $\delta$  process. While there has been controversy concerning which of these two processes is responsible for glassy dynamics in glass-forming LCs, recent experiments [222,225] have helped identify the tumbling mode as being the underlying process. A comparison between BDS data in the present work and temperature modulated DSC data published elsewhere [226] (see activation plots) confirms this finding for itraconazole. Therefore the latter process can simply be referred to as the  $\alpha$ -process, akin to the structural relaxation process in conventional glass formers.

Itraconazole, the triazole derivative studied in this work, is an active pharmaceutical ingredient (API) with rod-like structure and is known to have antifungal activity [227]. Apart from the structural ( $\alpha$ -) relaxation process, the bulk system exhibits a  $\delta$ -process (at lower frequencies in the supercooled liquid) which is attributed to the flip-flop fluctuation of the molecule about its short axis [226]. Additionally, although a first glance at the molecule (Fig. 4.11a) does not reveal its liquid crystalline-like nature (absence of tail ends), DSC scans find two endothermic peaks that are recognizable as being connected to the formation of nematic and Smectic A phases [226,228,229]. The temperatures at which these transitions occur are shifted to the lower side in confinement (Fig. 4.11b,c), a phenomenon that is well-established for confined LCs, at least as studied in nanopores [223,230–234]. In this study, the dynamics of itraconazole confined systematically in supported layers are followed down to a thickness of 6 nm.

### 4.3.2 Experimental details

The sample material – Itraconazole (IUPAC Name: (2R,4S)-rel-1-(butan-2-yl)-4-{4-[4-(4-[(2R,4S)-2-(2,4-dichlorophenyl)-2-(1H-1,2,4-triazol-1-ylmethyl)-1,3-dioxolan-4-yl]methoxy}phenyl)piperazin-1-yl]phenyl}-4,5-dihydro-1H-1,2,4-triazol-5-one), molecular formula:  $C_{35}H_{38}Cl_2N_8O_4$ ,  $M_w = 705.64$  g/mol) was supplied by Sigma Aldrich with purity greater than 99%, and used without further purification. The starting material was completely crystalline with a melting point of 439 K, which agrees with what is reported in the literature (438-451 K) [228]. Its chemical structure is displayed in Figure 4.11a.

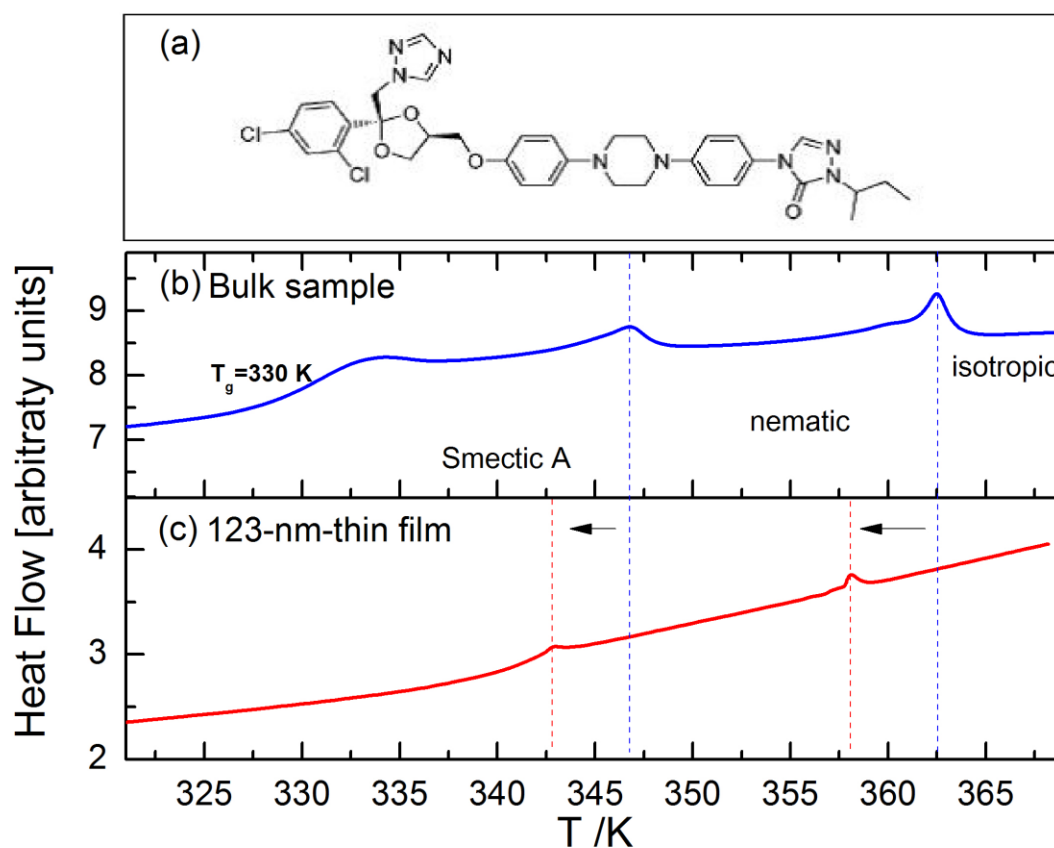


**Figure 4.11.** The chemical structure of the itraconazole molecule showing its rod-like nature (a). DSC thermograms obtained upon heating of (b) the bulk material, and (c) a 123-nm-thick film over a wide temperature range covering the smectic A, nematic and isotropic regions. Two endothermic transitions associated with liquid crystalline ordering are observed in both cases, but are shifted by  $\sim 5$  K to lower temperatures in the thin film sample. Adapted from [235] with permission.

Thin films of itraconazole were prepared by spin-coating from an acetone (Sigma-Aldrich, purity  $\geq 99.9\%$ ) solution at a rate of 3000 rpm. Different thicknesses were obtained by varying the concentration of the mother solution: concentrations of 25, 15, 8, 5 and 1 mg/ml delivered films with thicknesses 123, 83, 46, 22 and 6 nm, respectively. These thicknesses were determined – with uncertainty of  $\pm 2$  nm – by analyzing (Atomic Force Microscopy) AFM-generated height profiles of scratches made on the films. All solutions were filtered through polytetrafluoroethylene (PTFE) membranes (Merck Millipore) having pores of diameter 200 nm. The films – supported on highly conductive silicon wafers (root-mean-square roughness 0.23 nm measured on a  $1 \mu\text{m}^2$  scan area, specific resistivity  $< 3 \text{ m}\Omega\text{cm}$ ) with a 30-nm thermally oxidized layer – were then annealed at 380 K for 24 h in an oil-free high vacuum ( $10^{-6}$  mbar) before dielectric measurements. Nanostructured electrodes (see Section 3.2) were used to assemble the capacitors for dielectric measurements. Isobaric measurements of the dielectric permittivity  $\varepsilon^*(\omega) = \varepsilon'(\omega) - i\varepsilon''(\omega)$  at ambient pressure were performed using a high-resolution Alpha Analyzer (Novocontrol) over a frequency range from 1 to  $3 \cdot 10^6$  Hz. The measured function is denoted in all presentations as  $\varepsilon''_{total}$ , since it is the total response of the whole active capacitor. It has already been demonstrated that  $\varepsilon''_{total}$  still retains the shape and mean relaxation rate of the material under investigation [203], although the absolute dielectric strength (of the sample) cannot be determined, at least up to now, for this specific sample geometry. Temperature control was executed by a Quattro System (Novocontrol) using a jet of dry nitrogen, thereby ensuring relative and absolute errors better than 0.1 and 2 K, respectively. The dielectric measurements were performed in the temperature range 330 - 386 K after first quenching the samples to the glassy state.

### 4.3.3 Results and discussion

To analyze the isothermal spectra of the dielectric loss, two Havriliak-Negami (HN) functions [195] were used:

$$\varepsilon''(\omega) = \frac{\sigma_{dc}}{\varepsilon_0 \omega} + \text{Im} \sum_{j=1}^2 \left\{ \varepsilon_{\infty} + \frac{\Delta \varepsilon_j}{[1 + (i\omega\tau_j)^{\alpha_j}]^{\beta_j}} \right\} \quad (4.3)$$

where the first term accounts for the conductivity contribution,  $\varepsilon_{\infty}$  is the permittivity of the unrelaxed medium,  $\alpha$  and  $\beta$  are the shape parameters representing the symmetric and asymmetric broadening of the given relaxation peaks,  $\Delta\varepsilon$  the dielectric strength,  $\tau$  the relaxation time, while  $\omega = 2\pi f$  is the angular frequency of the applied field.

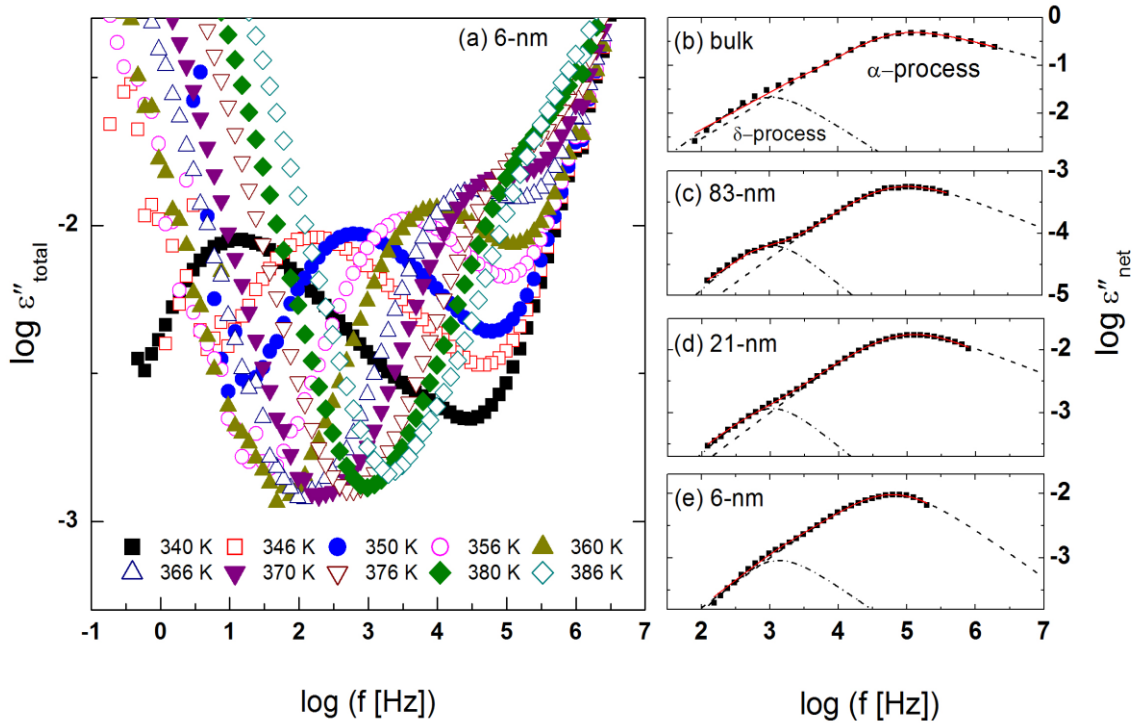


**Figure 4.12.** Raw dielectric spectra: the imaginary part of the measured permittivity,  $\varepsilon''_{total}$ , as a function of frequency for a 6-nm thin itraconazole layer (a). Panels (b), (c), (d) and (e) show the dielectric spectra (at 375 K [bulk] and 374 K [thin films]) after subtraction of the conductivity contribution and the high-frequency wing; the dashed and dash-dotted lines, respectively, are HN-functions describing the  $\alpha$ - and  $\delta$ -relaxation processes. Adopted from [235] with permission.



The measured dielectric response of the thin films in our set up includes some spurious conductivity and resistance of the silicon electrodes which cause an increase in the dielectric loss in the low and high frequency flanks, respectively. Figure 4.12a is representative data for a 6-nm thin layer, and shows the molecular processes together with the extra contributions on the low and high frequency sides. These spectra show the structural ( $\alpha$ -) relaxation process (due to precessing motions of the molecules), which underlies the dynamic glass transition, and a shoulder between the  $\alpha$ -process, and the conductivity contribution. This is a  $\delta$ -relaxation process – whose genesis is the flip-flop fluctuation of the itraconazole molecule about its short axis – clearly resolved after subtraction of the dc conductivity (see Fig. 4.12b-e). In Figure 4.13, all the dielectric loss spectra (after subtraction of both the conductivity contribution and the high-frequency wing) for bulk itraconazole (panel a) and films of various thickness, i.e., 123, 83, 46, 21 and 6 nm (panels b to f) are presented. As evident from Figures 4.12 and 4.13, the two relaxation processes are present in both the bulk material and the thin layers.

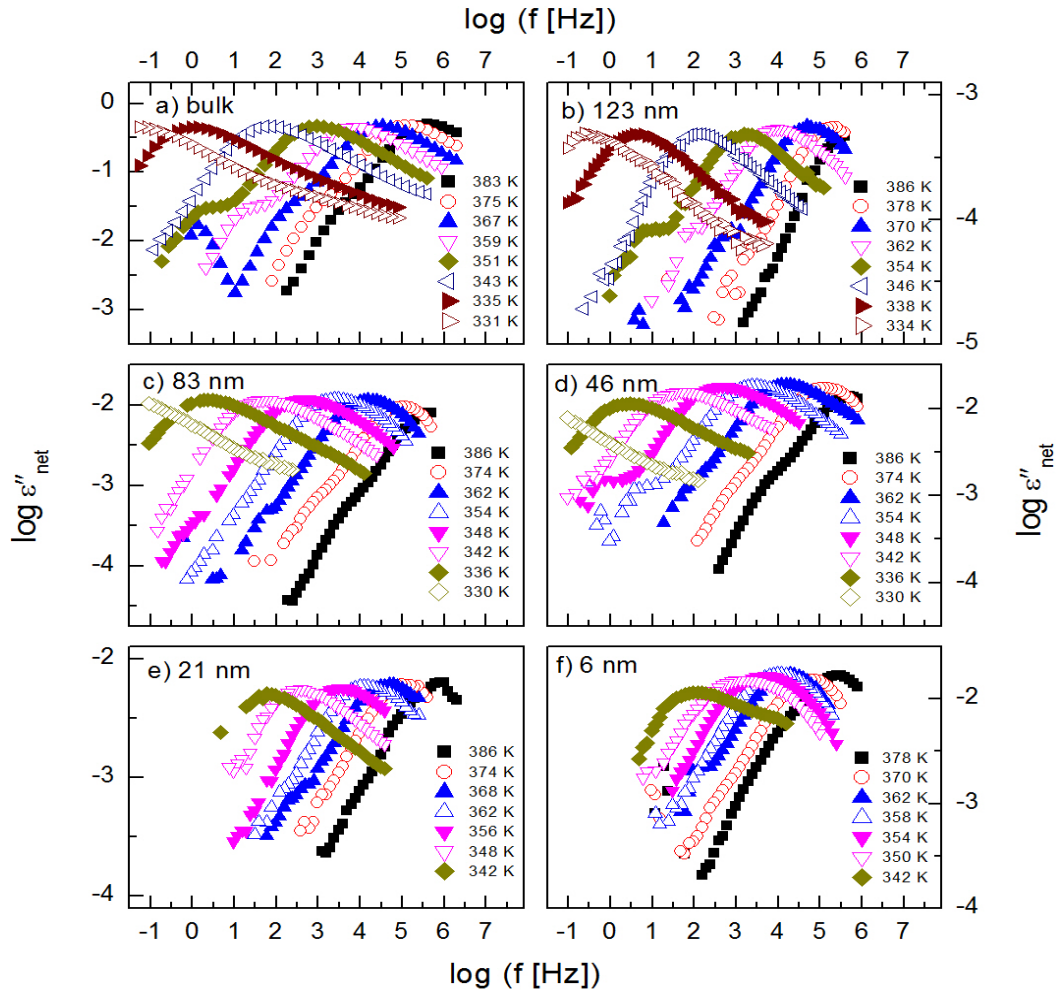


**Figure 4.13.** Dielectric loss,  $\epsilon''_{\text{net}}$ , (after subtraction of the conductivity contribution and the high-frequency wing) measured (in the uncapped geometry) above the glass transition temperature for the bulk material (panel a) and films of various thickness as indicated in panels (b) to (f). Adopted from [235] with permission.

Figure 4.14 shows normalized dielectric loss spectra obtained for all examined samples at 374, 354 and 342 K, that is, temperatures at which, respectively, isotropic, nematic and Smectic A mesophases are expected. In Figure 4.15, the evolution of the mean relaxation rate (for the two molecular processes) with temperature, as well as the film-thickness dependence of the dielectrically-determined glass transition temperature,  $T_g$ , are presented. It is clearly observed that: (i) at a given temperature (in the nematic and isotropic phases), the structural relaxation peak is broadened (on the lower frequency side) for the thin layers

when comparison is made with bulk data (insets-Fig. 4.14a,b); (ii) there is a tendency (in the Smectic A phase) for the  $\alpha$ -peak to narrow down with reducing layer thickness (Fig. 4.14c); (iii) the mean relaxation rate of the  $\alpha$ -process (and hence the dynamic glass transition) remains bulk-like, within the limits of experimental uncertainty, independent of the layer thickness (Fig. 4.15); (iv) the  $\delta$ -relaxation exhibits a pronounced slowing down, for the confined molecules, as the LC is cooled towards the glass transition (Fig. 4.15a); and (v) while it is typical of LCs to have just one relaxation process above the clearing temperature [236], itraconazole has two (Fig. 4.15a). Each of these observations is rationalized in the following discussion.

Concerning the broadening (at high temperatures) of the structural relaxation process with decreasing thickness, theoretical computations were performed to quantify the interaction between itraconazole and the silica substrate. It is shown (Fig. 4.16) that hydrogen bonds – with an average length of about 2.05 Å – are formed between oxygen and OH units belonging to, respectively, the carbonyl moiety in itraconazole and silica surface layer. These are relatively strong interactions especially when kept in mind that, for instance, the average length of the hydrogen bond in water is  $\sim 1.96$  Å [237]. It has been proven that such attractive interactions lead to immobilization [143] of some of the molecules, hence introducing slower modes (which show up as a broadened peak on the long-time side) [147]. This also accounts for the fact that the phase transitions in a thin film (Fig. 4.11) have suppressed peaks, and their respective temperatures are depressed by  $\sim 5$  K. Given the immobilization of some molecules in contact with the substrate, it follows that upon heating through the transition, only a fraction of the liquid-crystal material participates in the disordering. This aspect can be studied concisely by DSC on thin samples via analyzing the intensity of the transition peaks (not included in this thesis).

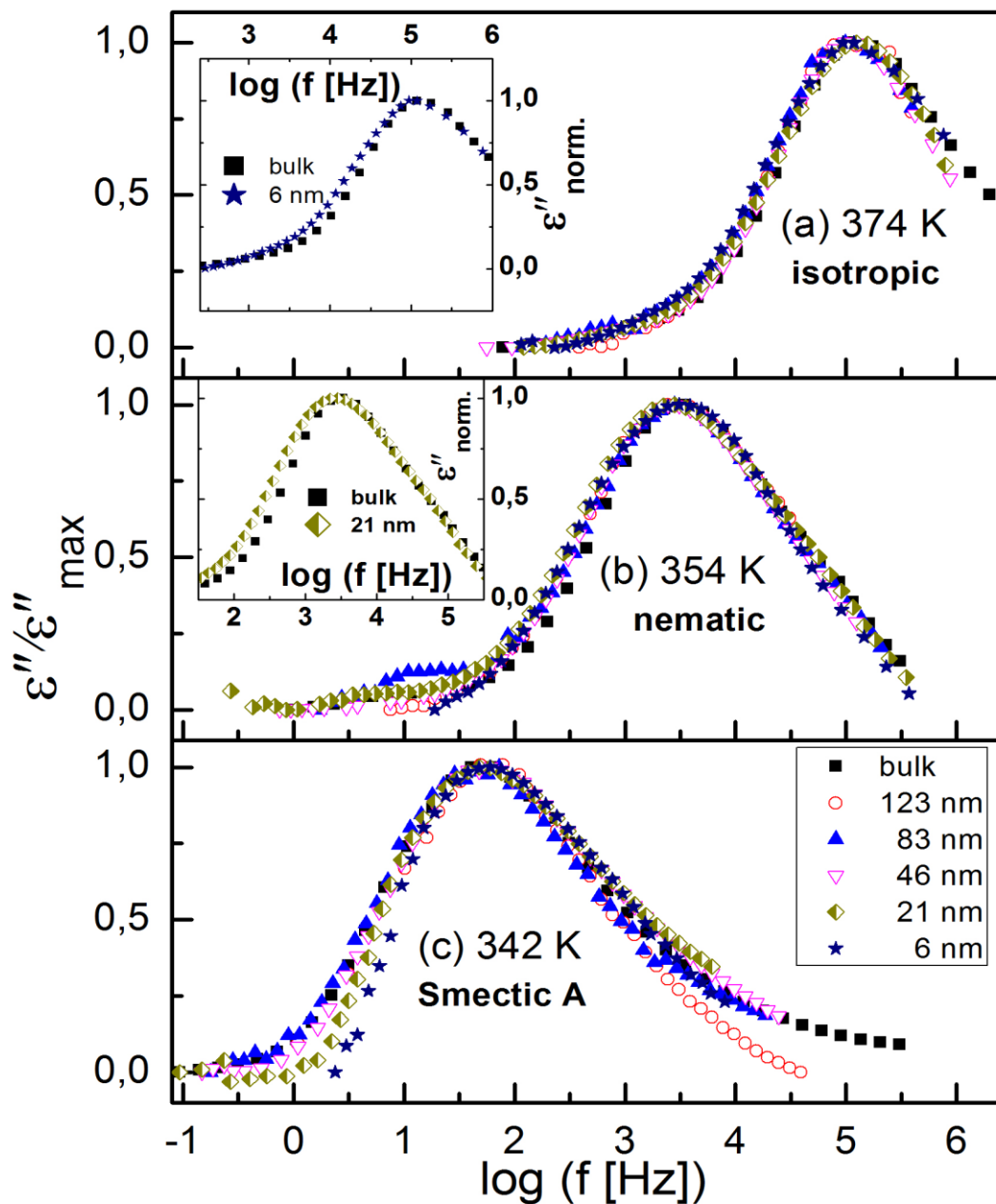


**Figure 4.14.** Dielectric spectra normalized with respect to the maximum of dielectric loss ( $\epsilon''_{max}$ ) of the  $\alpha$ -process at temperatures where the (a) isotropic, (b) nematic and (c) smectic A mesophases are expected. The insets in (a) and (b) compare data for bulk sample and thin films (thicknesses as indicated) at 374 and 354 K, respectively. All measurements on thin films were carried out in the uncapped geometry. Adopted from [235] with permission.

While (attractive) interfacial interactions cause a broadening of the  $\alpha$ -peak, crystalline ordering in the sample promotes its narrowing. These therefore are competing processes, and whichever one dominates is temperature-determined. At low temperatures, i.e., in the smectic A phase, the peak tends to narrow down with reducing layer thickness. To understand this, it must be noted that smectic layering begins at the interface [238], and progresses through the film expanse in the direction perpendicular to the wall; the extent to which smectic ordering permeates the sample volume is therefore inversely proportional to the film thickness. Hence, the thinner the film, the more the order parameter aligns in the direction of the applied electric field.

For the structural relaxation, the temperature-dependencies of the mean relaxation times plotted in Figure 4.15a were fitted by the Vogel-Fulcher-Tammann (VFT) equation (Eq. 2.1). All fitting parameters are collected in Table 4.2. It is clear that the temperature evolution of the mean structural relaxation times in all investigated samples is the same, within the margins of uncertainty. From the VFT fits (not displayed), the glass transition temperature,  $T_g$ , for each sample was evaluated by defining  $T_g$  as the temperature at which structural relaxation time is equal to 100 s. The results are presented in Figure 4.15b where it is manifest that the glass transition temperature of all the studied film samples remains within a margin of  $\pm 2$  K of the bulk value. These findings point to the fact that the extent of confinement reached in these experiments is not restrictive enough to change the dynamic glass transition of itraconazole. The question here is: what is the length scale that underlies the (dynamic) glass transition? Kremer *et al.*[33] have experimentally demonstrated that six molecules (for ethylene glycol) are already sufficient to perform bulk-like dynamics (in terms of the mean relaxation rate), and that such dynamics persist to a length scale as small as 1.5 nm for propylene glycol. This is consistent with experimental [32,239–241], theoretical [242] as well as computational [32] investigations of larger molecules where the length of the basic fluctuating unit has been estimated to be just about a nanometer.

The flip-flop fluctuation of the molecule about its short axis ( $\delta$ -relaxation) is, naturally, a slow process because of its coupling to the centres of mass [243]. Given the tumbling mo-

tions through which the molecules go, it follows that geometrically induced restrictions should further slow down the movement, especially at low temperatures. Since the data in Figure 4.15 does not reveal a thickness-dependence of the slowing down, it is inferred that the main cause of this phenomenon is the spin casting process itself. A number of studies have shown that the spin-coating procedure introduces conformational changes [244,245] which have a direct consequence on the ensuing molecular dynamics [146,174,246,247].

**Table 4.2.** VFT parameters of the  $\alpha$ -relaxation process for the studied samples, and the respective  $T_g$  values obtained as discussed in the text.

Sample	Log $\tau$	$D_T$	$T_0$	$T_g \pm 1 K$
<b>Bulk</b>	$-9.8 \pm 0.1$	$635.8 \pm 27.3$	$305.2 \pm 0.7$	332.5
<b>123 nm</b>	$-10.4 \pm 0.2$	$777.9 \pm 49.2$	$300.5 \pm 1.8$	332.4
<b>83 nm</b>	$-11.1 \pm 0.2$	$972.0 \pm 48.4$	$294.6 \pm 1.3$	332.7
<b>46 nm</b>	$-10.2 \pm 0.1$	$729.6 \pm 23.9$	$301.1 \pm 0.7$	332.1
<b>21 nm</b>	$-10.5 \pm 0.1$	$801 \pm 17$	$298.3 \pm 0.5$	331.9
<b>6 nm</b>	$-10 \pm 1$	$684.6 \pm 296.1$	$299.8 \pm 10.5$	331.5

Finally, attention is turned to the presence of two relaxation processes above the clearing temperature. Typically, only one relaxation process is expected in the isotropic mesophase because the liquid state dominates. The two processes registered in (bulk and confined) itraconazole, however, suggest that the molecules can still undergo distinguishable motions about their short and long axes, as would be the case in the more-ordered phases. Theoretical predictions [248], and some X-ray diffraction (XRD) experiments have hinted at the existence of nematic clusters [249–252] which may not disappear [253] even at high temperatures in some LCs. Consequently, local, randomly oriented nematic-ordered structures (clusters) – without long-range ordering – can be found in the isotropic liquid phase. Our dielectric results therefore provide proof of the existence of a locally ordered phase in the temperature regime where isotropism should prevail.

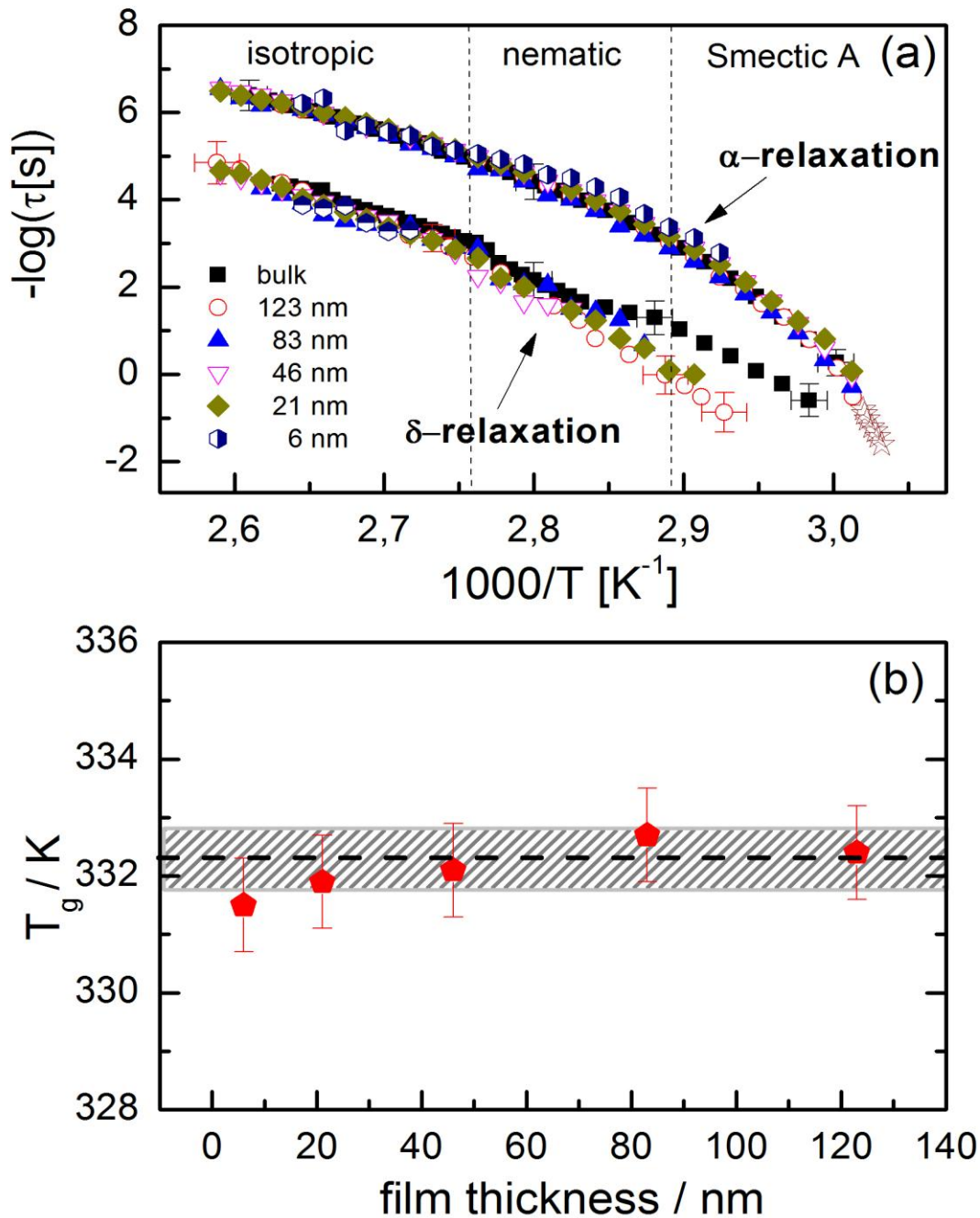


**Figure 4.15.** (a) The temperature- dependence of the mean relaxation times for the  $\alpha$ - and  $\delta$ -processes for different layer thicknesses. The star symbols represent data obtained (from Ref.[226]) by temperature-modulated DSC for the bulk sample; (b) the dielectrically-determined glass transition temperature for the layers. The dashed line in (b) represents the calorimetric bulk  $T_g$  with its experimental error of  $\pm 0.5 \text{ K}$  included (shaded region) for completeness. Adopted from [235] with permission.

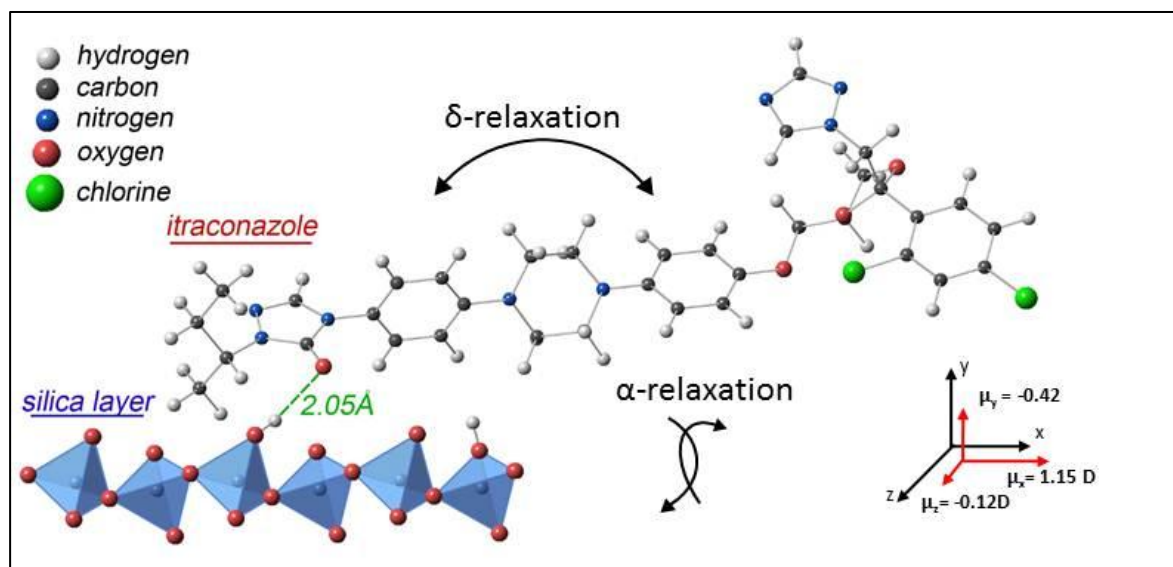


**Figure 4.16.** A visualization of interaction between deposited itraconazole and silica as obtained via theoretical computations. The two relaxation processes present in this molecule are also illustrated, together with (calculated) values of the components of the net dipole moment in 3D space. Adopted from [235] with permission.

#### 4.3.4 Summary

The molecular dynamics of confined itraconazole have been investigated and compared to the bulk material. It is shown that the mean structural relaxation times – and hence the dynamic glass transition – remain bulk-like in the accessible temperature range even for the thinnest studied sample of 6 nm. The distribution of these relaxation times is affected by two competing events: the interfacial interactions and crystalline ordering in the sample. It is also demonstrated that confinement of itraconazole in thin layers slows down the molecules' flip-flop motion (about their short axes) as the glass transition is approached from the upper side. These results provide further understanding of liquid crystal behaviour in confinement, and bear direct consequences to their applicability in nanotechnology.



## 4.4 Segmental and chain dynamics in nanometric layers of poly(*cis*-1,4-isoprene)

### 4.4.1 Introduction

Most of the attention in confinement studies has been paid to the effect of geometric or size-restrictions on short-time scale motions ( $\alpha$ - and  $\beta$ -relaxations) of glass formers [254,255]. These studies have shown, for example, that the segmental relaxation is largely unaffected, in its rate, by the geometrical restriction of thin films [69–71,83,89,94,107,117,138,148,174,175,211,246]. Longer-time scale motions [256–258] (so-called normal modes) have not received as much attention. The reason for this – at least with respect to BDS – is the fact that there is just a handful of so-called *Type A* [259] polymers which can be synthesized with narrow molecular-weight distributions. Poly(*cis*-1,4-isoprene) (PI) is one such polymer which, therefore, presents a unique opportunity to simultaneously probe the segmental and normal mode processes. Because of the lack of symmetry in its chemical structure, it has non-zero components of the dipole moment perpendicular and parallel to the chain contour; the former causes a dielectric relaxation due to segmental motions, while the latter is responsible for the normal mode process [47,259]. In this Section, the effects of confinement are investigated for a series of molecular weights,  $M_w$ , by systematically varying the layer thicknesses,  $d$ , from bulk to dimensions comparable to the respective radius of gyration,  $R_g$ . Furthermore, a hitherto presumed parameter is explored: the concentration,  $c$ , of the spin-cast solution. In the final part, first results are presented for PI confined in Anodic Aluminium Oxide (AAO) membranes and compared with the case of thin layers. By this it is demonstrated that molecular dynamics exhibit a dependence on the dimensionality of confinement.

## 4.4.2 Experimental details and data analysis

### 4.4.2.1 Sample preparation

All the poly(*cis*-1,4-isoprene) (Polymer Source Inc.) thin layers (for properties, see Table 4.3) were prepared by spin-casting from chloroform (Sigma-Aldrich, purity  $\geq 99.9\%$ ) solutions at a rate of 3000 rpm. Always handled using glass syringes (neoLab GmbH), the solutions were filtered through PTFE (polytetrafluoroethylene) membranes with 200-nm pores. In one series of the experiments, for different molecular weights, the layer thicknesses were systematically decreased by reducing the concentration of the polymer in (semi-dilute) solution, and carrying out one spinning process. In another, several thin layers with nearly the same thickness (from PI-53) were prepared from solutions with varying concentrations (from semi-dilute to dilute regimes). In this case, with reducing concentration, several depositions had to be made to attain the required film thickness. All the films – supported on highly conductive silicon wafers – were annealed at 400 K for 24 h in an oil-free high vacuum ( $10^{-6}$  mbar).

**Table 4.3.** Characteristics of the PI samples Adopted from [61] with permission.

Sample*	$10^3 M_w$	$M_w/M_n$	$\langle R_{EE}^2 \rangle^{0.5\#}$ (nm)	$\langle R_g^2 \rangle^{0.5\&}$ (nm)	$T_g^{\&}$ $\pm 0.5 K$
PI-12	11.6	1.06	8.9	3.5	208.3
PI-25	24.5	1.06	11.4	5.3	209.2
PI-45	44.5	1.06	17.4	6.9	208.8
PI-53	53	1.06	19	7.5	209.4
PI-75	75	1.08	22.6	9	210.4

\*The microstructure (data provided by Polymer Source Inc. – Canada) is 80% (*cis*-1,4), 15% (*trans*-1,4) and 5.0% (*vinyl*-3,4) for all samples. #Calculated [69] assuming a Gaussian chain,  $\langle R_{EE}^2 \rangle = Na^2$ , where N is the degree of polymerization and  $a$  is the statistical segment length,  $a = 0.68$  nm. §Evaluated [82] as  $\langle R_g^2 \rangle = 1.07 \times 10^3 M_w$ . &Measured by differential scanning calorimetry at a cooling rate of 10 K/min.

The dielectric measurements of the bulk samples were done using a high resolution Alpha Analyzer (Novocontrol), while for all the thin layers, the measurements were performed using an Andeen-Hagerling impedance bridge which has an accuracy of  $\leq 10^{-5}$  in  $\tan(\delta)$ , corresponding to an error in the dielectric loss  $\epsilon''$  smaller than the symbol size in all

presentations. Temperature regulation for both systems was executed by a Quattro System (Novocontrol) using a jet of dry nitrogen, thereby ensuring relative and absolute errors better than 0.1 and 2 K, respectively.

For 2-dimensional confinement studies, AAO membranes with uni-directional pore channels were purchased from Synkera Technologies Inc., USA, (see Table 4.4) and infiltrated with poly(cis-1,4-isoprene) as detailed in Section 3.3 for dielectric measurements.

**Table 4.4.** Characteristics of the AAO membranes used in this study

	I	II
<b>Diameter of membrane</b> (± 0.2 mm)	13	13
<b>Thickness</b> (± 2 µm)	48	50
<b>Porosity</b> (%)	11	10
<b>Pore diameter</b> (nm)	55 ± 6	18 ± 3
<b>Pore density</b> (cm <sup>-2</sup> )	2.10 <sup>9</sup>	5.10 <sup>10</sup>

#### 4.4.2.2 Data analysis

The empirical Havriliak-Negami (HN) equation (Eq. 3.39) is used in this analysis to quantify the main features of the dielectric relaxation processes observed. Its relaxation time at maximum loss,  $\tau_{max}$  ( $= \tau_{HN} [(\sin(\alpha\gamma\pi/2 + 2\gamma))/(\sin(\alpha\pi/2 + 2\gamma))]^{1/\alpha}$ ), not  $\tau_{HN}$ , is used to generate activation plots (Fig. 4.24) since the latter is a function of shape parameters  $\alpha$  and  $\beta$ . When  $\tau_{max}$  has a non-Arrhenius temperature dependence, as is characteristic of the structural relaxation for all glass formers, it is described by the Vogel-Fulcher-Tammann (VFT) equation [8–10]:

$$\tau_{max}(T) = \tau_0 \exp\left(-\frac{DT_V}{T-T_V}\right) \quad (4.4)$$

where  $\tau_0$  and  $D$  are fit parameters (the latter is referred to as the fragility parameter, and is oft used to quantify the extent by which the temperature-dependence of the relaxation times deviates from Arrhenius behaviour) and  $T_V$  is the so-called Vogel temperature. It has

been shown that the normal mode in bulk PI is also VFT-like [47,261]. The VFT equation is mathematically equivalent to the Williams-Landel-Ferry (WLF) equation [262] which reads

$$\log \frac{\tau_{max}}{\tau_0} = \frac{C_1(T-T_0)}{C_2+T-T_0} \quad (4.5)$$

where  $T_0$  is a reference temperature,  $\tau_0$  is the corresponding relaxation time, and  $C_1$  and  $C_2$  are fitting parameters. The parameters of these two equations are related [47] by  $DT_V = C_1C_2$  and  $T_V = T_0 - C_2$ .

Combining Eq. (3.39) and Eq. (4.4), and assuming a temperature independence of the dielectric strength and shape parameters, delivers a temperature-dependent description of the complex dielectric function:

$$\varepsilon^*(\omega) = \varepsilon_\infty + \frac{\Delta\varepsilon}{\left[1 + \left(i\omega\tau_0 \exp\left\{-\frac{DT_V}{T-T_V}\right\}\right)^{\alpha\beta}\right]} \quad (4.6)$$

To extract the distribution of relaxation times for the two dynamic processes in PI, each was modelled, as illustrated in Figure 4.17, in a step-by-step manner using Eq. (4.6). First, a function which best describes the segmental mode was calculated and subtracted from the measured (raw) data (Fig. 4.17a). This delivers a separated normal mode peak (Fig. 4.17b), which is then easily modelled as next step (Fig. 4.17c). Figure 4.18 is a representative display of data (PI-45) described using this procedure. Notice that fitting Eq. (4.6) directly to the data would involve at least eight free parameters, a procedure which would not deliver unique values.

With  $\tau_{HN}$  and the shape parameters  $\alpha$  and  $\beta$ , the distribution of the relaxation times,  $L(\tau)$ , is computed employing an analytically derived equation [12,198] of the form

$$L(\tau) = \frac{1}{\pi} x^{\alpha\beta} \{\sin(\gamma\Theta(x))\Omega(x)\} \quad (4.7)$$

where  $x = \frac{\tau}{\tau_{HN}}$ ,  $\Theta(x) = \arctan \left[ \frac{\sin(\pi\alpha)}{x^\alpha + \cos(\pi\alpha)} \right]$ , and  $\Omega(x) = [1 + 2x^\alpha \cos(\pi\alpha) + x^{2\alpha}]^{-x/2}$

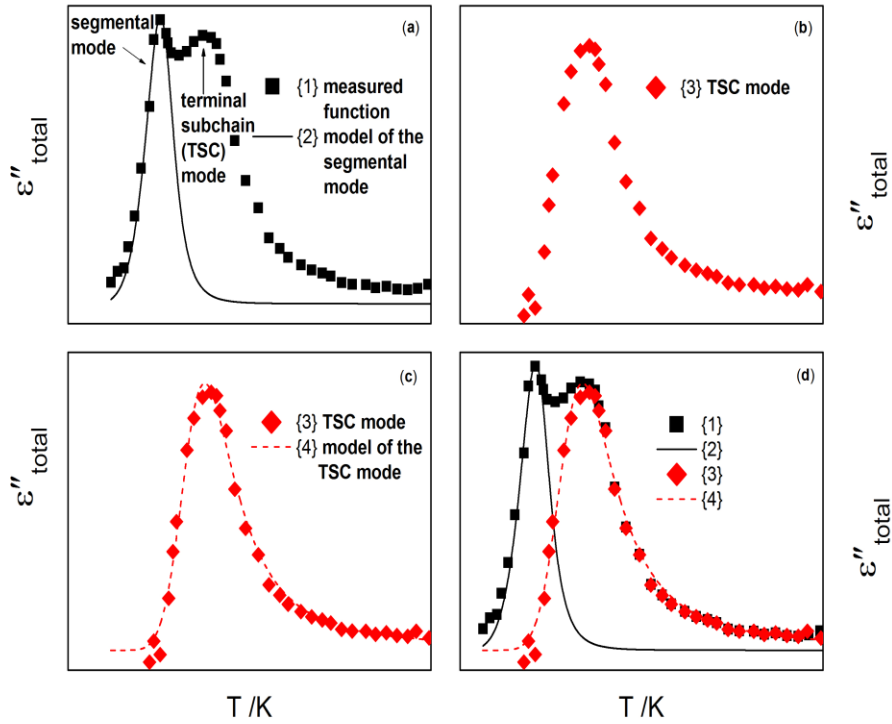


**Figure 4.17.** An illustration of how dielectric loss data in the temperature representation is described step-by-step: a) the raw data {1} showing the two relaxation processes present in a thin spincast PI sample, and a model function {2} calculated using Eq. (4.6) to fit the segmental mode; b) a separated terminal subchain (TSC) mode {3} obtained by subtracting {2} from {1}; c) a model function {4} evaluated to fit the TSC mode; and d) a plot showing all the functions {1}, {2}, {3}, and {4}. Adopted from [263] with permission.

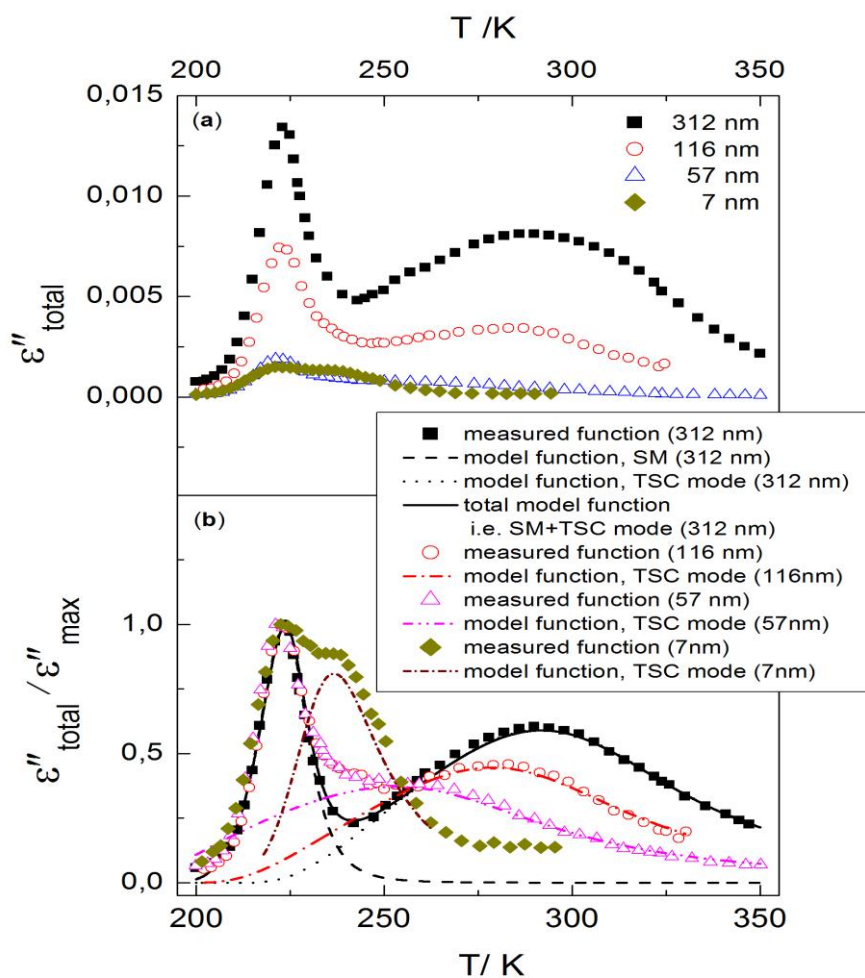


**Figure 4.18.** (a) The measured dielectric loss,  $\epsilon''_{total}$ , plotted as a function of temperature (at 80 Hz) for thin layers (thicknesses indicated) prepared from PI-45. (b) The same data in (a) normalized w.r.t. the maximum loss value of the segmental mode (SM). The lines represent functions (shown in the normalized data for graphical clarity) calculated to describe the data as explained in Figure 4.17. The parameters used to construct these model functions are recorded in Table 4.5.

#### 4.4.3 Results and discussion

It is conventional in this kind of studies to vary the concentration of the polymer in solution in order to tune the film thickness. Figure 4.19 presents the results for such a study for PI-12 and PI-75 where all samples were prepared from semi-dilute solutions by a single deposition procedure. Here, the layer thicknesses were systematically adjusted from bulk to dimensions comparable to the radius of gyration,  $R_g$ , of the respective chain in bulk. It is

evident, for both molecular weights, that the segmental peak remains unaffected – in its spectral position and shape – within the limits of experimental uncertainty. Concerning chain dynamics, for  $M_w \cong M_c$  (PI-12;  $M_c$  is the cross-over molecular weight from Rouse to reptation dynamics and is equal to 10 000 g/mol), the normal mode remains bulk-like in its relaxation rate down to the thinnest layer ( $d = 6$  nm) studied, that is,  $d \sim 1.7R_g$  (Fig. 4.19a,c,e). For  $M_w = 7.5M_c$  (PI-75), the normal mode for all the thin layers is not bulk-like in its relaxation rate and shape. It is therefore referred to as the terminal subchain (TSC) mode (and explained it later). Observation is made of the fact that the TSC modes become faster and reduce in their dielectric strength upon increasing confinement (Fig. 4.19b,d,f).

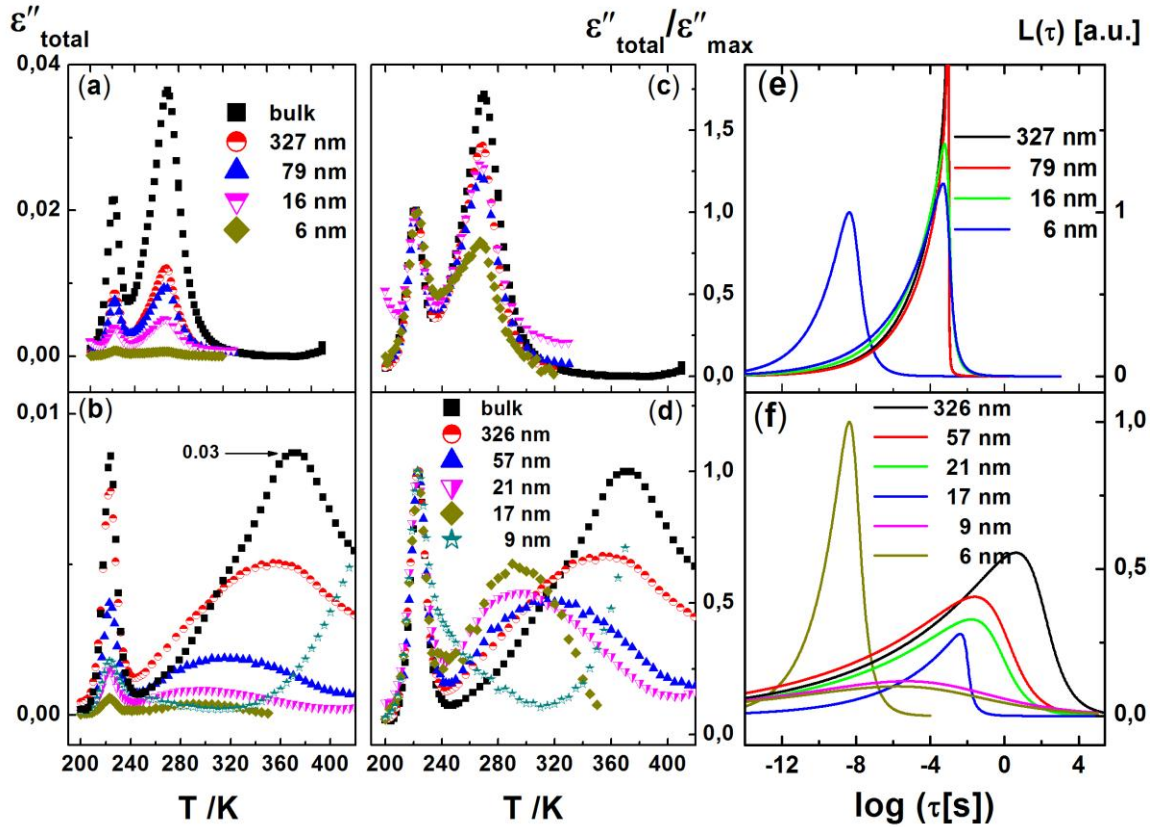


**Figure 4.19.** Temperature dependence of the imaginary part,  $\epsilon''_{total}$ , of the measured complex permittivity at 80 Hz for (a) PI-12 and (b) PI-75. In (c) and (d), respectively, the same dielectric data is shown normalized w.r.t. the maximum loss value of the segmental mode. (e) and (f) display the corresponding relaxation time distribution functions at  $T = 312$  K. Panels (a) & (c), and (b) & (d) share common legends. The bulk data in (b) is not plotted to scale w.r.t. y-axis. Adapted from [146] with permission.

In order to check how these results would evolve with a gradual variation of molecular weights, three more molecular weights (lying between PI-12 and PI-75) were investigated. Figure 4.20 is a summary of the results at a representative frequency of 80 Hz. It is observed that (i) irrespective of the molecular weight, the segmental mode is not shifted by a reduction in film thickness; (ii) its shape parameters (see Table 4.5) remain invariant with thickness, even when  $d \approx R_g$ , implying an unbroadened peak at this level of confinement; and (iii) TSC modes are present, vary in their shape (Table 4.5) and approach the segmental mode with decreasing film thickness (see also Fig. 4.21).

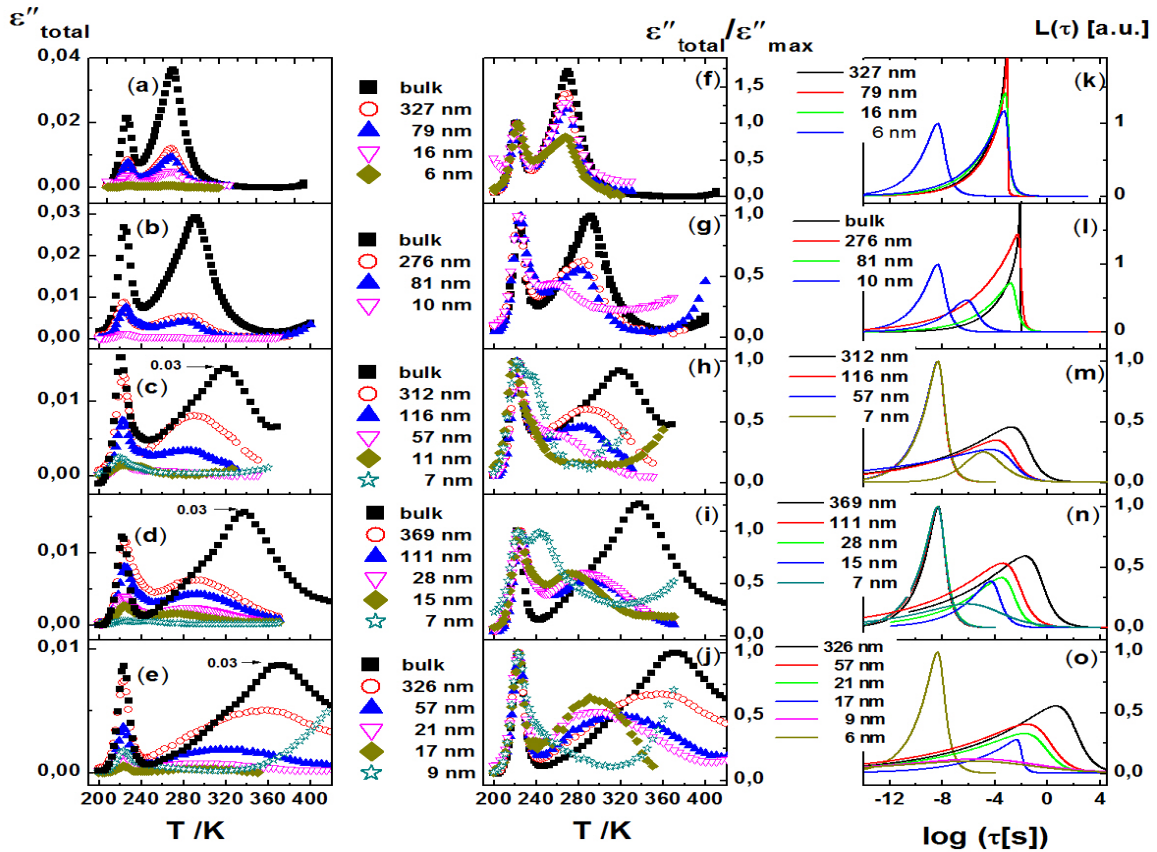


**Figure 4.20.** Temperature dependence of the imaginary part,  $\varepsilon''_{total}$ , of the complex permittivity at 80 Hz for (a) PI-12, (b) PI-25, (c) PI-45, (d) PI-53, and (e) PI-75. In (f)-(j), respectively, the same dielectric data is shown normalized w.r.t. the maximum loss value of the segmental mode. (k)-(o) display the corresponding relaxation time distribution functions at  $T = 312$  K. The bulk data in (c), (d) and (e) does not share the same y-axis scale with the rest of the curves. Adapted from [146] with permission.



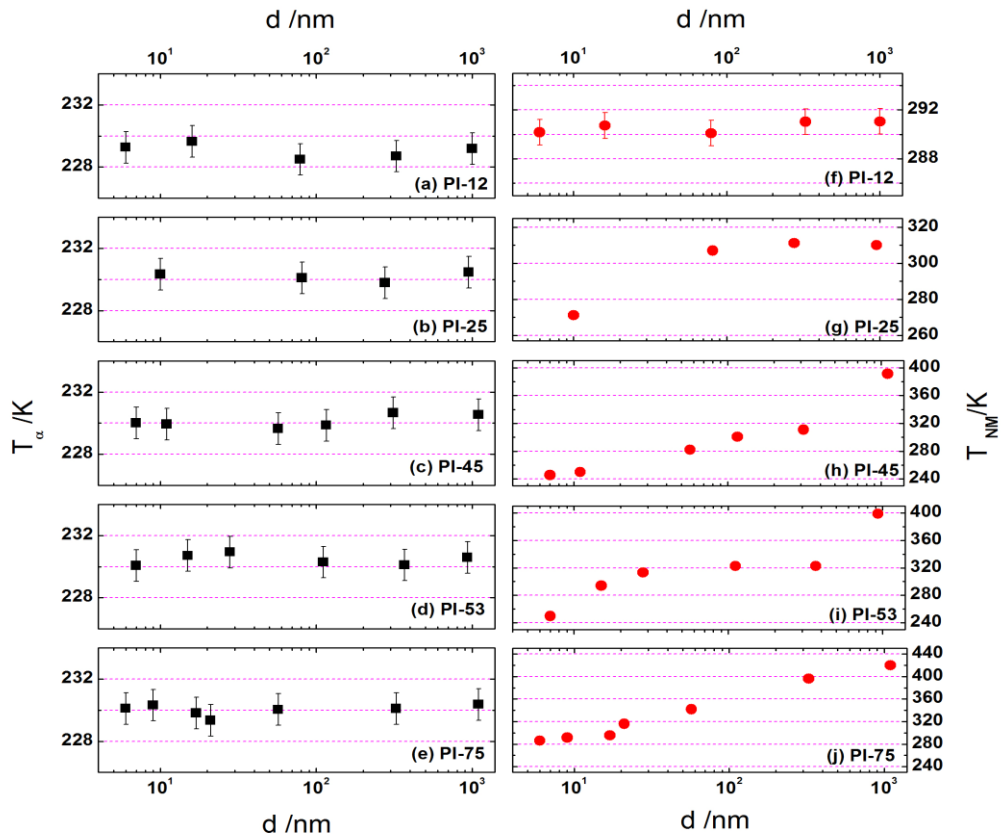


**Figure 4.21.** Thickness ( $d$ )-dependence of the characteristic temperature  $T_\alpha$  (left panels) and  $T_{NM}$  (right panels) for the segmental- and normal modes, respectively, as measured at 1 kHz for different molecular weights (as indicated) of PI. Unless indicated, the experimental uncertainty is smaller than the size of the symbols.

It is significant to note that the results so far presented involve a variation of the concentration of the mother solution used to prepare the thin layers. However, the findings for PI-12 point to the fact that entanglements play a role in the chain dynamics. To probe this intuition further, experiments were carried out in such a way that the film thickness and molecular weight are kept constant, but the solution concentration,  $c$ , systematically varied.

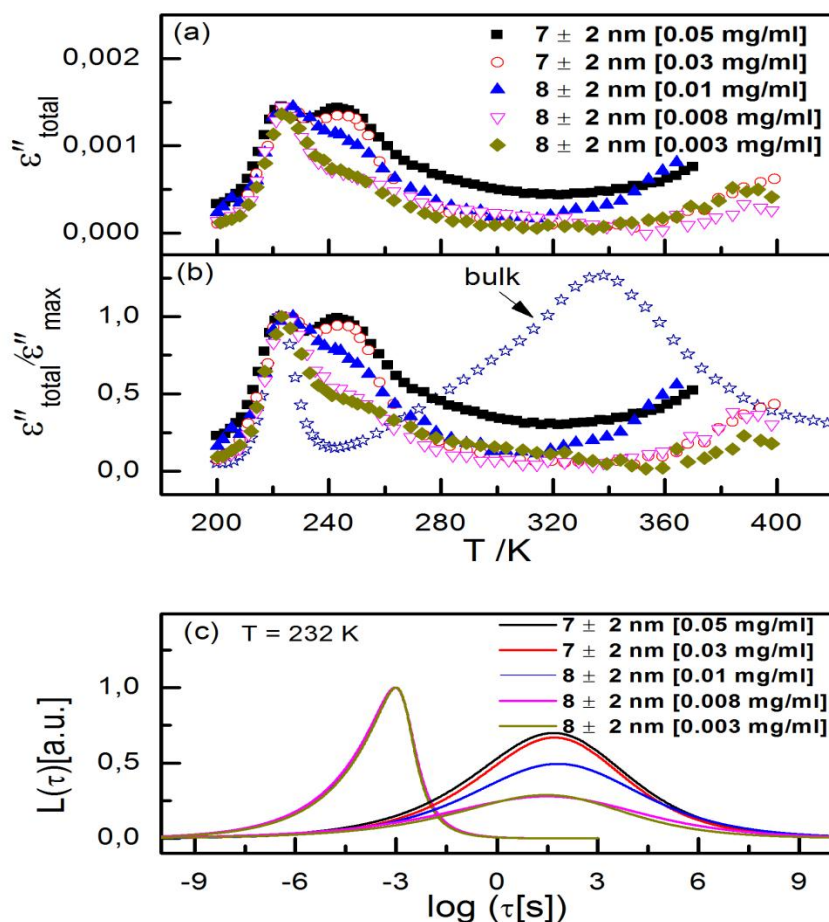


**Figure 4.22.** (a) Dielectric loss  $\epsilon''_{total}$  versus temperature at 80 Hz (PI-53) for thin layers of thickness  $\sim 7$  nm, each prepared from a different solution (in terms of concentration,  $c$ ), with  $c$  varied from dilute (0.008 mg/ml) to semi-dilute (0.05 mg/ml) regimes. In (b), the same data is shown normalized w.r.t. the maximum loss value of the segmental mode. For comparison, data for a bulk sample is included. Panels (a) and (b) share a common legend. (c) The relaxation time distributions at  $T = 232$  K for the various thin layers. Notice that all curves for the segmental mode superimpose. Inset – the number of depositions (made to get  $\sim 7$  nm of film) plotted to show its dependence on the concentration of PI in solution. Adapted from [146] with permission.

Figure 4.22 is a plot of the results thus obtained (PI-53) and shows the dielectric loss (as a function of temperature) in its dependence on the concentration,  $c$ , of the mother solution used to deposit thin layers.  $c$  was varied from 5.15 to 0.32 % vol. of PI, that is, from semi-

dilute to dilute regimes, and several samples with thickness  $d \approx 7$  nm prepared. In order to attain this same thickness, the number of depositions required (at the same spinning rate) had to be increased with reducing concentration. It is evident for all samples studied, when compared to bulk, that the temperature position of the segmental relaxation peak remains unchanged. Additionally, the TSC mode – shifted by about 95 K to lower temperatures – is present, and its strength reduces with decreasing concentration of the mother solution (Fig. 4.22a,b). The corresponding distributions of the relaxation times for both the segmental and TSC modes are shown in Figure 4.22c, and confirm the unaffected nature of the former mode, together with the  $c$ -dependence of the latter.

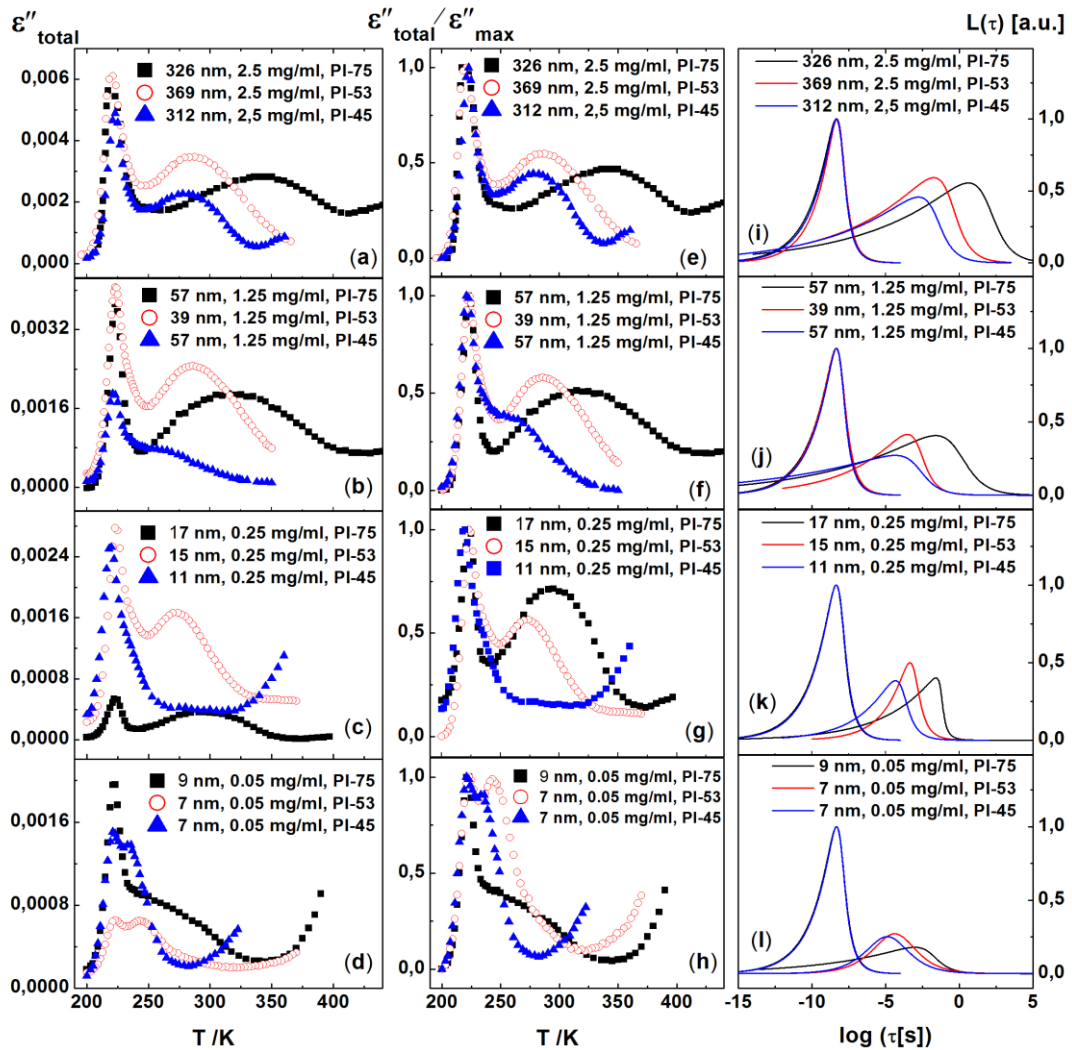


**Figure 4.23.** Temperature dependence (at 80 Hz) of the measured dielectric loss,  $\epsilon''_{total}$ , for thin layers (prepared from different molecular weights of PI, but the same solution concentrations) with comparable thicknesses: (a) 312-369 nm; (b) 39-57 nm; (c) 11-17 nm; and 7-9 nm. The same data normalized w.r.t. the maximum loss value of the segmental mode is plotted in (e)-(h). Panels (i)-(l) show the respective distribution of relaxation times at 312 K. Adapted from [146] with permission.

**Table 4.5.** Havriliak-Negami (HN) shape parameters. Adapted from [146] with permission.

Sample	Thickness (nm)	Segmental mode		Normal mode	
		$\beta$	$\gamma$	$\beta$	$\gamma$
<b>PI-12</b>	Bulk	0.74	0.46	0.99	0.84
	327	0.74	0.43	0.95	0.85
	79	0.72	0.42	0.97	0.82
	16	0.71	0.42	0.96	0.79
	6	0.73	0.41	0.92	0.75
<b>PI-25</b>	Bulk	0.72	0.41	0.69	0.52
	276	0.71	0.42	0.54	0.45
	81	0.72	0.40	0.49	0.47
	10	0.69	0.43	0.50	0.38
<b>PI-45</b>	Bulk	0.74	0.45	0.99	0.40
	312	0.72	0.40	0.55	0.14
	116	0.72	0.40	0.55	0.14
	57	0.71	0.41	0.51	0.10
	11	0.70	0.43	0.55	0.84
	7	0.71	0.42	0.39	0.90
<b>PI-53</b>	Bulk	0.72	0.49	0.71	0.35
	369	0.71	0.45	0.54	0.15
	111	0.70	0.42	0.54	0.15
	28	0.69	0.43	0.54	0.21
	15	0.70	0.41	0.65	0.30
	7	0.70	0.42	0.28	0.35
<b>PI-75</b>	Bulk	0.73	0.51	0.63	0.36
	326	0.70	0.40	0.50	0.14
	57	0.70	0.40	0.45	0.14
	21	0.71	0.40	0.47	0.15
	17	0.69	0.40	0.85	0.15
	9	0.70	0.40	0.17	0.35
	6	0.70	0.40	0.17	0.34

The preceding experimental findings can be summed up as follows: (i) the segmental relaxation, i.e. the dynamic glass transition in poly(*cis*-1,4-isoprene) is not shifted or broadened independent of all the studied parameters; in contrast (ii) the chain dynamics corresponding to the fluctuation of the end-to-end vector of the polymer chain or of the free tails of tethered chains (terminal subchains, TSC), are strongly affected by the concentration from which the polymer layers are deposited, the thickness of the layers, and the sample molecular weight. An interpretation of these observations is mainly of a qualitative nature because atomistic simulations of the dynamic glass transition, and more importantly of entangled systems, are not yet available.

It has been generally [240,241,264], and specifically for PI [239], shown that the segmental mode is a fluctuation occurring at a length scale of about 2 to 3 chain segments, corresponding to about 7 Å. This is a size far below the external, one-dimensional confinement of  $d \geq 6$  nm, given by the layer thickness (Fig. 4.25). At this extent of confinement, no changes in the dynamic glass transition are expected, at least for measurements carried out in the linear-response regime [144]. As has been recently proven for poly(vinylpyridine) on silica [147], certainly some polymer segments at the polymer-substrate interface (for the case of predominantly attractive interactions) will be immobilized [143], with respect to the time-scale of the experiment. This explains the reduction in the dielectric strength of the segmental mode as, for instance, observed in Figure 4.20. Unfortunately, we cannot carry out a quantitative analysis of the dielectric strength because of the geometry applied in these measurements – there are inaccuracies in defining the macroscopic evenness of the nanostructures at extensions of 4 mm.

An elaborate discussion of the chain dynamics is provided in the following discussion. In the bulk state, the main parameters of a chain depend on the macromolecular nature of the material, with the characteristic dimension being the radius of gyration,  $R_g$ , which is proportional to the molecular weight. The chain has a Gaussian distribution of the distances of one chain end from the other [163]. As first predicted by Flory [265], a given test chain occupies ~1% of the volume within the nearly spherical region encompassed by the chain itself, while the rest is occupied by many other entangled chains and free volume. The

length scale characterizing the chain dynamics is therefore that of the end-to-end distance (Fig. 4.25a). However, this conformation of the chain must be modified when it comes in contact with a solid substrate (Fig. 4.25b), or when spincoated from solution into a thin geometrically constrained layer (Fig. 4.25c,d). In the spin coating process, the polymer solution is transferred – within a time much shorter than the time required for the whole chain to relax – to a molten, non-equilibrium state [162], in which most of the solvent is removed.

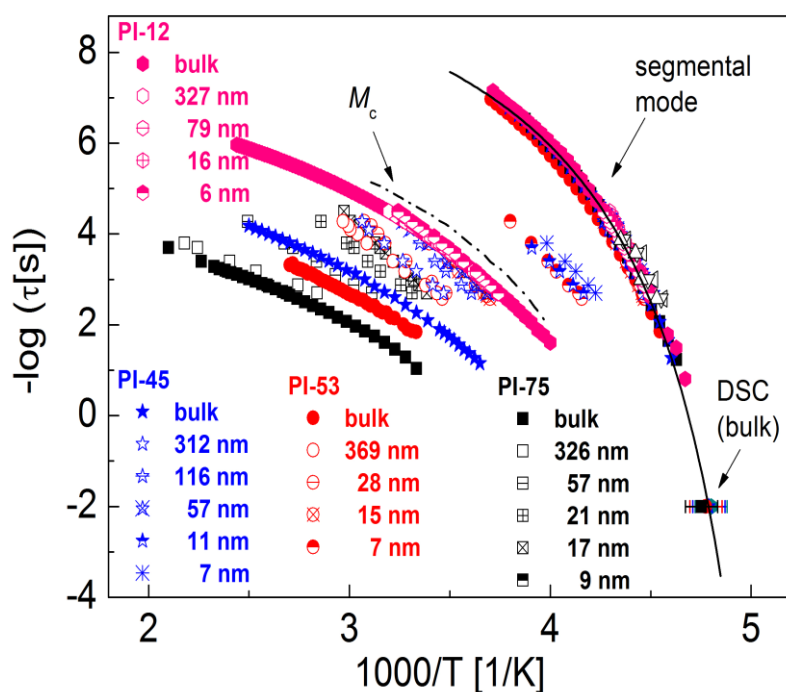


**Figure 4.24.** Activation plot for the segmental, normal, and terminal subchain modes of PI samples prepared from different molecular weights, as indicated. Complementary data obtained from AC Calorimetry for PI-53 is presented by open triangles: bulk (up triangles), 100 nm (down triangles) and 15 nm (side triangles).  $T_g$  data determined for bulk samples by DSC is included as well. The solid line is a VFT fit to the segmental mode, with parameters:  $\log \tau_0 = 10.6$ ,  $DT_V = 299$  K and  $T_V = 185$  K, while the dash-dotted line is calculated for the normal mode as expected for  $M_w = M_c = 10^4$  g/mol. Adopted from [146] with permission.

As observed in the current experiments, this results in a suppression of the normal mode relaxation (Figs. 4.18-4.20, 4.23) in nanometric PI layers and is explained by several fac-

tors which add up: (i) chain segments in the immediate vicinity of, and attractively interacting with the substrate become immobilized, leading to a suppression of the fluctuations of the end-to-end vector; (ii) the end-to-end vector of a chain prepared in a nanometric layer preferentially orients perpendicular to the  $E$  vector of the external electric field in the sample capacitor, and hence its contribution to the relaxation process is no longer dielectrically observable; (iii) topological constraints imposed by the spin-coating procedure might as well interrupt the normal mode process.

For polymer chains prepared from solutions in the dilute regime ( $c = 0.003$  mg/ml), a weak relaxation is observed close to the segmental mode. It is assigned to the relaxation of terminal subchains (TSC) as depicted in Figure 4.25d. The length of the TSC can be estimated from the frequency position of the respective peak to be about 90 segments. Increasing the polymer concentration in the spin-cast solution leads to an overlap of the polymer chains in the semi-dilute regime ( $c > 0.008$  mg/ml), and hence to an increase in the strength of the TSC relaxations (Fig. 4.22a,b). It is also noteworthy that as the concentration of the solution is increased (and hence the number of spin-casting processes reduced), the angle between the TSC and the external field  $E$  increases (Fig. 4.25c,d); this should also account for the increase in the strength of the dielectric response. Remarkably, the relaxation time distribution of the TSC relaxation shows very minimal dependence on the polymer concentration. The TSC relaxation, however, shows pronounced molecular-weight dependence, as demonstrated for samples prepared from semi-dilute solutions (Fig. 4.23). With increasing molecular weight, the peak of the TSC relaxation shifts to higher temperatures corresponding to lower relaxation times.

The fact that entanglements matter for the TSC relaxation is clearly reflected in the  $M_w$ -dependence of the chain dynamics in confinement (Fig. 4.19): for  $M_w = 11.6$  kg/mol, which is close to  $M_c = 10$  kg/mol, the cross-over molecular weight from Rouse- to reptation dynamics, the normal mode is not changed in its spectral position and relaxation time distribution (Fig. 4.19a,c,e) – only the strength of the relaxation is decreased. This is in pronounced contrast to all measurements on samples having  $M_w \gg M_c$ , where TSC relaxations are observed.

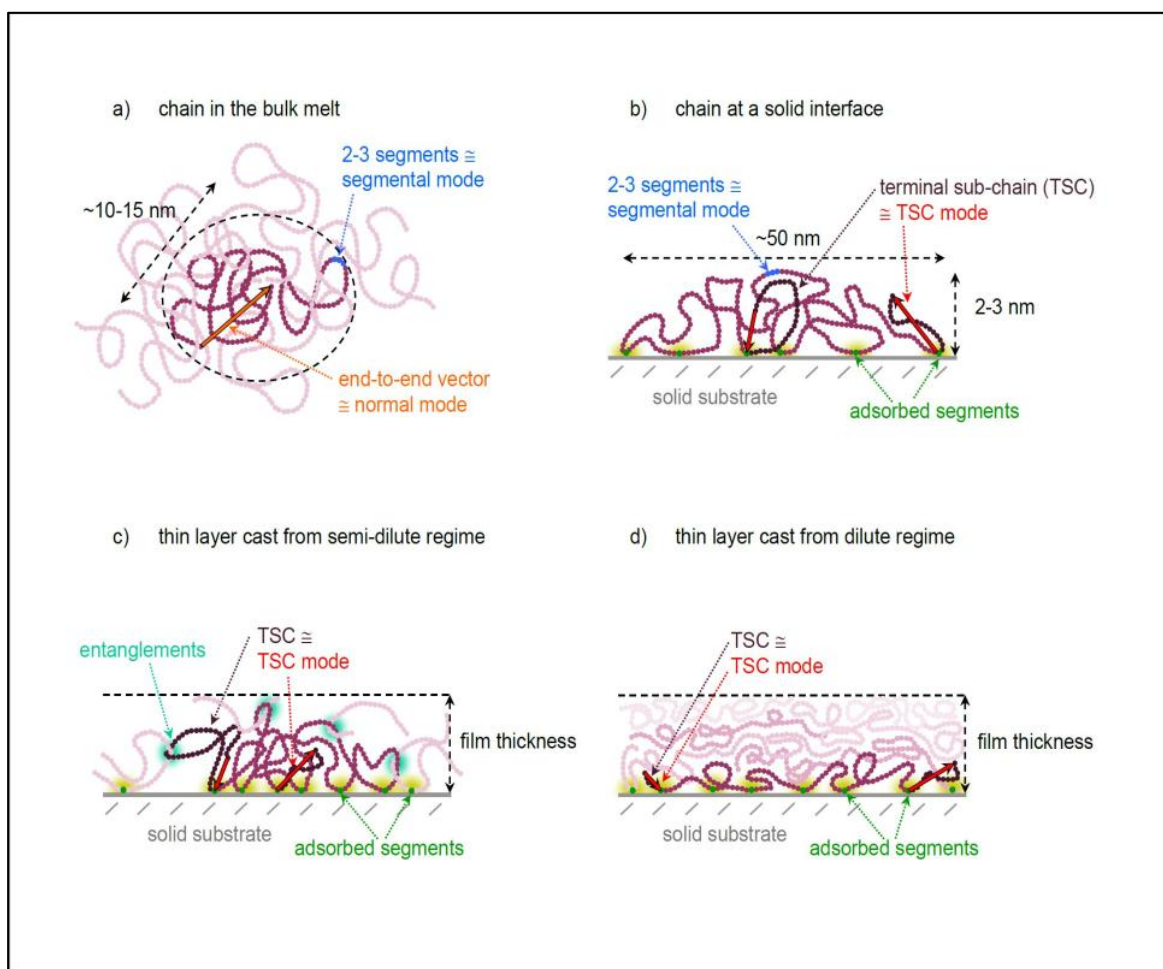


**Figure 4.25.** Schematic representation of different polymer chain conformations induced by preparation. In the bulk melt, the chain has its equilibrium conformation and the molecular relaxations detected by BDS correspond to the segmental motions as well as the fluctuations of the end-to-end vector (a). In thin layers the interaction with the solid substrate leads to adsorption of chain segments directly at the interface which are therefore immobilized (b). This interferes with the bulk normal mode: the dipole moment along the chain between pinned segments cannot perform fluctuations anymore; hence, only the free chain ends after the first and/or last adsorbed segment, the so-called terminal subchains (TSC), perform relaxation motions which we refer to as TSC modes. Spin-casting a thin layer from a semi-dilute solution (where chains still have overlap/entanglements) presumably results in an entangled network (c) with adsorption of segments causing TSCs. For preparations from dilute concentrations (no overlap/entanglements of chains) several depositions are necessary which suggests that chains individually wet the substrate and are strongly stretched in parallel to the substrate (d). Consequently, the dipole moment of the TSC has only a minor component in the direction of the applied electrical field, causing a reduction in the strength of the detected signal. Adopted from [266] with permission.



As reviewed in the Section 2.3, the Rouse and reptation theories, respectively, predict  $M^2$  and  $M^3$  dependencies of the mean relaxation times of the normal mode, below and above  $M_c = 10^4$  g/mol. In Figure 4.26, a plot of the mean relaxation times *versus* molecular weight is presented as a function of PI layer thickness. It must be clarified here that, for the thin layers, the molecular weights presented are those of the mother (starting) sample before dissolution in chloroform. The relation  $\tau \propto M^{3.5 \pm 0.1}$  is found for the bulk samples, quite in quantitative agreement with reported results in literature, e.g., in [47,255] (see inset Fig.4.26). For the case of spin-cast samples, a gradual reduction in the gradient of the  $\log \tau$  *versus*  $\log M_w$  plots is noted as the layer thickness is decreased. It is thus inferred that the dynamics of the TSC modes approach Rouse dynamics with reducing layer thickness, even though the mother chains are entangled.

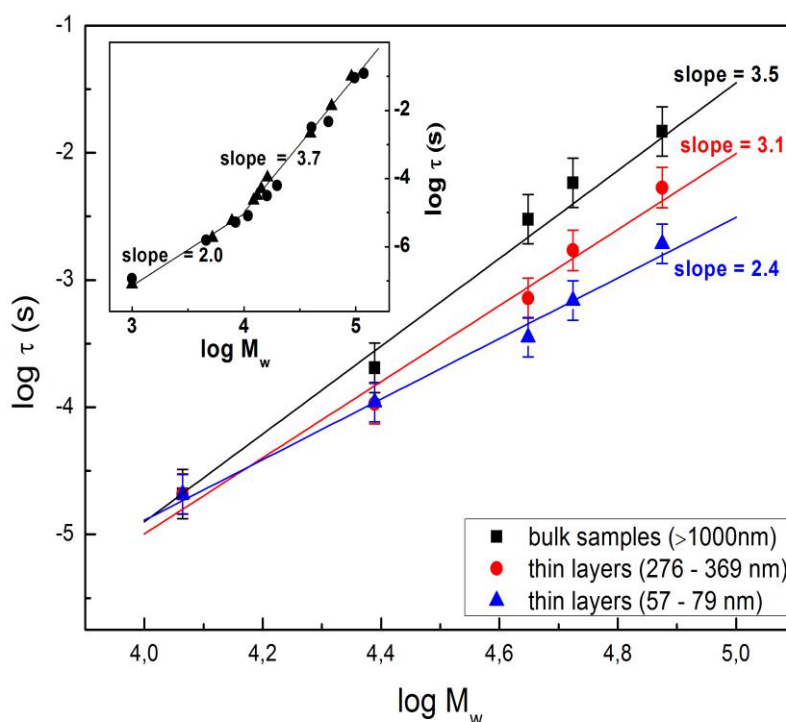


**Figure 4.26.** Dependence of the mean dielectric relaxation time on molecular weight,  $M_w$ , for the normal mode (bulk samples) and terminal subchain mode (spincast layers) of poly(*cis*-1,4-isoprene) at 320 K. Inset: data for bulk linear PI is adapted with permission from [47].

#### 4.4.3.1 1- versus 2-D confinement of poly(*cis*-1,4-isoprene)

It is considered here that thin films (with one free interface) impose a one-dimensional (1-D) confinement, since a given chain experiences constraints only in one direction, while, with the same reasoning, uni-directional nanopores offer a two-dimensional (2-D) confining space.

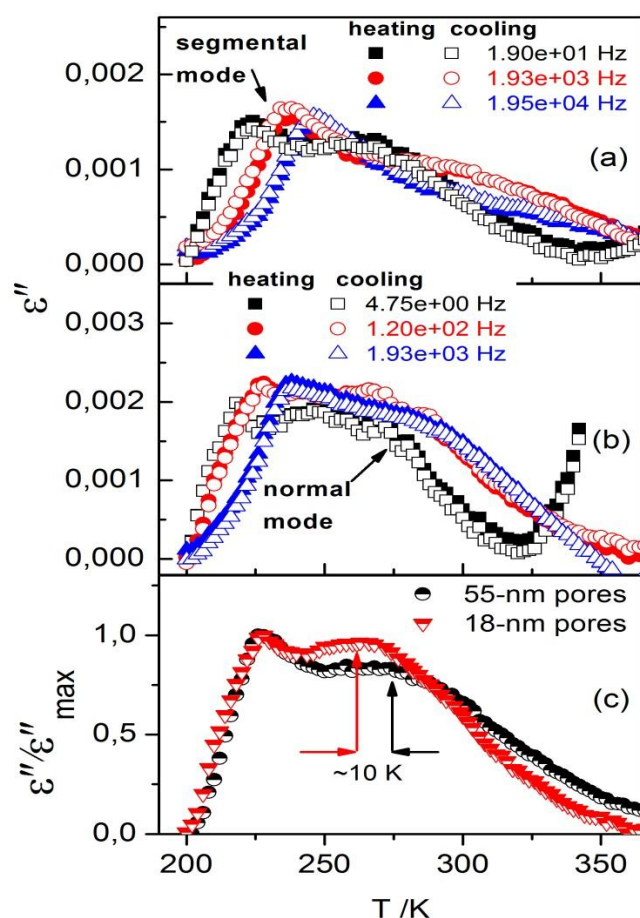


**Figure 4.27.** Dielectric loss  $\epsilon''$  (for PI-53) versus temperature (heating and cooling runs), after subtraction of the AAO background, as obtained for templates with pores of average diameter (a) 55- and (b) 18-nm. In (c) normalized loss data (measured at 120 Hz) is plotted, for comparison, as function of temperature for PI-53 in 55- and 18-nm pores. Adopted from [263] with permission.

Figure 4.27 shows dielectric loss data (after subtraction of the alumina background) for PI-53 measured in AAO nanopores – pore diameter, 55 nm (Fig. 4.27a) and 18 nm

(Fig. 4.27b). As evident in these plots, the two dynamic processes present in PI are clearly visible; the low-temperature process corresponds to the segmental relaxation, and hence the dynamic glass transition, while the slower process is that of the (sub)chain fluctuations. Furthermore, given the coincidence between the cooling and heating runs, it is established that the samples are stable (with regard to the measured dielectric response) and that the measurements are reproducible. The pore-size dependence of the molecular dynamics is summarized in Fig. 4.27c: while the temperature positions of the loss maxima (segmental mode) overlap, the maxima of the TSC modes are separated by about 10 K. This observation will be rationalized later.

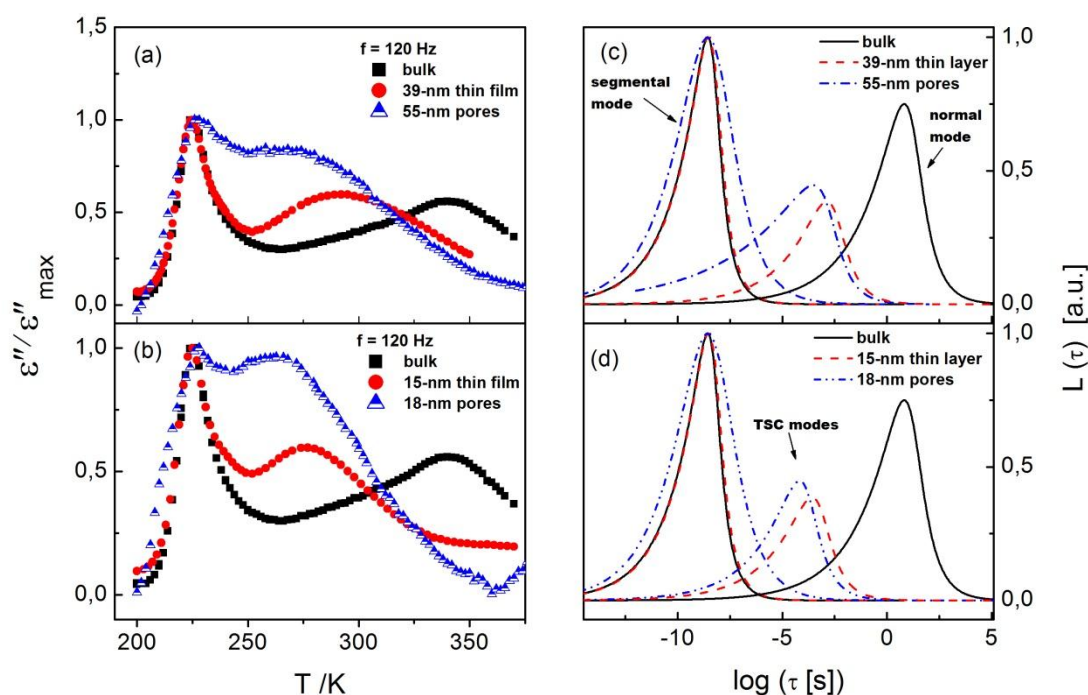


**Figure 4.28.** A comparison of PI loss data normalized w.r.t. the loss maximum of the segmental mode measured (at 120 Hz) in pores and in thin layers of comparable size (to the pore-diameter) as indicated in (a) and (b). Bulk data is included as well for completeness. Panels (c) and (d) show the respective distribution functions of the relaxation times at  $T = 316$  K.

In order to make a straightforward comparison between the effects of 1- and 2-D confinement, data for PI films and pores (with pore-diameters) of nearly equal size was plotted.

Figure 4.28 shows such data from which it is clear that (i) the mean spectral position of the segmental mode remains unchanged, when 1- and 2-D confined systems are compared to bulk data; (ii) the segmental mode is broadened in the AAO nanopore matrix, a phenomenon not observed for 1-D confinement; (iii) the fluctuation of the end-to-end vector of the chains is interrupted (since it is no longer bulk-like) in pores, just as in thin films, and becomes faster with reducing pore diameter (Fig. 4.27c). In addition, (iv) the broadening of the segmental mode is found to be pore-size dependent as shown in Figure 4.28c,d. It is important to note here that low-molecular weight (2, 7 and 11 kg/mol) *cis*-polyisoprene has been studied [254] in the controlled porous glass (CPG) Bioran and found too to exhibit a broadening (compared to bulk) of the segmental relaxation process.

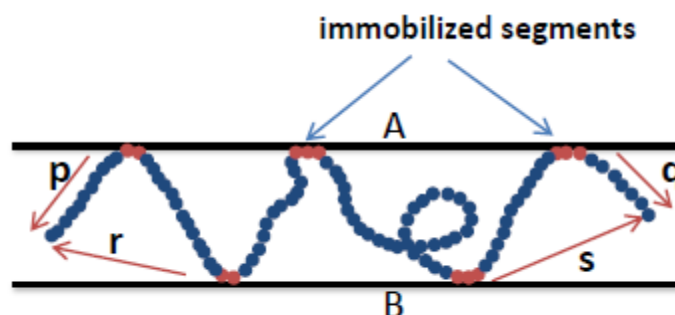


**Figure 4.29.** A schematic view of a chain (viewed in one plane inside a nanopore) constrained by the solid surfaces A and B. Segments of the chain in (attractive) interaction with the surfaces are adsorbed, and hence become immobilized. The tail ends (terminal subchains) are free to fluctuate with resultant vectors p and q or r and s in the presence or absence, respectively, of wall A.

The reason for the first observation (concerning the dynamic glass transition) is the same as already presented in the foregoing discussion. Fundamentally, the 2-D confining space  $\geq 18$  nm (i.e., the pore diameter) is still large enough to allow for uninterrupted fluctuation of sufficient basic units (2-3 segments) that underlie the (dynamic) glass transition. On the other hand, the broadening in the structural relaxation process, in pores as compared to thin films, is a consequence of the increase in the number of segments per unit volume that interact with the solid surface. This is because the surface area to volume ratio

increases by at least one order of magnitude from thin films to nanopores. A further reduction in the pore-diameter would increase the chain-surface interaction, and hence the pore-size dependent broadening as observed. The scheme in Figure 4.29 presents a possible explanation for why the TSC mode in nanopores is faster than that in a thin film of comparable size. For the pore system, taking a snap-shot view in one plane, the chain interacts with the two surfaces A and B so that the resultant terminal subchains have vectors  $\mathbf{p}$  and  $\mathbf{q}$ . If surface A is removed – producing a system equivalent to an uncapped thin film – the TSCs have vectors  $\mathbf{r}$  and  $\mathbf{s}$ , which are, intuitively, longer than  $\mathbf{p}$  and  $\mathbf{q}$ ; the fluctuation of the latter should therefore be faster.

#### 4.4.4 Summary

On the one hand, poly(*cis*-1,4-isoprene) being a *Type A* polymer, is an ideal candidate for studying both segmental and chain dynamics in confinement. The use of the nanostructured electrode arrangement, on the other hand, avails the experimental possibility of probing ultra-thin layers by BDS. It has been shown in this Chapter – for several molecular weights of PI lying in the range  $10 < M_w < 80$  kg/mol – that while the structural relaxation remains largely unaffected by changes in layer thickness (down to 7 nm), molecular weight and the polymer concentration in the spin-cast solution, the chain dynamics are drastically altered in dependence on these parameters. It has also been shown, courtesy of inaugural experiments, that chain dynamics in confinement depend on the dimensionality of the confining geometry. For a full understanding of this dependence, there is need for more experiments devoted to comparing 1-D with 2-D confining systems, as well as the corresponding molecular simulations.



## 5 Conclusions

---

In this work, the dielectric properties of atactic polystyrene (PS), itraconazole and poly(cis-1,4-isoprene) (PI) – under conditions of confinement – have been probed using Broadband Dielectric Spectroscopy (BDS) as the main experimental tool. Other techniques like Spectroscopic vis-Ellipsometry, chip AC Calorimetry and Differential Scanning Calorimetry, X-ray reflectometry and Atomic Force Microscopy have also been employed. For BDS, two sample geometries used for studying thin layers were substantively investigated. For all investigations, the sample size (thickness) was systematically scaled down to dimensions comparable to, or even less than, the radius of gyration of the respective molecule in bulk. The main findings can be summed up as follows:

- 1) The sample geometry applied in BDS studies has an influence on the measured dielectric response; precisely, the use of evaporated electrodes – which is the traditional and most common approach – introduces additional features to the complex permittivity, which show up mainly by broadening the dielectric loss peaks. The presence of metal oxides and immobilized layers at the polymer-solid interfaces partially account for this broadening.
- 2) The dynamic glass transition remains unchanged – in terms of the mean relaxation times – even when the system is confined in thin layers with thicknesses in the order of the radius of gyration of the corresponding molecule in bulk. This holds when the samples are annealed in high vacuum and measured in inert atmosphere.
- 3) While the structural relaxation remains bulk-like in confinement, independent of molecular weight, other molecular motions are considerably altered: a) for the case of LC itraconazole, the  $\delta$ -relaxation (flip-flop motions of the molecule about its short axis) become slowed down as the system is cooled towards glass formation; b) the fluctuation of the end-to-end vector, as exemplified by PI, is interrupted and can no longer be bulk-like. Instead, only the fluctuations of the free tails – called termi-

nal subchains in this report – can be sensed by BDS, and become faster with reducing layer thickness.

- 4) How molecules respond to confinement depends on the dimensionality of the confining space. By using a type A polymer (PI), and comparing 1- and 2-D confined cases, it has been demonstrated that, because of enhanced interactions with the walls, 2-D restrictions result in the broadening of the segmental peak and faster terminal subchains.
- 5) A hitherto overlooked parameter – the concentration of the mother solution – that influences dynamics in confinement has been unveiled. Usually, in thin film studies, the concentration of the starting solution is varied solely to adjust the film thickness. In this work, however, it has been shown that it matters whether the solution is dilute or semi-dilute.

## 5.1 Dynamics in confinement - a wider perspective

While the reasons for divergent results reported in literature concerning the (dynamic) glass transition in confinement remain the subject of debate and rigorous scientific investigations, there's an emerging trend in results which brings an explication of the same within reach. It is noteworthy that for techniques such as ellipsometry, fluorescence spectroscopy, thermal expansion spectroscopy, etc.,  $T_g$  is defined as the temperature where a first order thermodynamic property – or an associated quantity – exhibits a change in its temperature dependence, and often shows up as a kink in the observed trend. Fundamentally therefore, these methods avail information on how a glass former recovers or losses thermodynamic equilibrium upon heating or cooling, respectively. On the other hand, techniques such as Broadband Dielectric Spectroscopy and AC Calorimetry work in the linear regime, i.e., they probe the spontaneous fluctuations associated with the segmental (and other) relaxations usually at temperatures above the calorimetric  $T_g$ , and therefore actually study the glass-former in its (quasi)equilibrium liquid-like state.



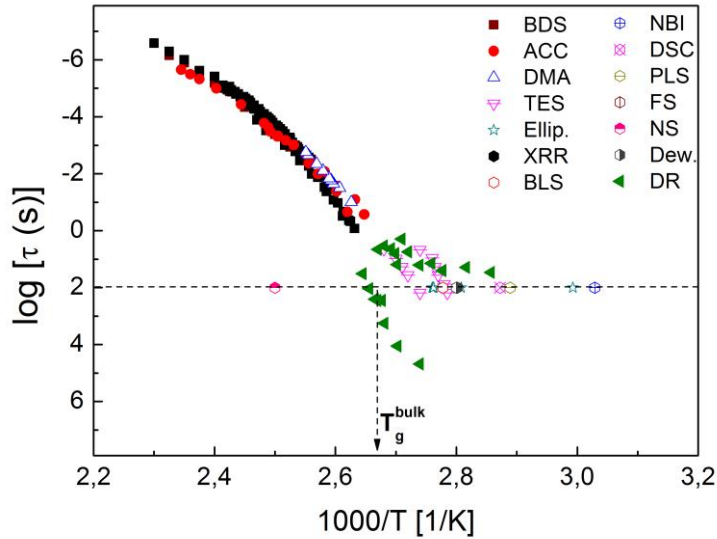


**Figure 5.1.** Relaxation times as a function of inverse temperature (extracted from literature) for supported polystyrene films with molecular weight in the range  $90\,000 < M_w < 1\,000\,000$  g/mol and thickness  $10 < d < 50$  nm as determined from various experimental techniques: Broadband Dielectric Spectroscopy (BDS) [70,91,131,137,144]; AC Calorimetry (ACC) [91,92]; Dynamic Mechanical Analysis (DMA) [115]; Thermal Expansion Spectroscopy (TES) [82]; Ellipsometry (Ellip.) [48,52,54,57,58,60]; X-Ray Reflectometry (XRR) [78]; Brillouin Light Scattering (BLS) [113]; Nano-Bubble Inflation (NBI) [120]; Differential Scanning Calorimetry (DSC) [52]; Positron Lifetime Spectroscopy (PLS) [90]; Fluorescence Spectroscopy (FS) [67]; Neutron Scattering (NS) [66]; Dewetting (Dew.) studies [126]; and (for freestanding PS layers) Dye Reorientation (DR) [104]. Data from techniques (e.g. DSC, Ellipsometry) where  $T_g$  is defined as the temperature at which a first order thermodynamic property (or an associated quantity) undergoes a change in its temperature-dependence is plotted assuming the convention  $T / \tau_{=100\text{ s}} = T_g$ .

This difference – together with the fact that it is unclear to what extent expansivity is coupled to dynamics [267] – makes it unsurprising when the two sets of techniques deliver discordant results. In Figure 5.1, an activation plot (data compiled from literature) for supported polystyrene (PS) layers (with molecular weight in the range  $90\,000 < M_w < 1\,000\,000$  g/mol and thickness  $10 < d < 50$  nm) as measured by a variety of experimental techniques is presented. PS is chosen for this illustration since it is the most studied system. It is noticeable that there's quantitative agreement between the results from Broad-

band Dielectric Spectroscopy, AC Calorimetry and dynamic mechanical analysis. On the other hand, results from Ellipsometry, differential scanning calorimetry etc. have a wide spread. These observations have been discussed in original [59,74,144,153] as well as review [268,269] expositions.

It has been argued that a dilatometric glass transition temperature (in thin films) does not necessarily signify a glass transition [270]. Starting from the idea of a so-called rheological temperature,  $T_R$ <sup>4</sup> [271] at the interface, Forrest and Dalnoki-Veress have shown that most of the  $T_g$  reductions reported from dilatometric measurements may be simply due to an enhanced surface mobility, and that the same does not imply a change in the dynamics of the whole film. Recently, Ediger and co-workers [104] – using segment-coupled dye-reorientation measurements – found two  $M_w$ -independent dynamical populations in the segmental dynamics of freestanding PS films (their data is included in Fig. 5.1 as well). Pye and Roth [272] also observed a two- $T_g$  phenomenon in freestanding high  $M_w$  PS films probed by transmission ellipsometry. The former group attributed the faster process to a mobile layer at the surface of the films, and the slow one to the interior. It has been suggested [269] that dielectric and dynamic heat capacity experiments, among others, do not report a distinct relaxation process consistent with a high surface mobility because of the temperature dependence of the mobile surface itself. This surface is said to be only apparent near and below the bulk  $T_g$ , and therefore observable exclusively at very low frequencies (or long time scales). While the nature of this surface layer demands further investigation, it is clear that close attention must now be paid to what exactly a given experimental technique probes.

---

<sup>4</sup>  $T_R$  is defined [270] as “the temperature the bulk system would have to be in order to have the same properties (relaxation time, modulus, etc.) as those measured for any portion of the system with the same thermal history.”

## References

- [1] J. Mattsson, J.A. Forrest, L. Börjesson, Quantifying glass transition behavior in ultrathin free-standing polymer films, *Phys. Rev. E.* 62 (2000) 5187.
- [2] K. Dalnoki-Veress, J. Forrest, C. Murray, C. Gigault, J. Dutcher, Molecular weight dependence of reductions in the glass transition temperature of thin, freely standing polymer films, *Phys. Rev. E.* 63 (2001) 031801. doi:10.1103/PhysRevE.63.031801.
- [3] J. Zarzycki, *Glasses and the vitreous state*, Cambridge University Press, Cambridge, 1991.
- [4] P. Debenedetti G., F. Stillinger H., Supercooled liquids and the glass transition, *Nature.* 410 (2001) 259–267.
- [5] C.A. Angell, K.L. Ngai, G.B. McKenna, P.F. McMillan, S.W. Martin, Relaxation in glassforming liquids and amorphous solids, *J. Appl. Phys.* 88 (2000) 3113–3157. doi:10.1063/1.1286035.
- [6] M.I. Ojovan, Glass formation in amorphous SiO<sub>2</sub> as a percolation phase transition in a system of network defects, *J. Exp. Theor. Phys. Lett.* 79 (2004) 632–634.
- [7] M.D. Ediger, C.A. Angell, S.R. Nagel, Supercooled liquids and glasses, *J. Phys. Chem.* 100 (1996) 13200–13212.
- [8] H. Vogel, *Phys. Z.* 22 (1921) 645–646.
- [9] G. Fulcher S., Analysis of recent measurements of the viscosity of glasses, *J. Am. Ceram. Soc.* 8 (1925) 339–355.
- [10] G. Tammann, G. Hesse, Die Abhängigkeit der Viskosität von der Temperatur bei Unterkühlten Flüssigkeiten, *Z. Für Anorg. Allg. Chem.* 156 (1926) 245–257.
- [11] W. Kauzmann, The nature of the glassy state and the behavior of liquids at low temperatures., *Chem. Rev.* 43 (1948) 219–256.
- [12] F. Kremer, A. Schönhals, eds., *Broadband Dielectric Spectroscopy*, Springer-Verlag, Berlin, 2003.
- [13] C.A. Angell, Formation of glasses from liquids and biopolymers, *Science.* 267 (1995) 1924–1935.
- [14] F. Stickel, E.W. Fischer, R. Richert, Dynamics of glass-forming liquids. I. Temperature-derivative analysis of dielectric relaxation data, *J. Chem. Phys.* 102 (1995) 6251–6257. doi:10.1063/1.469071.
- [15] G. Williams, D.C. Watts, Non-symmetrical dielectric relaxation behaviour arising from a simple empirical decay function, *Trans. Faraday Soc.* 66 (1970) 80–85. doi:10.1039/TF9706600080.
- [16] R. Richert, Homogeneous dispersion of dielectric responses in a simple gas, *J. Non-Cryst. Solids.* 172-174 (1994) 209–213.
- [17] D. Turnbull, M.H. Cohen, Concerning reconstructive transformation and formation of glass, *J. Chem. Phys.* 29 (1958) 1049–1054. doi:10.1063/1.1744654.
- [18] T.G. Fox, P.J. Flory, Second-order transition temperatures and related properties of polystyrene. I. Influence of molecular weight, *J. Appl. Phys.* 21 (1950) 581–591. doi:10.1063/1.1699711.
- [19] T.G. Fox Jr, P.J. Flory, Further studies on the melt viscosity of polyisobutylene., *J. Phys. Chem.* 55 (1951) 221–234.
- [20] T.G. Fox, P.J. Flory, The glass temperature and related properties of polystyrene. Influence of molecular weight, *J. Polym. Sci.* 14 (1954) 315–319.

- [21] A.K. Doolittle, Studies in Newtonian flow. II. The dependence of the viscosity of liquids on free-space, *J. Appl. Phys.* 22 (1951) 1471–1475. doi:10.1063/1.1699894.
- [22] M.H. Cohen, G.S. Grest, Liquid-glass transition, a free-volume approach, *Phys. Rev. B.* 20 (1979) 1077–1098.
- [23] M.H. Cohen, D. Turnbull, Molecular transport in liquids and glasses, *J. Chem. Phys.* 31 (1959) 1164–1169. doi:10.1063/1.1730566.
- [24] G. Tarjus, D. Kivelson, Breakdown of the Stokes–Einstein relation in supercooled liquids, *J. Chem. Phys.* 103 (1995) 3071–3073. doi:10.1063/1.470495.
- [25] D. Champion, H. Hervet, G. Blond, M.L. Meste, D. Simatos, Translational diffusion in sucrose solutions in the vicinity of their glass transition temperature, *J. Phys. Chem. B.* 101 (1997) 10674–10679.
- [26] S.C. Glotzer, V.N. Novikov, T.B. Schröder, Time-dependent, four-point density correlation function description of dynamical heterogeneity and decoupling in supercooled liquids, *J. Chem. Phys.* 112 (2000) 509–512. doi:10.1063/1.480541.
- [27] S.M. Anthony, M. Kim, S. Granick, Translation-rotation decoupling of colloidal clusters of various symmetries, *J. Chem. Phys.* 129 (2008) 244701–244706. doi:10.1063/1.3043443.
- [28] K.V. Edmond, M.T. Elsesser, G.L. Hunter, D.J. Pine, E.R. Weeks, Decoupling of rotational and translational diffusion in supercooled colloidal fluids, *Proc. Natl. Acad. Sci.* 109 (2012) 17891–17896. doi:10.1073/pnas.1203328109.
- [29] G. Tarjus, An overview of the theories of the glass transition, *Dyn. Heterog. Glas. Colloids Granul. Media.* 150 (2011) 1–28.
- [30] G. Adam, J.H. Gibbs, On the temperature dependence of cooperative relaxation properties in glass-forming liquids, *J. Chem. Phys.* 43 (1965) 139–146.
- [31] C.A. Angell, Structural instability and relaxation in liquid and glassy phases near the fragile liquid limit, *J. Non-Cryst. Solids.* 102 (1988) 205–221.
- [32] E. Donth, H. Huth, M. Beiner, Characteristic length of the glass transition, *J. Phys. Condens. Matter.* 13 (2001) L451–L462.
- [33] F. Kremer, A. Huwe, M. Arndt, P. Behrens, W. Schwieger, How many molecules form a liquid?, *J. Phys. Condens. Matter.* 11 (1999) A175–A188.
- [34] E. Hempel, G. Hempel, A. Hensel, C. Schick, E. Donth, Characteristic length of dynamic glass transition near  $T_g$  for a wide assortment of glass-forming substances, *J. Phys. Chem. B.* 104 (2000) 2460–2466. doi:10.1021/jp991153f.
- [35] S.A. Reinsberg, X.H. Qiu, M. Wilhelm, H.W. Spiess, M.D. Ediger, Length scale of dynamic heterogeneity in supercooled glycerol near  $T_g$ , *J. Chem. Phys.* 114 (2001) 7299–7302. doi:10.1063/1.1369160.
- [36] M. Wübbenhorst, C.A. Murray, J.A. Forrest, J.R. Dutcher, Dielectric relaxations in ultra-thin films of PMMA: Assessing the length scale of cooperativity in the dynamic glass transition, in: *Electrets 2002 ISE 11 Proc. 11th Int. Symp. On, 2002*: pp. 401–406. [http://ieeexplore.ieee.org/xpls/abs\\_all.jsp?arnumber=1043027](http://ieeexplore.ieee.org/xpls/abs_all.jsp?arnumber=1043027) (accessed July 30, 2013).
- [37] C. Donati, J.F. Douglas, W. Kob, S.J. Plimpton, P.H. Poole, S.C. Glotzer, Stringlike cooperative motion in a supercooled liquid, *Phys. Rev. Lett.* 80 (1998) 2338–2341.
- [38] J.R. Dutcher, A.G. Marangoni, eds., *Soft Materials: Structure and Dynamics*, Marcel Dekker, New York, 2005.

- [39] U. Bengtzelius, W. Gotze, A. Sjolander, Dynamics of supercooled liquids and the glass transition, *J. Phys. C Solid State Phys.* 17 (1984) 5915–5934.
- [40] E. Leutheusser, Dynamical model of the liquid-glass transition, *Phys. Rev. A.* 29 (1984) 2765–2773.
- [41] K. Kawasaki, Correlation-function approach to the transport coefficients near the critical point., *Phys. Rev.* 150 (1966) 291–306.
- [42] W. Götze, L. Sjogren, Relaxation processes in supercooled liquids, *Rep. Prog. Phys.* 55 (1992) 241–376.
- [43] D.R. Reichman, P. Charbonneau, Mode-coupling theory, *J. Stat. Mech. Theory Exp.* 2005 (2005) P05013–P05036. doi:10.1088/1742-5468/2005/05/P05013.
- [44] A. Wischnewski, D. Richter, Polymer dynamics in melts, in: G. Gompper, M. Schick (Eds.), *Soft Matter*, Wiley-VCH, Weinheim, 2006: pp. 17–85.
- [45] G.R. Strobl, *The Physics of Polymers: Concepts for Understanding their Structures and Behavior*, 3rd ed., Springer, Berlin Heidelberg New York, 2007.
- [46] P.G. de Gennes, Reptation of a polymer chain in the presence of fixed obstacles, *J. Chem. Phys.* 55 (1971) 572. doi:10.1063/1.1675789.
- [47] D. Boese, F. Kremer, Molecular dynamics in bulk cis-polyisoprene as studied by dielectric spectroscopy, *Macromolecules.* 23 (1990) 829–835.
- [48] J.L. Keddie, R.A.L. Jones, R.A. Cory, Size-dependent depression of the glass transition temperature in polymer films, *Europhys. Lett.* 27 (1994) 59–64.
- [49] J.L. Keddie, R.A.L. Jones, R.A. Cory, Interface and surface effects on the glass-transition temperature in thin polymer films, *Faraday Discuss.* 98 (1994) 219–230.
- [50] J.A. Forrest, K. Dalnoki-Veress, J.R. Dutcher, Interface and chain confinement effects on the glass transition temperature of thin polymer films, *Phys. Rev. E.* 56 (1997) 5705–5716.
- [51] Y. Grohens, M. Brogly, C. Labbe, M.-O. David, J. Schultz, Glass transition of stereoregular poly (methyl methacrylate) at interfaces, *Langmuir.* 14 (1998) 2929–2932.
- [52] D.S. Fryer, P.F. Nealey, J.J. de Pablo, Thermal probe measurements of the glass transition temperature for ultrathin polymer films as a function of thickness, *Macromolecules.* 33 (2000) 6439–6447. doi:10.1021/ma0003349.
- [53] D.S. Fryer, R.D. Peters, E.J. Kim, J.E. Tomaszewski, J.J. de Pablo, P.F. Nealey, et al., Dependence of the glass transition temperature of polymer films on interfacial energy and thickness, *Macromolecules.* 34 (2001) 5627–5634. doi:10.1021/ma001932q.
- [54] S. Kawana, R. Jones, Character of the glass transition in thin supported polymer films, *Phys. Rev. E.* 63 (2001) 021501. doi:10.1103/PhysRevE.63.021501.
- [55] O.K.C. Tsui, H.F. Zhang, Effects of chain ends and chain entanglement on the glass transition temperature of polymer thin films, *Macromolecules.* 34 (2001) 9139–9142. doi:10.1021/ma0102159.
- [56] Y. Grohens, L. Hamon, G. Reiter, A. Soldera, Y. Holl, Some relevant parameters affecting the glass transition of supported ultra-thin polymer films, *Eur. Phys. J. E - Soft Matter.* 8 (2002) 217–224. doi:10.1140/epje/i2001-10088-4.
- [57] F. Xie, H.F. Zhang, F.K. Lee, B. Du, O.K.C. Tsui, Y. Yokoe, et al., Effect of low surface energy chain ends on the glass transition temperature of polymer thin films, *Macromolecules.* 35 (2002) 1491–1492. doi:10.1021/ma011689a.

- [58] J. Sharp, J. Forrest, Free surfaces cause reductions in the glass transition temperature of thin polystyrene films, *Phys. Rev. Lett.* 91 (2003) 235701. doi:10.1103/PhysRevLett.91.235701.
- [59] J. Sharp, J. Forrest, Dielectric and ellipsometric studies of the dynamics in thin films of isotactic poly(methylmethacrylate) with one free surface, *Phys. Rev. E* 67 (2003) 031805. doi:10.1103/PhysRevE.67.031805.
- [60] J. D'Amour, Influence of substrate chemistry on the properties of ultrathin polymer films, *Microelectron. Eng.* 73-74 (2004) 209–217. doi:10.1016/j.mee.2004.02.042.
- [61] Z. Fakhraai, J.S. Sharp, J.A. Forrest, Effect of sample preparation on the glass-transition of thin polystyrene films, *J. Polym. Sci. Part B Polym. Phys.* 42 (2004) 4503–4507. doi:10.1002/polb.20281.
- [62] L. Singh, P.J. Ludovice, C.L. Henderson, Influence of molecular weight and film thickness on the glass transition temperature and coefficient of thermal expansion of supported ultrathin polymer films, *Thin Solid Films*. 449 (2004) 231–241. doi:10.1016/S0040-6090(03)01353-1.
- [63] Z. Fakhraai, J. Forrest, Probing slow dynamics in supported thin polymer films, *Phys. Rev. Lett.* 95 (2005) 025701. doi:10.1103/PhysRevLett.95.025701.
- [64] C.B. Roth, A. Pound, S.W. Kamp, C.A. Murray, J.R. Dutcher, Molecular-weight dependence of the glass transition temperature of freely-standing poly(methyl methacrylate) films, *Eur. Phys. J. E* 20 (2006) 441–448. doi:10.1140/epje/i2006-10034-0.
- [65] A.N. Raegen, M.V. Massa, J.A. Forrest, K. Dalnoki-Veress, Effect of atmosphere on reductions in the glass transition of thin polystyrene films, *Eur. Phys. J. E* 27 (2008) 375–377. doi:10.1140/epje/i2008-10394-3.
- [66] R. Inoue, T. Kanaya, K. Nishida, I. Tsukushi, M. Telling, B. Gabrys, et al., Glass transition and molecular mobility in polymer thin films, *Phys. Rev. E* 80 (2009) 031802. doi:10.1103/PhysRevE.80.031802.
- [67] S. Kim, S.A. Hewlett, C.B. Roth, J.M. Torkelson, Confinement effects on glass transition temperature, transition breadth, and expansivity: Comparison of ellipsometry and fluorescence measurements on polystyrene films, *Eur. Phys. J. E* 30 (2009) 83–92. doi:10.1140/epje/i2009-10510-y.
- [68] H. Lu, W. Chen, T.P. Russell, Relaxation of thin films of polystyrene floating on ionic liquid surface, *Macromolecules*. 42 (2009) 9111–9117. doi:10.1021/ma901789k.
- [69] E.U. Mapesa, M. Erber, M. Tress, K.-J. Eichhorn, A. Serghei, B. Voit, et al., Glassy dynamics in nanometer thin layers of polystyrene, *Eur. Phys. J. Spec. Top.* 189 (2010) 173–180. doi:10.1140/epjst/e2010-01320-2.
- [70] M. Tress, M. Erber, E.U. Mapesa, H. Huth, J. Müller, A. Serghei, et al., Glassy dynamics and glass transition in nanometric thin layers of polystyrene, *Macromolecules*. 43 (2010) 9937–9944. doi:10.1021/ma102031k.
- [71] M. Erber, M. Tress, E.U. Mapesa, A. Serghei, K.-J. Eichhorn, B. Voit, et al., Glassy dynamics and glass transition in thin polymer layers of PMMA deposited on different substrates, *Macromolecules*. 43 (2010) 7729–7733. doi:10.1021/ma100912r.
- [72] A. Clough, D. Peng, Z. Yang, O.K.C. Tsui, Glass transition temperature of polymer films that slip, *Macromolecules*. 44 (2011) 1649–1653. doi:10.1021/ma102918s.

- [73] E. Glynos, B. Frieberg, H. Oh, M. Liu, D.W. Gidley, P.F. Green, Role of molecular architecture on the vitrification of polymer thin films, *Phys. Rev. Lett.* 106 (2011) 128301. doi:10.1103/PhysRevLett.106.128301.
- [74] O. Bäumchen, J.D. McGraw, J.A. Forrest, K. Dalnoki-Veress, Reduced glass transition temperatures in thin polymer films: surface effect or artifact?, *Phys. Rev. Lett.* 109 (2012) 055701. doi:10.1103/PhysRevLett.109.055701.
- [75] G. Reiter, Dewetting as a probe of polymer mobility in thin films, *Macromolecules.* 27 (1994) 3046–3052.
- [76] W.E. Wallace, J.H. Van Zanten, W.L. Wu, Influence of an impenetrable interface on a polymer glass-transition temperature, *Phys. Rev. E.* 52 (1995) R3329–R3332.
- [77] O.K.C. Tsui, T.P. Russell, C.J. Hawker, Effect of Interfacial Interactions on the Glass Transition of Polymer Thin Films, *Macromolecules.* 34 (2001) 5535–5539. doi:10.1021/ma000028v.
- [78] R. Inoue, T. Kanaya, T. Miyazaki, K. Nishida, I. Tsukushi, K. Shibata, Glass transition and thermal expansivity of polystyrene thin films, *Mater. Sci. Eng. A.* 442 (2006) 367–370. doi:10.1016/j.msea.2006.01.143.
- [79] T. Miyazaki, R. Inoue, K. Nishida, T. Kanaya, X-ray reflectivity studies on glass transition of free standing polystyrene thin films, *Eur. Phys. J. Spec. Top.* 141 (2007) 203–206. doi:10.1140/epjst/e2007-00041-y.
- [80] T. Kanaya, R. Inoue, K. Kawashima, T. Miyazaki, I. Tsukushi, K. Shibata, et al., Glassy dynamics and heterogeneity of polymer thin films, *J. Phys. Soc. Jpn.* 78 (2009) 041004. doi:10.1143/JPSJ.78.041004.
- [81] R.S. Tate, D.S. Fryer, S. Pasqualini, M.F. Montague, J.J. de Pablo, P.F. Nealey, Extraordinary elevation of the glass transition temperature of thin polymer films grafted to silicon oxide substrates, *J. Chem. Phys.* 115 (2001) 9982. doi:10.1063/1.1415497.
- [82] K. Fukao, Y. Miyamoto, Slow dynamics near glass transitions in thin polymer films, *Phys. Rev. E.* 64 (2001) 011803. doi:10.1103/PhysRevE.64.011803.
- [83] M.Y. Efremov, E. Olson, M. Zhang, Z. Zhang, L. Allen, Glass transition in ultrathin polymer films: calorimetric study, *Phys. Rev. Lett.* 91 (2003) 085703. doi:10.1103/PhysRevLett.91.085703.
- [84] M.Y. Efremov, E.A. Olson, M. Zhang, Z. Zhang, L.H. Allen, Probing glass transition of ultrathin polymer films at a time scale of seconds using fast differential scanning calorimetry, *Macromolecules.* 37 (2004) 4607–4616. doi:10.1021/ma035909r.
- [85] Y.P. Koh, G.B. McKenna, S.L. Simon, Calorimetric glass transition temperature and absolute heat capacity of polystyrene ultrathin films, *J. Polym. Sci. Part B Polym. Phys.* 44 (2006) 3518–3527. doi:10.1002/polb.21021.
- [86] Y.P. Koh, S.L. Simon, Structural relaxation of stacked ultrathin polystyrene films, *J. Polym. Sci. Part B Polym. Phys.* 46 (2008) 2741–2753. doi:10.1002/polb.21598.
- [87] P. Bernazzani, R.F. Sanchez, Structural and thermal behavior of polystyrene thin films using ATR–FTIR–NanoDSC measurements, *J. Therm. Anal. Calorim.* 96 (2009) 727–732. doi:10.1007/s10973-009-0033-4.
- [88] K. Fukao, T. Terasawa, Y. Oda, K. Nakamura, D. Tahara, Glass transition dynamics of stacked thin polymer films, *Phys. Rev. E.* 84 (2011) 041808. doi:10.1103/PhysRevE.84.041808.

- [89] G.B. DeMaggio, W.E. Frieze, D.W. Gidley, M. Zhu, H.A. Hristov, A.F. Yee, Interface and surface effects on the glass transition in thin polystyrene films, *Phys. Rev. Lett.* 78 (1997) 1524–1527.
- [90] Y.C. Jean, R. Zhang, H. Cao, J.-P. Yuan, C.-M. Huang, B. Nielsen, et al., Glass transition of polystyrene near the surface studied by slow-positron-annihilation spectroscopy, *Phys. Rev. B.* 56 (1997) R8459.
- [91] V. Lupășcu, H. Huth, C. Schick, M. Wübbenhorst, Specific heat and dielectric relaxations in ultra-thin polystyrene layers, *Thermochim. Acta.* 432 (2005) 222–228. doi:10.1016/j.tca.2005.04.022.
- [92] H. Huth, A.A. Minakov, C. Schick, Differential AC-chip calorimeter for glass transition measurements in ultrathin films, *J. Polym. Sci. Part B Polym. Phys.* 44 (2006) 2996–3005. doi:10.1002/polb.20921.
- [93] H. Huth, A.A. Minakov, A. Serghei, F. Kremer, C. Schick, Differential AC-chip calorimeter for glass transition measurements in ultra thin polymeric films, *Eur. Phys. J. Spec. Top.* 141 (2007) 153–160. doi:10.1140/epjst/e2007-00033-y.
- [94] C. Schick, Glass transition under confinement-what can be learned from calorimetry, *Eur. Phys. J. Spec. Top.* 189 (2010) 3–36. doi:10.1140/epjst/e2010-01307-y.
- [95] C.J. Ellison, J.M. Torkelson, Sensing the glass transition in thin and ultrathin polymer films via fluorescence probes and labels, *J. Polym. Sci. Part B Polym. Phys.* 40 (2002) 2745–2758. doi:10.1002/polb.10343.
- [96] C.J. Ellison, S.D. Kim, D.B. Hall, J.M. Torkelson, Confinement and processing effects on glass transition temperature and physical aging in ultrathin polymer films: Novel fluorescence measurements, *Eur. Phys. J. E - Soft Matter.* 8 (2002) 155–166. doi:10.1140/epje/i2001-10057-y.
- [97] C.J. Ellison, J.M. Torkelson, The distribution of glass-transition temperatures in nanoscopically confined glass formers, *Nat. Mater.* 2 (2003) 695–700. doi:10.1038/nmat980.
- [98] C. Ellison, R. Ruszkowski, N. Fredin, J. Torkelson, Dramatic reduction of the effect of nanoconfinement on the glass transition of polymer films via addition of small-molecule diluent, *Phys. Rev. Lett.* 92 (2004) 095702. doi:10.1103/PhysRevLett.92.095702.
- [99] C.J. Ellison, M.K. Mundra, J.M. Torkelson, Impacts of polystyrene molecular weight and modification to the repeat unit structure on the glass transition–nanoconfinement effect and the cooperativity length scale, *Macromolecules.* 38 (2005) 1767–1778. doi:10.1021/ma047846y.
- [100] M.K. Mundra, C.J. Ellison, R.E. Behling, J.M. Torkelson, Confinement, composition, and spin-coating effects on the glass transition and stress relaxation of thin films of polystyrene and styrene-containing random copolymers: Sensing by intrinsic fluorescence, *Polymer.* 47 (2006) 7747–7759. doi:10.1016/j.polymer.2006.08.064.
- [101] M.K. Mundra, C.J. Ellison, P. Rittigstein, J.M. Torkelson, Fluorescence studies of confinement in polymer films and nanocomposites: Glass transition temperature, plasticizer effects, and sensitivity to stress relaxation and local polarity, *Eur. Phys. J. Spec. Top.* 141 (2007) 143–151. doi:10.1140/epjst/e2007-00032-0.
- [102] S. Kim, C.B. Roth, J.M. Torkelson, Effect of nanoscale confinement on the glass transition temperature of free-standing polymer films: Novel, self-referencing fluo-



- rescence method, *J. Polym. Sci. Part B Polym. Phys.* 46 (2008) 2754–2764. doi:10.1002/polb.21591.
- [103] S. Kim, J.M. Torkelson, Distribution of glass transition temperatures in free-standing, nanoconfined polystyrene films: Atest of de Gennes' sliding motion mechanism, *Macromolecules*. 44 (2011) 4546–4553. doi:10.1021/ma200617j.
- [104] K. Paeng, S.F. Swallen, M.D. Ediger, Direct measurement of molecular motion in freestanding polystyrene thin films, *J. Am. Chem. Soc.* 133 (2011) 8444–8447. doi:10.1021/ja2022834.
- [105] K. Paeng, M.D. Ediger, Molecular motion in free-standing thin films of poly(methyl methacrylate), poly(4-*tert*-butylstyrene), poly( $\alpha$ -methylstyrene), and poly(2-vinylpyridine), *Macromolecules*. 44 (2011) 7034–7042. doi:10.1021/ma201266r.
- [106] K. Paeng, H.-N. Lee, S.F. Swallen, M.D. Ediger, Temperature-ramping measurement of dye reorientation to probe molecular motion in polymer glasses, *J. Chem. Phys.* 134 (2011) 024901.
- [107] K. Paeng, R. Richert, M.D. Ediger, Molecular mobility in supported thin films of polystyrene, poly(methyl methacrylate), and poly(2-vinyl pyridine) probed by dye reorientation, *Soft Matter*. 8 (2012) 819–826. doi:10.1039/c1sm06501g.
- [108] T. Kanaya, T. Miyazaki, H. Watanabe, K. Nishida, H. Yamano, S. Tasaki, et al., Annealing effects on thickness of polystyrene thin films as studied by neutron reflectivity, *Polymer*. 44 (2003) 3769–3773. doi:10.1016/S0032-3861(03)00309-4.
- [109] R. Inoue, K. Kawashima, K. Matsui, T. Kanaya, K. Nishida, G. Matsuba, et al., Distributions of glass-transition temperature and thermal expansivity in multilayered polystyrene thin films studied by neutron reflectivity, *Phys. Rev. E*. 83 (2011) 021801. doi:10.1103/PhysRevE.83.021801.
- [110] R. Inoue, K. Kawashima, K. Matsui, M. Nakamura, K. Nishida, T. Kanaya, et al., Interfacial properties of polystyrene thin films as revealed by neutron reflectivity, *Phys. Rev. E*. 84 (2011) 031802. doi:10.1103/PhysRevE.84.031802.
- [111] J.A. Forrest, K. Dalnoki-Veress, J.R. Stevens, J.R. Dutcher, Effect of free surfaces on the glass transition temperature of thin polymer films, *Phys. Rev. Lett.* 77 (1996) 2002–2005.
- [112] J.A. Forrest, J. Mattsson, Reductions of the glass transition temperature in thin polymer films: probing the length scale of cooperative dynamics, *Phys. Rev. E*. 61 (2000) R53–R56.
- [113] W. Cheng, R. Sainidou, P. Burgardt, N. Stefanou, A. Kiyanova, M. Efremov, et al., Elastic properties and glass transition of supported polymer thin films, *Macromolecules*. 40 (2007) 7283–7290. doi:10.1021/ma071227i.
- [114] K. Akabori, K. Tanaka, T. Kajiyama, A. Takahara, Anomalous surface relaxation process in polystyrene ultrathin films, *Macromolecules*. 36 (2003) 4937–4943. doi:10.1021/ma034001y.
- [115] K. Akabori, K. Tanaka, T. Nagamura, A. Takahara, T. Kajiyama, Molecular motion in ultrathin polystyrene films: dynamic mechanical analysis of surface and interfacial effects, *Macromolecules*. 38 (2005) 9735–9741. doi:10.1021/ma051143e.
- [116] K.-I. Akabori, K. Tanaka, A. Takahara, T. Kajiyama, T. Nagamura, Substrate effect on mechanical relaxation of polystyrene in ultrathin films, *Eur. Phys. J. Spec. Top.* 141 (2007) 173–180. doi:10.1140/epjst/e2007-00036-8.

- [117] S. Ge, Y. Pu, W. Zhang, M. Rafailovich, J. Sokolov, C. Buenviaje, et al., Shear modulation force microscopy study of near surface glass transition temperatures, *Phys. Rev. Lett.* 85 (2000) 2340–2343.
- [118] F. Dinelli, A. Ricci, T. Sgrilli, P. Baschieri, P. Pingue, M. Puttaswamy, et al., Nanoscale viscoelastic behavior of the surface of thick polystyrene films as a function of temperature, *Macromolecules.* 44 (2011) 987–992. doi:10.1021/ma200007d.
- [119] P.A. O’Connell, G.B. McKenna, Rheological measurements of the thermoviscoelastic response of ultrathin polymer films, *Science.* 307 (2005) 1760–1763. doi:10.1126/science.1105658.
- [120] P.A. O’Connell, G.B. McKenna, Dramatic stiffening of ultrathin polymer films in the rubbery regime, *Eur. Phys. J. E.* 20 (2006) 143–150. doi:10.1140/epje/i2005-10125-4.
- [121] P.A. O’Connell, G.B. McKenna, Novel nanobubble inflation method for determining the viscoelastic properties of ultrathin polymer films, *Rev. Sci. Instrum.* 78 (2007) 013901. doi:10.1063/1.2409777.
- [122] P.A. O’Connell, S.A. Hutcheson, G.B. McKenna, Creep behavior of ultra-thin polymer films, *J. Polym. Sci. Part B Polym. Phys.* 46 (2008) 1952–1965. doi:10.1002/polb.21531.
- [123] P.A. O’Connell, G.B. McKenna, A novel nano-bubble inflation method for determining the viscoelastic properties of ultrathin polymer films, *Scanning.* 30 (2008) 184–196.
- [124] H. Bodiguel, C. Fretigny, Viscoelastic properties of ultrathin polystyrene films, *Macromolecules.* 40 (2007) 7291–7298. doi:10.1021/ma070460d.
- [125] Z. Yang, D. Peng, A. Clough, C.-H. Lam, O.K.C. Tsui, Is the dynamics of polystyrene films consistent with their glass transition temperature?, *Eur. Phys. J. Spec. Top.* 189 (2010) 155–164. doi:10.1140/epjst/e2010-01318-8.
- [126] J. Wang, G.B. McKenna, Viscoelastic and glass transition properties of ultrathin polystyrene films by dewetting from liquid glycerol, *Macromolecules.* 46 (2013) 2485–2495. doi:10.1021/ma400040j.
- [127] O. Prucker, S. Christian, H. Bock, J. Ruhe, W.C. Frank, W. Knoll, On the glass transition in ultrathin polymer films of different molecular architecture, *Macromol. Chem. Phys.* 199 (1998) 1435–1444.
- [128] K. Fukao, Y. Miyamoto, Glass transition temperature and dynamics of  $\alpha$ -process in thin polymer films, *Europhys. Lett.* 46 (1999) 649–654.
- [129] K. Fukao, Y. Miyamoto, Glass transitions and dynamics in thin polymer films: dielectric relaxation of thin films of polystyrene, *Phys. Rev. E.* 61 (2000) 1743–1754.
- [130] K. Fukao, S. Uno, Y. Miyamoto, A. Hoshino, H. Miyaji, Relaxation dynamics in thin supported polymer films, *J. Non-Cryst. Solids.* 307-310 (2002) 517–523.
- [131] A. Serghei, H. Huth, M. Schellenberger, C. Schick, F. Kremer, Pattern formation in thin polystyrene films induced by an enhanced mobility in ambient air, *Phys. Rev. E.* 71 (2005) 061801. doi:10.1103/PhysRevE.71.061801.
- [132] V. Lupaşcu, S.J. Picken, M. Wubbenhorst, Cooperative and non-cooperative dynamics in ultra-thin films of polystyrene studied by dielectric spectroscopy and capacitive dilatometry, *J. Non-Cryst. Solids.* 352 (2006) 5594–5600. doi:10.1016/j.jnoncrysol.2006.09.004.

- [133] A. Serghei, F. Kremer, Unexpected preparative effects on the properties of thin polymer films, *Prog. Colloid Polym. Sci.* 132 (2006) 33–40. doi:10.1007/2882\_038.
- [134] S. Napolitano, M. Wübbenhorst, Dielectric signature of a dead layer in ultrathin films of a nonpolar polymer, *J. Phys. Chem. B.* 111 (2007) 9197–9199. doi:10.1021/jp072868i.
- [135] R. Priestley, L. Broadbelt, J. Torkelson, K. Fukao, Glass transition and  $\alpha$ -relaxation dynamics of thin films of labeled polystyrene, *Phys. Rev. E.* 75 (2007) 061806. doi:10.1103/PhysRevE.75.061806.
- [136] C. Svanberg, Glass transition relaxations in thin suspended polymer films, *Macromolecules.* 40 (2007) 312–315. doi:10.1021/ma061967b.
- [137] A. Serghei, H. Huth, C. Schick, F. Kremer, Glassy dynamics in thin polymer layers having a free upper interface, *Macromolecules.* 41 (2008) 3636–3639. doi:10.1021/ma702381t.
- [138] A. Serghei, F. Kremer, Metastable states of glassy dynamics, possibly mimicking confinement-effects in thin polymer films, *Macromol. Chem. Phys.* 209 (2008) 810–817. doi:10.1002/macp.200700534.
- [139] C. Rotella, S. Napolitano, M. Wübbenhorst, Segmental mobility and glass transition temperature of freely suspended ultrathin polymer membranes, *Macromolecules.* 42 (2009) 1415–1417. doi:10.1021/ma8027968.
- [140] S. Napolitano, M. Wübbenhorst, Structural relaxation and dynamic fragility of freely standing polymer films, *Polymer.* 51 (2010) 5309–5312. doi:10.1016/j.polymer.2010.09.060.
- [141] C. Rotella, S. Napolitano, L. De Cremer, G. Koeckelberghs, M. Wübbenhorst, Distribution of segmental mobility in ultrathin polymer films, *Macromolecules.* 43 (2010) 8686–8691. doi:10.1021/ma101695y.
- [142] S. Napolitano, C. Rotella, M. Wübbenhorst, Is the reduction in tracer diffusivity under nanoscopic confinement related to a frustrated segmental mobility?, *Macromol. Rapid Commun.* 32 (2011) 844–848. doi:10.1002/marc.201100029.
- [143] S. Napolitano, M. Wübbenhorst, The lifetime of the deviations from bulk behaviour in polymers confined at the nanoscale, *Nat. Commun.* 2 (2011) 260–267. doi:10.1038/ncomms1259.
- [144] V.M. Boucher, D. Cangialosi, H. Yin, A. Schönhals, A. Alegría, J. Colmenero, Tg depression and invariant segmental dynamics in polystyrene thin films, *Soft Matter.* 8 (2012) 5119–5122. doi:10.1039/c2sm25419k.
- [145] F. Kremer, L. Hartmann, A. Serghei, P. Pouret, L. Leger, Molecular dynamics in thin grafted and spin-coated polymer layers, *Eur. Phys. J. E - Soft Matter.* 12 (2003) 139–142. doi:10.1140/epje/i2003-10053-3.
- [146] E.U. Mapesa, M. Tress, G. Schulz, H. Huth, C. Schick, M. Reiche, et al., Segmental and chain dynamics in nanometric layers of poly(cis-1,4-isoprene) as studied by broadband dielectric spectroscopy and temperature-modulated calorimetry, *Soft Matter.* 9 (2013) 10592. doi:10.1039/c3sm51311d.
- [147] M. Tress, E.U. Mapesa, W. Kossack, W.K. Kipnusu, M. Reiche, F. Kremer, Glassy dynamics in condensed isolated polymer coils, *Science.* 341 (2013) 1371–1374. doi:10.1126/science.123850.
- [148] K. Fukao, Dynamics in thin polymer films by dielectric spectroscopy, *Eur. Phys. J. E - Soft Matter.* 12 (2003) 119–125. doi:10.1140/epje/i2003-10030-x.

- [149] F.E. Karasz, W.J. MacKnight, The influence of stereoregularity on the glass transition temperatures of vinyl polymers, *Macromolecules*. 1 (1968) 537–540.
- [150] H.K. Nguyen, M. Labardi, S. Capaccioli, M. Lucchesi, P. Rolla, D. Prevosto, Interfacial and annealing effects on primary  $\alpha$ -relaxation of ultrathin polymer films investigated at nanoscale, *Macromolecules*. 45 (2012) 2138–2144. doi:10.1021/ma202757q.
- [151] H.K. Nguyen, M. Labardi, M. Lucchesi, P. Rolla, D. Prevosto, Plasticization in ultrathin polymer films: The role of supporting substrate and annealing, *Macromolecules*. 46 (2013) 555–561. doi:10.1021/ma301980w.
- [152] J.H. van Zanten, W.E. Wallace, W. Wu, Effect of strongly favorable substrate interactions on the thermal properties of ultrathin polymer films, *Phys. Rev. E*. 53 (1996) R2053.
- [153] A. Serghei, Challenges in glassy dynamics of polymers, *Macromol. Chem. Phys.* 209 (2008) 1415–1423. doi:10.1002/macp.200800197.
- [154] G.C. Pimental, A.L. McClelland, *The Hydrogen Bond*, Freeman, San Francisco, 1960.
- [155] F. Varnik, J. Baschnagel, K. Binder, Static and dynamic properties of supercooled thin polymer films, *Eur. Phys. J. E - Soft Matter*. 8 (2002) 175–192. doi:10.1140/epje/i2001-10092-8.
- [156] F. Varnik, J. Baschnagel, K. Binder, Reduction of the glass transition temperature in polymer films: A molecular-dynamics study, *Phys. Rev. E*. 65 (2002). doi:10.1103/PhysRevE.65.021507.
- [157] S. Peter, S. Napolitano, H. Meyer, M. Wübbenhorst, J. Baschnagel, Modeling dielectric relaxation in polymer glass simulations: Dynamics in the bulk and in supported polymer films, *Macromolecules*. 41 (2008) 7729–7743. doi:10.1021/ma800694v.
- [158] B. Frank, A.P. Gast, T.P. Russell, H.R. Brown, C. Hawker, Polymer mobility in thin films, *Macromolecules*. 29 (1996) 6531–6534.
- [159] D.B. Hall, J.C. Hooker, J.M. Torkelson, Ultrathin polymer films near the glass transition: effect on the distribution of  $\alpha$ -relaxation times as measured by second harmonic generation, *Macromolecules*. 30 (1997) 667–669.
- [160] D.B. Hall, J.M. Torkelson, Small molecule probe diffusion in thin and ultrathin supported polymer films, *Macromolecules*. 31 (1998) 8817–8825. doi:10.1021/ma9812128.
- [161] E.K. Lin, R. Kolb, S.K. Satija, W. Wu, Reduced polymer mobility near the polymer/solid interface as measured by neutron reflectivity, *Macromolecules*. 32 (1999) 3753–3757. doi:10.1021/ma9814604.
- [162] J. García-Turiel, B. Jérôme, Solvent retention in thin polymer films studied by gas chromatography, *Colloid Polym. Sci.* 285 (2007) 1617–1623. doi:10.1007/s00396-007-1733-6.
- [163] C.W. Frank, V. Rao, M.M. Despotopoulou, R.F.W. Pease, W.D. Hinsberg, R.D. Miller, et al., Structure in thin and ultra-thin spin-cast polymer films, *Science*. 247 (1996) 912–915. doi:DOI:10.1126/science.273.5277.912.
- [164] J. Perlich, E. Metwalli, L. Schulz, R. Georgii, P. Müller-Buschbaum, Solvent content in thin spin-coated polystyrene homopolymer films, *Macromolecules*. 42 (2008) 337–344.

- [165] Y. Grohens, L. Hamon, J. Spěvák, Y. Holl, The gel-like structure of polymer in thin films: an explanation of the thickness dependent glass transition?, *Macromol. Symp.* 203 (2003) 155–164. doi:10.1002/masy.200351314.
- [166] K. Dalnoki-Veress, J.A. Forrest, P.G. De Gennes, J.R. Dutcher, Glass transition reductions in thin freely-standing polymer films: A scaling analysis of chain confinement effects, *J. Phys. IV.* 10 (2000) 221–226.
- [167] P.G. De Gennes, Glass transitions in thin polymer films, *Eur. Phys. J. E.* 2 (2000) 201–205.
- [168] D. Long, F. Lequeux, Heterogeneous dynamics at the glass transition in van der Waals liquids, in the bulk and in thin films, *Eur. Phys. J. E.* 4 (2001) 371–387.
- [169] D. Long, P. Sotta, How the shift of the glass transition temperature of thin polymer films depends on the adsorption with the substrate, *ArXiv Prepr. Cond-Mat0301100.* (2003) 1–33.
- [170] S. Herminghaus, K. Jacobs, R. Seemann, The glass transition of thin polymer films: some questions, and a possible answer, *Eur. Phys. J. E.* 5 (2001) 531–538.
- [171] S. Herminghaus, Polymer thin films and surfaces: Possible effects of capillary waves, *Eur. Phys. J. E - Soft Matter.* 8 (2002) 237–243. doi:10.1140/epje/i2001-10056-0.
- [172] S. Herminghaus, R. Seemann, K. Landfester, Polymer surface melting mediated by capillary waves, *Phys. Rev. Lett.* 93 (2004) 017801. doi:10.1103/PhysRevLett.93.017801.
- [173] M. Wübbenhorst, C.A. Murray, J.R. Dutcher, Dielectric relaxations in ultrathin isotactic PMMA films and PS-PMMA-PS trilayer films, *Eur. Phys. J. E - Soft Matter.* 12 (2003) 109–112. doi:10.1140/epjed/e2003-01-025-1.
- [174] A. Serghei, F. Kremer, Confinement-induced relaxation process in thin films of cis-polyisoprene, *Phys. Rev. Lett.* 91 (2003) 165702. doi:10.1103/PhysRevLett.91.165702.
- [175] D. Labahn, R. Mix, A. Schönhals, Dielectric relaxation of ultrathin films of supported polysulfone, *Phys. Rev. E.* 79 (2009) 011801. doi:10.1103/PhysRevE.79.011801.
- [176] A. Piegari, E. Masetti, Thin film thickness measurement: a comparison of various techniques, *Thin Solid Films.* 124 (1985) 249–257.
- [177] P.D. Huibers, D.O. Shah, Multispectral determination of soap film thickness, *Langmuir.* 13 (1997) 5995–5998.
- [178] W.E. Wallace, N.C. Beck Tan, W.L. Wu, S. Satija, Mass density of polystyrene thin films measured by twin neutron reflectivity, *J. Chem. Phys.* 108 (1998) 3798. doi:10.1063/1.475769.
- [179] C. Bauer, R. Böhmer, S. Moreno-Flores, R. Richert, H. Sillescu, D. Neher, Capacitive scanning dilatometry and frequency-dependent thermal expansion of polymer films, *Phys. Rev. E.* 61 (2000) 1755.
- [180] P. Klapetek, D. Necas, Data analysis software, Central European Institute of Technology, Kotalářská, 2013. [www.gwyddion.net](http://www.gwyddion.net).
- [181] A. Serghei, F. Kremer, Broadband dielectric studies on the interfacial dynamics enabled by use of nanostructured electrodes, *Rev. Sci. Instrum.* 79 (2008) 026101. doi:10.1063/1.2839021.

- [182] K. Schwirn, W. Lee, R. Hillebrand, M. Steinhart, K. Nielsch, U. Gösele, Self-ordered anodic aluminum oxide formed by  $\text{H}_2\text{SO}_4$  hard anodization, *ACS Nano*. 2 (2008) 302–310. doi:10.1021/nm7001322.
- [183] L. Zaraska, G.D. Sulka, M. Jaskuła, Anodic alumina membranes with defined pore diameters and thicknesses obtained by adjusting the anodizing duration and pore opening/widening time, *J. Solid State Electrochem.* 15 (2011) 2427–2436. doi:10.1007/s10008-011-1471-z.
- [184] G.E.J. Poinern, N. Ali, D. Fawcett, Progress in nano-engineered anodic aluminum oxide membrane development, *Materials*. 4 (2011) 487–526. doi:10.3390/ma4030487.
- [185] R. Clausius, *Die mechanische wärmetheorie*, University of Michigan Library, 1876.
- [186] L. Onsager, Electric moments of molecules in liquids, *J. Am. Chem. Soc.* 58 (1936) 1486–1493. doi:10.1021/ja01299a050.
- [187] J.G. Kirkwood, The influence of hindered molecular rotation on the dielectric polarisation of polar liquids, *Trans. Faraday Soc.* 42 (1946) A007–A012.
- [188] H. Fröhlich, A. Theoretical dipolar interaction, *Trans. Faraday Soc.* 42 (1946) A003–A007.
- [189] R.D.L. Kronig, On the theory of dispersion of x-rays, *J. Opt. Soc. Am.* 12 (1926) 547–556. doi:10.1364/JOSA.12.000547.
- [190] H.B. Callen, T.A. Welton, Irreversibility and generalized noise, *Phys. Rev.* 83 (1951) 34–40.
- [191] P. Debye, *Polar molecules*, Dover Publications, New York, 1929.
- [192] P.J. Flory, *Statistical Mechanics of Chain Molecules*, Interscience, New York, 1969.
- [193] K.S. Cole, R.H. Cole, Dispersion and absorption in dielectrics I. Alternating current characteristics, *J. Chem. Phys.* 9 (1941) 341. doi:10.1063/1.1750906.
- [194] D.W. Davidson, R.H. Cole, Dielectric relaxation in glycerine, *J. Chem. Phys.* 18 (1950) 1471. doi:10.1063/1.1747496.
- [195] S. Havriliak, S. Negami, A complex plane representation of dielectric and mechanical relaxation processes in some polymers, *Polymer*. 8 (1967) 161–210.
- [196] A.K. Jonscher, *Universal Relaxation Law*, Chelsea Dielectric Press, London, 1996.
- [197] A. Schönhals, Fast calculation of the time dependent dielectric permittivity for the Havriliak-Negami function, *Acta Polym.* 42 (1991) 149–151. doi:10.1002/actp.1991.010420404.
- [198] A. Bello, E. Laredo, M. Grimau, Distribution of relaxation times from dielectric spectroscopy using Monte Carlo simulated annealing: application to  $\alpha$ -PVDF, *Phys. Rev. B*. 60 (1999) 12764–12774.
- [199] H. Fujiwara, *Spectroscopic Ellipsometry: Principles and Applications*, John Wiley & Sons, Ltd, West Sussex, 2007.
- [200] J.N. Hilfiker, In situ spectroscopic ellipsometry for characterization of thin film growth, in: G. Koster, G. Rijnders (Eds.), *Situ Charact. Thin Film Growth*, Woodhead Publishing Limited, Cambridge, 2011: p. 62.
- [201] M.Y. Efremov, E.A. Olson, M. Zhang, F. Schiettekatte, Z. Zhang, L.H. Allen, Ultrasensitive, fast, thin-film differential scanning calorimeter, *Rev. Sci. Instrum.* 75 (2004) 179–191. doi:10.1063/1.1633000.

- [202] F. Kremer, M. Tress, E.U. Mapesa, Broadband dielectric spectroscopy using nanostructured electrode arrangements, *Dielectrics Newsletter*. 10 (2012) 1–3.
- [203] A. Serghei, M. Tress, F. Kremer, The glass transition of thin polymer films in relation to the interfacial dynamics, *J. Chem. Phys.* 131 (2009) 154904. doi:10.1063/1.3248368.
- [204] S. Napolitano, D. Prevosto, M. Lucchesi, P. Pingue, M. D’Acunto, P. Rolla, Influence of a reduced mobility layer on the structural relaxation dynamics of aluminum capped ultrathin films of poly(ethylene terephthalate), *Langmuir*. 23 (2007) 2103–2109. doi:10.1021/la062229j.
- [205] R. Vila, M. Gonzalez, J. Molla, A. Ibarra, Dielectric spectroscopy of alumina ceramics over a wide frequency range, *J. Nucl. Mater.* 253 (1998) 141–148.
- [206] K. Konstadinidis, B. Thakkar, A. Chakraborty, L.W. Potts, R. Tannenbaum, M. Tirrell, et al., Segment level chemistry and chain conformation in the reactive adsorption of poly (methyl methacrylate) on aluminum oxide surfaces, *Langmuir*. 8 (1992) 1307–1317.
- [207] M. Morita, T. Ohmi, E. Hasegawa, M. Kawakami, M. Ohwada, Growth of native oxide on a silicon surface, *J. Appl. Phys.* 68 (1990) 1272. doi:10.1063/1.347181.
- [208] M. Krutyeva, A. Wischnewski, M. Monkenbusch, L. Willner, J. Maiz, C. Mijangos, et al., Effect of nanoconfinement on polymer dynamics: surface layers and interphases, *Phys. Rev. Lett.* 110 (2013) 108303. doi:10.1103/PhysRevLett.110.108303.
- [209] K. Terao, J.W. Mays, On-line measurement of molecular weight and radius of gyration of polystyrene in a good solvent and in a theta solvent measured with a two-angle light scattering detector, *Eur. Polym. J.* 40 (2004) 1623–1627. doi:10.1016/j.eurpolymj.2004.03.010.
- [210] M. Erber, A. Khalyavina, K.-J. Eichhorn, B.I. Voit, Variations in the glass transition temperature of polyester with special architectures confined in thin films, *Polymer*. 51 (2010) 129–135. doi:10.1016/j.polymer.2009.11.032.
- [211] Y. Liu, T.P. Russell, M.G. Samant, J. Stöhr, H.R. Brown, A. Cossy-Favre, et al., Surface relaxations in polymers, *Macromolecules*. 30 (1997) 7768–7771. doi:10.1021/ma970869a.
- [212] C.G. Robertson, T.E. Hogan, M. Rackaitis, J.E. Puskas, X. Wang, Effect of nanoscale confinement on glass transition of polystyrene domains from self-assembly of block copolymers, *J. Chem. Phys.* 132 (2010) 104904. doi:10.1063/1.3337910.
- [213] R. Weber, K.-M. Zimmermann, M. Tolan, J. Stettner, W. Press, O. Seeck, et al., X-ray reflectivity study on the surface and bulk glass transition of polystyrene, *Phys. Rev. E*. 64 (2001) 061508. doi:10.1103/PhysRevE.64.061508.
- [214] R. Zorn, M. Monkenbusch, D. Richter, A. Alegría, J. Colmenero, B. Farago, Plasticizer effect on the dynamics of polyvinylchloride studied by dielectric spectroscopy and quasielastic neutron scattering, *J. Chem. Phys.* 125 (2006) 154904. doi:10.1063/1.2357738.
- [215] S. Chandrasekhar, *Liquid Crystals*, 2nd ed., Cambridge University Press, Cambridge, 1992. <http://dx.doi.org/10.1017/CBO9780511622496>.
- [216] D. Demus, J. Goodby, G.W. Gray, H.W. Spiess, V. Vill, eds., *Handbook of liquid crystals*, Wiley-VCH, Weinheim, 1998.
- [217] P. Luigi Nordio, G. Rigatti, U. Segre, Dielectric relaxation theory in nematic liquids, *Mol. Phys.* 25 (1973) 129–136. doi:10.1080/00268977300100141.

- [218] G.S. Attard, K. Araki, G. Williams, A simple approach to the dielectric relaxation behaviour of a liquid crystalline polymer and its application to the determination of the director order parameter for partially aligned materials, *Br. Polym. J.* 19 (1987) 119–127.
- [219] K. Araki, G.S. Attard, A. Kozak, G. Williams, G.W. Gray, D. Lacey, et al., Molecular dynamics of a siloxane liquid-crystalline polymer as studied by dielectric relaxation spectroscopy, *J. Chem. Soc. Faraday Trans. 2 Mol. Chem. Phys.* 84 (1988) 1067–1081.
- [220] W.H. de Jeu, *Physical properties of liquid crystalline material*, Gordon & Breach, New York, London, Paris, 1979.
- [221] C. Baehr, B. Glösen, J.H. Wendorff, E.G. Staring, Dielectric relaxation studies on the side group rotation of NLO-active side-group polymers, *Macromol. Rapid Commun.* 15 (1994) 327–333. doi:DOI: 10.1002/marc.1994.030150405.
- [222] A. Brás, M. Dionísio, H. Huth, C. Schick, A. Schönhals, Origin of glassy dynamics in a liquid crystal studied by broadband dielectric and specific heat spectroscopy, *Phys. Rev. E.* 75 (2007) 061708. doi:10.1103/PhysRevE.75.061708.
- [223] A.R. Brás, S. Frunza, L. Guerreiro, I.M. Fonseca, A. Corma, L. Frunza, et al., Molecular mobility of nematic E7 confined to molecular sieves with a low filling degree, *J. Chem. Phys.* 132 (2010) 224508. doi:10.1063/1.3432775.
- [224] C. Grigoriadis, H. Duran, M. Steinhart, M. Kappl, H.-J. Butt, G. Floudas, Suppression of Phase Transitions in a Confined Rodlike Liquid Crystal, *ACS Nano.* 5 (2011) 9208–9215. doi:10.1021/nn203448c.
- [225] C. Schick, D. Sukhorukov, A. Schönhals, Comparison of the molecular dynamics of a liquid crystalline side group polymer revealed from temperature modulated DSC and dielectric experiments in the glass transition region, *Macromol. Chem. Phys.* 202 (2001) 1398–1404.
- [226] M. Tarnacka, K. Adrjanowicz, E. Kaminska, K. Kaminski, K. Grzybowska, K. Kłodziejczyk, et al., Molecular dynamics of itraconazole at ambient and high pressure, *Phys. Chem. Chem. Phys.* 15 (2013) 20742. doi:10.1039/c3cp52643g.
- [227] J. Van Cutsem, F. Van Gerven, M.A. Van de Ven, M. Borgers, P.A. Janssen, Itraconazole, a new triazole that is orally active in aspergillosis., *Antimicrob. Agents Chemother.* 26 (1984) 527–534.
- [228] K. Six, G. Verreck, J. Peeters, K. Binnemans, H. Berghmans, P. Augustijns, et al., Investigation of thermal properties of glassy itraconazole: identification of a monotropic mesophase, *Thermochim. Acta.* 376 (2001) 175–181.
- [229] K. Six, G. Verreck, J. Peeters, P. Augustijns, R. Kinget, G. Van den Mooter, Not known to me, *Int J Pharm.* 213 (2001) 163–173.
- [230] H. Lin, P. Palffy-Muhoray, M.A. Lee, Liquid crystalline cores for optical fibers, *Mol. Cryst. Liq. Cryst.* 204 (1991) 189–200. doi:10.1080/00268949108046605.
- [231] T. Bellini, N.A. Clark, C.D. Muzny, L. Wu, C.W. Garland, D.W. Schaefer, et al., Phase behavior of the liquid crystal 8CB in a silica aerogel, *Phys. Rev. Lett.* 69 (1992) 788.
- [232] G.S. Iannacchione, D. Finotello, Calorimetric study of phase transitions in confined liquid crystals, *Phys. Rev. Lett.* 69 (1992) 2094.



- [233] G. Iannacchione, D. Finotello, Confinement and orientational study at liquid crystal phase transitions, *Liq. Cryst.* 14 (1993) 1135–1142. doi:10.1080/02678299308027821.
- [234] A.R. Brás, M. Dionísio, A. Schönals, Confinement and surface effects on the molecular dynamics of a nematic mixture investigated by dielectric relaxation spectroscopy, *J. Phys. Chem. B.* 112 (2008) 8227–8235. doi:10.1021/jp802133e.
- [235] E.U. Mapesa, M. Tarnacka, E. Kaminska, K. Adrjanowicz, M. Dulski, W. Kossack, et al., Molecular dynamics of itraconazole confined in thin supported layers, *RSC Adv.* 4 (2014) 28432–28438. doi:10.1039/c4ra01544d.
- [236] M. Davies, R. Moutran, A.H. Price, M.S. Beevers, G. Williams, Dielectric and optical studies of a nematogen (4, 4-*n*-heptyl-cyanobiphenyl), *J Chem Soc Faraday Trans 2.* 72 (1976) 1447–1458.
- [237] A.C. Legon, D.J. Millen, Angular geometries and other properties of hydrogen-bonded dimers: a simple electrostatic interpretation of the success of the electron-pair model, *Chem. Soc. Rev.* 16 (1987) 467–498.
- [238] J.T. Mang, K. Sakamoto, S. Kumar, Smectic layer orientation in confined geometries, *Mol. Cryst. Liq. Cryst.* 223 (1992) 133–142. doi:10.1080/15421409208048246.
- [239] I. Bahar, B. Erman, F. Kremer, E.W. Fischer, Segmental motions of cis-polyisoprene in the bulk state: interpretation of dielectric relaxation data, *Macromolecules.* 25 (1992) 816–825.
- [240] A. Schönals, H. Goering, C. Schick, B. Frick, R. Zorn, Glass transition of polymers confined to nanoporous glasses, *Colloid Polym. Sci.* 282 (2004) 882–891. doi:10.1007/s00396-004-1106-3.
- [241] L. Berthier, Direct experimental evidence of a growing length scale accompanying the glass transition, *Science.* 310 (2005) 1797–1800. doi:10.1126/science.1120714.
- [242] E.-J. Donth, The size of cooperatively rearranging regions at the glass transition, *J. Non-Cryst. Solids.* 53 (1982) 325–330.
- [243] C.M. Roland, Characteristic relaxation times and their invariance to thermodynamic conditions, *Soft Matter.* 4 (2008) 2316. doi:10.1039/b804794d.
- [244] A. Brûlet, F. Boué, A. Menelle, J.P. Cotton, Conformation of polystyrene chain in ultrathin films obtained by spin coating, *Macromolecules.* 33 (2000) 997–1001. doi:10.1021/ma9906783.
- [245] H. Tsuruta, Y. Fujii, N. Kai, H. Kataoka, T. Ishizone, M. Doi, et al., Local conformation and relaxation of polystyrene at substrate interface, *Macromolecules.* 45 (2012) 4643–4649. doi:10.1021/ma3007202.
- [246] A. Serghei, F. Kremer, W. Kob, Chain conformation in thin polymer layers as revealed by simulations of ideal random walks, *Eur. Phys. J. E - Soft Matter.* 12 (2003) 143–146. doi:10.1140/epje/i2003-10038-2.
- [247] M. Solar, E.U. Mapesa, F. Kremer, K. Binder, W. Paul, The dielectric  $\alpha$ -relaxation in polymer films: A comparison between experiments and atomistic simulations, *Europhys. Lett.* 104 (2013) 66004. doi:10.1209/0295-5075/104/66004.
- [248] L.V. Azároff, X-ray scattering by cybotactic nematic mesophases, *Proc. Natl. Acad. Sci.* 77 (1980) 1252–1254.
- [249] I.G. Chistyakov, W.M. Chaikowsky, The structure of *p*-azoxybenzenes in magnetic fields, *Mol. Cryst.* 7 (1969) 269–277. doi:10.1080/15421406908084877.

- [250] A.D. Vries, Evidence for the existence of more than one type of nematic phase, *Mol. Cryst. Liq. Cryst.* 10 (1970) 31–35. doi:10.1080/15421407008083484.
- [251] O. Francescangeli, E.T. Samulski, Insights into the cybotactic nematic phase of bent-core molecules, *Soft Matter*. 6 (2010) 2413. doi:10.1039/c003310c.
- [252] C. Keith, A. Lehmann, U. Baumeister, M. Prehm, C. Tschierske, Nematic phases of bent-core mesogens, *Soft Matter*. 6 (2010) 1704. doi:10.1039/b923262a.
- [253] A.D. Vries, X-ray photographic studies of liquid crystals I. A cybotactic nematic phase, *Mol. Cryst. Liq. Cryst.* 10 (1970) 219–236. doi:10.1080/15421407008083495.
- [254] L. Petychakis, G. Floudas, G. Fleischer, Chain dynamics of polyisoprene confined in porous media. A dielectric spectroscopy study, *Europhys. Lett.* 40 (1997) 685–690.
- [255] K. Adachi, T. Kotaka, Dielectric normal mode process in undiluted cis-polyisoprene, *Macromolecules*. 18 (1985) 466–472.
- [256] K. Kojio, S. Jeon, S. Granick, Confinement-induced differences between dielectric normal modes and segmental modes of an ion-conducting polymer, *Eur. Phys. J. E - Soft Matter*. 8 (2002) 167–173. doi:10.1140/epje/i2001-10090-x.
- [257] S. Jeon, S. Granick, A polymer's dielectric normal modes depend on its film thickness when confined between nonwetting surfaces, *Macromolecules*. 34 (2001) 8490–8495. doi:10.1021/ma010015x.
- [258] A.P. Holt, J.R. Sangoro, Y. Wang, A.L. Agapov, A.P. Sokolov, Chain and segmental dynamics of poly(2-vinylpyridine) nanocomposites, *Macromolecules*. 46 (2013) 4168–4173. doi:10.1021/ma400418b.
- [259] W.H. Stockmayer, Dielectric dispersion in solutions of flexible polymers, *Pure Appl. Chem.* 15 (1967) 539–554.
- [260] N. Hadjichristidis, J.E.L. Roovers, Synthesis and solution properties of linear, four-branched, and six-branched star polyisoprenes, *J. Polym. Sci. Polym. Phys. Ed.* 12 (1974) 2521–2533.
- [261] G. Floudas, T. Reisinger, Pressure dependence of the local and global dynamics of polyisoprene, *J. Chem. Phys.* 111 (1999) 5201.
- [262] M.L. Williams, R.F. Landel, J.D. Ferry, The temperature dependence of relaxation mechanisms in amorphous polymers and other glass-forming liquids, *J. Am. Chem. Soc.* 77 (1955) 3701–3707.
- [263] E.U. Mapesa, L. Popp, W.K. Kipnusu, M. Tress, F. Kremer, Molecular dynamics in 1- and 2-D confinement as studied for the case of poly(cis-1,4-isoprene), *Soft Mater. Accepted* (2014). doi:10.1080/1539445X.2014.928320.
- [264] V.M. Boucher, D. Cangialosi, A. Alegría, J. Colmenero, Accounting for the thickness dependence of the T<sub>g</sub> in supported PS films via the volume holes diffusion model, *Thermochim. Acta.* 575 (2014) 233–237. doi:10.1016/j.tca.2013.10.023.
- [265] P.J. Flory, *Principles of Polymer Chemistry*, Cornell University Press, New York, 1953.
- [266] E.U. Mapesa, M. Tress, M. Reiche, F. Kremer, Molecular dynamics of poly(cis-1,4-isoprene) in 1- and 2-dimensional confinement, in: F. Kremer (Ed.), *Dyn. Geom. Confin.*, Springer-Verlag, Berlin Heidelberg New York, 2014: pp. 95–126. [http://link.springer.com/chapter/10.1007%2F978-3-319-06100-9\\_4](http://link.springer.com/chapter/10.1007%2F978-3-319-06100-9_4).

- [267] J.A. Forrest, K. Dalnoki-Veress, The glass transition in thin polymer films, *Adv. Colloid Interface Sci.* 94 (2001) 167–195.
- [268] F. Kremer, E.U. Mapesa, M. Tress, M. Reiche, Molecular dynamics of polymers at nanometric length scales: from thin layers to isolated coils, in: Y.P. Kalmykov (Ed.), *Recent Adv. Broadband Dielectr. Spectrosc.*, Springer, Dordrecht, 2011: pp. 163–178.
- [269] M.D. Ediger, J.A. Forrest, Dynamics near free surfaces and the glass transition in thin polymer films: a view to the future, *Macromolecules.* 47 (2013) 471–478. doi:10.1021/ma4017696.
- [270] J.A. Forrest, K. Dalnoki-Veress, When does a glass transition temperature not signify a glass transition?, *ACS Macro Lett.* 3 (2014) 310–314. doi:10.1021/mz4006217.
- [271] J.A. Forrest, What can we learn about a dynamical length scale in glasses from measurements of surface mobility?, *J. Chem. Phys.* 139 (2013) 084702. doi:10.1063/1.4818989.
- [272] J.E. Pye, C.B. Roth, Two simultaneous mechanisms causing glass transition temperature reductions in high molecular weight freestanding polymer films as measured by transmission ellipsometry, *Phys. Rev. Lett.* 107 (2011) 235701. doi:10.1103/PhysRevLett.107.235701.

# Appendices

## A1 List of Publications

### A1.1 Peer-Reviewed Papers

15) Kremer, F., Tress, M. and Mapesa, E.U. **Glassy dynamics and glass transition in nanometric layers and films: a silver lining on the horizon**, Journal of Non-Crystalline Solids, *accepted* August 2014 ([doi:10.1016/j.jnoncrysol.2014.08.016](https://doi.org/10.1016/j.jnoncrysol.2014.08.016))

14) Kaminska, E., Adrjanowicz, K., Tarnacka, M., Kolodziejczyk, K., Dulski, M., Mapesa, E.U., Zakowiecki, D., Hawelek, L., Smolka, W., I. Kaczmarczyk-Sedlak, I. and Kaminski, K. **Impact of inter and intramolecular interactions on the physical stability of indomethacin dispersed in acetylated saccharides**, Molecular Pharmaceutics 11(8), 2935, 2014. ([doi:10.1021/mp500286b](https://doi.org/10.1021/mp500286b))

13) Mapesa, E.U., Tarnacka, M., Adrjanowicz, K., Dulski, M., Tress, M., Kossack, W.K., Kipnusu, W.K., Kaminiski, K. and Kremer, F. **Molecular dynamics of itraconazole confined in thin supported layers**, RSC Advances 4 (54), 28432, 2014. ([doi: 10.1039/C4RA01544D](https://doi.org/10.1039/C4RA01544D))

12) Mapesa, E.U., Ludwig, P., Kipnusu, W.K., Tress, M. and Kremer, F. **Molecular dynamics in 1- and 2-D confinement as studied for the case of poly(*cis*-1,4-isoprene)** Soft Materials, *accepted* May 9<sup>th</sup>, 2014. ([doi: 10.1080/1539445X.2014.928320](https://doi.org/10.1080/1539445X.2014.928320))

11) Kossack, W., Kipnusu, W.K., Dulski, M., Adrjanowicz, K., Madejczyk, O., Kaminska, E., Mapesa, E.U., Tress, M., Kaminiski, K. and Kremer, F. **The kinetics of mutarotation in L-fucose as monitored by dielectric and infrared spectroscopy**, Journal of Chemical Physics 140 (21), 215101, 2014. ([doi: 10.1063/1.4880718](https://doi.org/10.1063/1.4880718))

10) Solar, M., Mapesa, E.U., Binder, K., Kremer, F. and Paul, W. **The dielectric  $\alpha$ -relaxation in polymer films: A comparison between experiments and atomistic simulations** Europhysics Letters 104 (6), 66004, 2013. ([doi: 10.1209/0295-5075/104/66004](https://doi.org/10.1209/0295-5075/104/66004))

9) Kossack, W., Adrjanowicz, K., Tarnacka, M., Kipnusu, W.K., Dulski, M., Mapesa, E.U., Kaminiski, K., Pawlus, S., Paluch, M. and Kremer, F. **Glassy dynamics and physical aging in fucose saccharides as studied by infrared- and broadband dielectric spectroscopy** Physical Chemistry Chemical Physics 15 (47), 20641, 2013. ([doi: 10.1039/c3cp52551a](https://doi.org/10.1039/c3cp52551a))

8) Kipnusu, W.K., Elmahdy, M.M., Tress, M., Fuchs, M., Mapesa, E.U., Smilgies, D.-M., Zhang, J., Papadakis, C.M., and Kremer, F. **Molecular order and dynamics of nanometric thin layers of poly(styrene-*b*-isoprene-1.4) diblock copolymers** Macromolecules 46 (24), 9729, 2013. ([doi: 10.1021/ma4019334](https://doi.org/10.1021/ma4019334))

- 7) Mapesa, E.U., Tress, M., Schulz, G., Huth, H., Schick, C., Reiche, M., Kremer, F., **Segmental and chain dynamics in nanometric layers of poly(cis-1,4-isoprene) as studied by broadband dielectric spectroscopy and temperature-modulated calorimetry** *Soft Matter* 9 (44), 10592, 2013. ([doi: 10.1039/c3sm51311d](https://doi.org/10.1039/c3sm51311d))
  
- 6) Tress, M., Mapesa, E.U., Kossack, W., Kipnusu, W.K., Reiche, M. and Kremer, F. **Glassy dynamics in condensed isolated polymer coils** *Science* 341 (6152), 1371, 2013. ([doi: 10.1126/science.1238950](https://doi.org/10.1126/science.1238950))
  
- 5) Kaminski, K., Kipnusu, W.K., Adrjanowicz, K., Mapesa, E.U., Jasiurkowska, M., Włodarczyk, P., Grzybowska, K., Paluch, M. and Kremer, F. **Comparative study on the molecular dynamics of a series of polypropylene glycols** *Macromolecules* 46, 1973, 2013. ([doi: 10.1021/ma302611x](https://doi.org/10.1021/ma302611x))
  
- 4) Mapesa, E.U., Erber, M., Tress, M., Eichhorn, K.-J., Serghei, A., Voit, B. and Kremer, F. **Glassy dynamics in nanometer thin layers of polystyrene** *European Physical Journal - Special Topics* 189, 173, 2010. ([doi: 0.1140/epjst/e2010-01320-2](https://doi.org/0.1140/epjst/e2010-01320-2))
  
- 3) Erber, M., Tress, M., Mapesa, E.U., Serghei, A., Eichhorn, K.-J., Voit, B. and Kremer, F. **Glassy dynamics and glass transition in thin polymer layers of PMMA deposited on different substrates** *Macromolecules* 43, 7729, 2010. ([doi: 10.1021/ma100912r](https://doi.org/10.1021/ma100912r))
  
- 2) Tress, M, Erber, M., Mapesa, E.U., Huth, H., Müller, J., Serghei, A., Schick, C., Eichhorn, K.-J., Voit, B. and Kremer, F. **Glassy Dynamics and Glass Transition in Nanometric Thin Layers of Polystyrene** *Macromolecules* 43, 9937, 2010. ([doi: 10.1021/ma102031k](https://doi.org/10.1021/ma102031k))
  
- 1) Mapesa, E.U., Odote, J.M. & Okumu, J. 2006. **Optical properties of indium-tin-oxide thin films prepared by non-reactive dc magnetron sputtering** *East African Journal of Pure and Applied Sciences* 7, 13, 2006.

## A1.2 Book Chapters

- 3) Mapesa, E.U., Tress, M., Reiche, M. and Kremer, F. **Molecular dynamics of poly(cis-1,4-isoprene) in 1- and 2-dimensional confinement** in *Dynamics in Geometrical Confinement (Volume 2)*, edited by Friedrich Kremer, Springer 2014. ([doi: 10.1007/978-3-319-06100-9\\_4](https://doi.org/10.1007/978-3-319-06100-9_4))
  
- 2) Tress, M. Mapesa, E.U., Reiche, M. and Kremer, F. **Molecular dynamics of condensed (semi-) isolated polymer chains** in *Dynamics in Geometrical Confinement (Volume 2)*, edited by Friedrich Kremer, Springer 2014. ([doi: 10.1007/978-3-319-06100-9\\_3](https://doi.org/10.1007/978-3-319-06100-9_3))
  
- 1) Kremer, F., Mapesa, E.U. and Tress, M. **Molecular dynamics of polymers at nanometric length scales: From thin layers to isolated coils** in *Recent Advances in Broad-*

band Dielectric Spectroscopy, edited by Yuri P. Kalmykov, Springer 2012 ([doi: 10.1007/978-94-007-5012-8](https://doi.org/10.1007/978-94-007-5012-8))

### A1.3 Conference Proceedings and others

4) Kremer, F., Serghei, A., Sangoro, J.R., Tress, M. and Mapesa, E.U. **Broadband dielectric spectroscopy in nano-(bio)-physics** IEEE Transactions on Dielectrics and Electrical Insulation 2009. ([doi: 10.1109/CEIDP.2009.5377717](https://doi.org/10.1109/CEIDP.2009.5377717))

3) Kremer, F., Treß, M. and Mapesa, E.U. **Broadband Dielectric Spectroscopy using nanostructured electrode arrangements** Dielectrics Newsletter 26, 1, 2012.

2) Mapesa, E.U. **Influence of deposition pressure on the optical properties of dc-magnetron sputtered Indium Tin Oxide (ITO) thin films** MSc Thesis, Kenyatta University, Nairobi, Kenya. 2006. <http://ir-library.ku.ac.ke/handle/123456789/1949>

1) Mapesa, E.U., Odote, J.M. & Okumu, J. **Optical properties of thin dc-sputtered indium tin oxide films prepared in non-reactive ambiance** The Ninth College on Thin Film Technology, 24<sup>th</sup> July– 4<sup>th</sup> August 2006, University of Dar es Salaam, Dar es Salaam, Tanzania.

## A2 Acknowledgements

I would like to express my sincere appreciation to the following for the support they gave me during my PhD work:

- Prof. Dr. Friedrich Kremer, for giving me an opportunity to work in his research group, and for his unfailing guidance throughout the time of this work;
- Prof. Dr. Mario Beiner (Martin-Luther-Universität Halle-Wittenberg), for accepting to be my mentor in the framework of the integrated Research Training Group (SFB TRR 102), and sharing with me his views about the subjects of my research;
- Dr. Joshua Sangoro, for recommending me to Prof. Kremer when an open PhD position arose in the latter's Research Group;
- Dipl.-Phys. Martin Treß, for introducing me to all the instrumentation that I eventually used for my experiments, and for the fruitful collaboration that saw us co-publish several papers;
- All my colleagues in the Department of Molecular Physics (MOP), for the friendly atmosphere they provided, and helpful discussions I had with many of them. I appreciate too the ever-present help of Dipl.-Ing. Reinmuth Jörg and Dipl.-Phys. Wiktor Skokov in keeping all experimental tools in the lab in usable form, and staying at the cutting edge of innovation.
- Friends like Margret and Heiner Hoffman, Linnet and Wycliffe Kipnusu, Jacinta and Markus Wagner, Funbi and Agboola Oni-Orisan, Pamela and Dan Omanga, Katherene Söllner, Aruna Haruna, Arun Prasad-Raja and Loti Mgondi for being there to ensure that life outside the laboratory experience was also interesting;
- My parents and parents-in-law (Nancy and Elijah Mapesa, and Josephine and John Mutisya) for their constant material and kind support for my family;
- My beautiful wife Gladys Mumbua for her patience, prayerfulness and resilience, and for taking good care of our little angels – Viktoria and Samara – during the many times when I was absent from them. Gladys also read through the first draft of this thesis to ensure its fidelity to the English language. I thank Viktoria and Samara too for inspiring me to work harder by their quick growth and development, and their lovely innocent demands;
- Last but most important, I thank my God for giving me life and strength to function, and for making my life in Leipzig fruitful and enjoyable.


### **A3 Selbständigkeitserklärung**

Ich erkläre hiermit, dass ich diese Dissertation selbständig und ohne unerlaubte Hilfe gemacht. Ich habe keine anderen als im Schriftenverzeichnis angeführten Quellen benutzt und sämtliche Textstellen, die wörtlich oder sinngemäß aus veröffentlichten oder unveröffentlichten Schriften entnommen wurde, und alle Angaben, die auf mündlichen Auskünften beruhen, als solche kenntlich gemacht. Ebenfalls sind alle von anderen Personen bereitgestellten Materialien oder erbrachten Dienstleistungen also solche gekennzeichnet. Weitere Personen waren bei der geistigen Erstellung der vorliegenden Arbeit nicht beteiligt und haben keine geldwerten Leistungen für Arbeiten im Zusammenhang mit der Dissertation erhalten. Die vorliegende Arbeit wurde weder im Inland noch im Ausland in gleicher oder in ähnlicher Form einer anderen Prüfungsbehörde zum Zwecke einer Promotion oder eines anderen Prüfungsverfahrens vorgelegt und in ihrer Gesamtheit nicht veröffentlicht. Ich versichere, dass keine erfolglosen Prüfungsversuche stattgefunden haben.

**Leipzig, den**

**Emmanuel Urandu Mapesa**

**17.11.2014**



Ich bin damit einverstanden, dass nach einer positiven Bewertung, diese Arbeit wird in der Universitätsbibliothek werden.

**Leipzig, den**

**Emmanuel Urandu Mapesa**

**17.11.2014**





*Bless the Lord, O my soul – and all that is within me –  
bless his Holy Name.*  
**Psalm 103:1**